

INFORMATION TO USERS

This manuscript has been reproduced from the microfilm master. UMI films the text directly from the original or copy submitted. Thus, some thesis and dissertation copies are in typewriter face, while others may be from any type of computer printer.

The quality of this reproduction is dependent upon the quality of the copy submitted. Broken or indistinct print, colored or poor quality illustrations and photographs, print bleedthrough, substandard margins, and improper alignment can adversely affect reproduction.

In the unlikely event that the author did not send UMI a complete manuscript and there are missing pages, these will be noted. Also, if unauthorized copyright material had to be removed, a note will indicate the deletion.

Oversize materials (e.g., maps, drawings, charts) are reproduced by sectioning the original, beginning at the upper left-hand corner and continuing from left to right in equal sections with small overlaps. Each original is also photographed in one exposure and is included in reduced form at the back of the book.

Photographs included in the original manuscript have been reproduced xerographically in this copy. Higher quality 6" x 9" black and white photographic prints are available for any photographs or illustrations appearing in this copy for an additional charge. Contact UMI directly to order.

U·M·I

University Microfilms International
A Bell & Howell Information Company
300 North Zeeb Road, Ann Arbor, MI 48106-1346 USA
313/761-4700 800/521-0600

Order Number 9410174

Studies of the geophysics of sea ice

Wade, Robert Hampton, Ph.D.

University of Alaska Fairbanks, 1993

U·M·I
300 N. Zeeb Rd.
Ann Arbor, MI 48106

STUDIES OF THE GEOPHYSICS OF SEA ICE

A

THESIS

Presented to the Faculty

of the University of Alaska Fairbanks

in Partial Fulfillment of the Requirements

for the Degree of

DOCTOR OF PHILOSOPHY

By

Robert H. Wade, B.A.

Fairbanks, Alaska

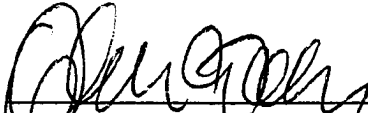
December 1993

STUDIES OF THE GEOPHYSICS OF SEA ICE

By

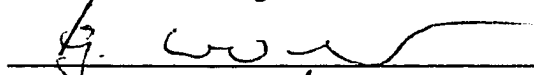
Robert H. Wade

RECOMMENDED:


Dr. Gunter E. Weller


Dr. H. Joseph Niebauer

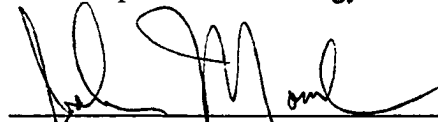

Dr. William J. Stringer


Dr. Gerd-D. Wendler


Dr. Wilford F. Weeks, Chairman,
Advisory Committee


Dr. R. Keith Crowder, Head,
Department of Geology and Geophysics

APPROVED:


Dr. John Morack, Interim Dean, College of Natural Sciences


Dr. Edward Murphy, Interim Dean of the Graduate School

27 October 1993
Date

Abstract

A non-linear growth model that solves the surface energy balance and heat conduction equations was developed to estimate thermal and physical properties of sea ice. The model incorporates several mechanisms that affect the salinity profile, including initial brine entrapment, brine expulsion, and gravity drainage, and is a non-linear extension of the model initially developed by Cox and Weeks (1988). Simulations were run to investigate the effects of the non-linear feedbacks which exist between the ice growth velocity and the thermal properties of the resulting ice. A comparison of the growth rate versus accumulated freeze-days was performed on the linear model, the non-linear model, and empirical formulas based on field observations. Allowing the model to run through the summer months with retarded ice growth and making an attempt at modelling summer desalinization processes produced second and third-year ice with proper temperature and salinity profiles.

The ice growth model was then coupled to a Lambertian surface backscattering model for radar. By calculating the average dielectric constant of the penetration depth and using this value in the backscattering model, a comparison of the predicted signature variations in first-year sea ice was performed against observed backscattering values from ERS-1 SAR images of Dease Inlet, Alaska. The agreement between calculated and observed backscatter was surprisingly good considering that other factors may also influence radar returns. However, the more surprising result was the rescaling of the predicted first year ice signature by + 6 dB produced a remarkable fit to observed backscattering values of multiyear ice. The predicted backscatter values and ice thicknesses were then used in conjunction with ERS-1 SAR imagery of the high Arctic to estimate areal coverage of the three major ice types in a $100 \times 100 \text{ km}^2$ area. Heat and mass flux calculations were then performed to produce daily estimates of energy loss and salt infusion for the winter months of October 1991 through March 1992.

Contents

Abstract	iii
List of Figures	ix
List of Tables	xiii
Acknowledgments	xv
1. General introduction	1
1.1 Dissertation Objectives	1
1.2 Sea Ice and the Earth's Climate Machine	2
1.3 Sea Ice and Remote Sensing	6
2. Sea Ice Growth Model	9
2.1 Introduction	9
2.2 Program Structure	9
2.2.1 Initialization	10
2.2.2 Finite-Difference Routine	11
2.2.3 Surface Energy Balance Routine	11
2.2.4 Ice Properties Routine	12
2.2.5 Desalination Process	12
2.3 Detailed Model Description	13
2.3.1 Surface Energy Balance	13
2.3.1.1 Introduction	13
2.3.1.2 Incoming Shortwave Radiation (F_r)	14
2.3.1.3 Net Influx of Radiation to the Interior of the Ice (I_0)	15

2.3.1.4 Incoming Longwave Radiation (F_I)	16
2.3.1.5 Emitted Longwave Radiation (F_E)	16
2.3.1.6 Sensible Heat Flux (F_S)	16
2.3.1.7 Latent Heat Flux (F_E)	17
2.3.1.8 Conductive Heat Flux (F_C)	18
2.3.1.9 Oceanic Heat Flux (F_O)	20
2.3.1.10 Snow	20
2.3.2 Ice Properties	21
2.3.2.1 Introduction	21
2.3.2.2 Initial Salt Entrapment	21
2.3.2.3 Brine Salinity	22
2.3.2.4 Brine Density	23
2.3.2.5 Latent Heat of Fusion	23
2.3.2.6 Heat Capacitance	23
2.3.3 Desalination Process	24
2.3.3.1 Introduction	24
2.3.3.2 Brine Expulsion	24
2.3.3.3 Gravity Drainage	25
2.3.4 Finite Difference Routine	26
2.3.4.1 General	26
2.3.4.2 Forward Elimination	29
2.3.4.3 Backward Elimination	30

2.4 Meteorological Data	33
2.5 Model Results	35
2.5.1 First Year Ice	35
2.5.2 Multiyear Ice	39
2.6 Model Comparisons	47
2.6.1 Introduction	47
2.6.2 Ice Thickness	49
2.6.3 Ice Properties	52
3. Synthetic Aperture Radar	55
3.1 Introduction	55
3.2 Surface Scattering	60
3.3 Volume Scattering	63
3.4 Sea Ice Backscattering Model	64
3.5 Incident Angle Dependence	67
3.6 SAR Model Results	67
3.6.1 First Year Backscatter Values	67
3.6.2 Multiyear Backscatter Values	77
4. Ice Thickness Estimates	80
4.1 Introduction	80
4.2 Supervised Ice Type Estimates	82
4.3 Unsupervised Ice Type Estimates	86

5. Flux Calculations	89
5.1 Introduction	89
5.2 New Ice / Open Water Fluxes	90
5.3 First Year Ice Fluxes	92
5.4 Multiyear Ice Fluxes	93
5.5 Comparison of Flux Results With Previous Studies	96
6. Summary and Recommendations	98
6.1 Sea Ice Growth	98
6.2 Backscattering Model	101
6.3 Areal Coverage of Ice Types and Thickness Estimates	102
6.4 Flux Calculations	104
Appendix A. Image Radiometric Corrections	106
Appendix B. Ice Classification Tables	108
Appendix C. Daily Heat Flux Tables	112
Appendix D. Daily Salt Flux Tables	122
Bibliography	131

List of Figures

Figure 1	Map Showing Study Areas.	2
Figure 2	Energy Flux Indices for Atmosphere–Ice–Ocean.	14
Figure 3	Finite-Difference Grid Indices.	28
Figure 4	Finite Difference Grid for Region Containing the Phase Boundary.	31
Figure 5	Comparison of Unidata air temperatures verses NOAA Station air temperatures.	34
Figure 6	Dease Inlet First Year Ice Profile 1; growth started on 10 October 1991.	36
Figure 7	Dease Inlet First Year Ice Profile 2; growth started on 18 November 1991.	37
Figure 8	High Arctic First Year Ice Profile; growth started on 1 November 1991.	38
Figure 9	High Arctic First Year Ice Profile; growth started on 3 November 1991.	39
Figure 10	Multiyear Ice on September 1 without Meltwater Desalinization.	40
Figure 11	Multiyear Ice on January 1 without Meltwater Desalinization.	41

Figure 12	Multiyear Ice on May 15 without Meltwater Desalinization.	42
Figure 13	Average MY Salinity Profiles for Hummocked (A), Depressed Ice (B) and Average MY Profile from Station Alpha(C). (Cox and Weeks 1975).	43
Figure 14	Multiyear Ice on September 1 with Meltwater Desalinization.	44
Figure 15	Multiyear Ice on January 1 with Meltwater Desalinization. . .	45
Figure 16	Multiyear Ice on May 15 with Meltwater Desalinization. . .	46
Figure 17	Growth Rate Comparison.	50
Figure 18	Look Angle Dependence.	68
Figure 19	Measurement Areas Near Point Barrow, Alaska, showing the two areas analyzed.	70
Figure 20	Dease Inlet Profile 1.	71
Figure 21	Predicted vs Measured Backscatter for Dease Inlet 1. . .	72
Figure 22	Backscatter vs days for ice with initial growth starting on various days – Ideal.	73
Figure 23	Backscatter vs days for ice with initial growth starting on various days – Reality.	74
Figure 24	Predicted vs Measured Backscatter for Dease Inlet 2. . .	75

Figure 25	Dease Inlet Profile 2.	76
Figure 26	Measured Backscatter for Multiyear Ice.	77
Figure 27	Multiyear Predicted and Measured Backscatter.	78
Figure 28	Area Coverage For multiyear (MY), first year (FY) and new ice/open water (NI/OW).	84
Figure 29	Area Total Heat Flux For MY-2m, MY-3m, FY and NI/OW. .	95
Figure 30	Arctic Air Temperatures vs Average Air Temperatures. .	100

List of Tables

Table 1	Table of Snow Accumulation Options.	20
Table 2	Model Constants.	66
Table 3	Lookup Table for JPL Classification Algorithm.	86
Table 4	Supervised vs Unsupervised Ice Coverage Comparison.	87
Table 5	New Ice/Open Water Heat and Salt Flux Summary.	91
Table 6	First Year Ice Heat and Salt Flux Summary.	92
Table 7	2m Multiyear Ice Heat and Salt Flux Summary.	94
Table 8	3m Multiyear Ice Heat and Salt Flux Summary.	94
Table 9	Monthly Heat Flux Densities After (Maykut, 1982).	96
Table 10	Monthly Heat Flux Densities for Current Study.	96
Table 11	Soviet NP-23 and NP-4 Heat Fluxes.	96
Table 12	Supervised Ice Classification Results.	108
Table 13	GPS Ice Classification Results.	110
Table 14	Daily Flux Densities for NI/OW and FY Ice.	112
Table 15	Daily Heat Fluxes for NI/OW and FY Ice.	114
Table 16	Daily Heat Fluxes for 2 Meter Multiyear Ice.	116
Table 17	Daily Heat Fluxes for 3 Meter Multiyear Ice.	118

Table 18	Daily Total Heat Fluxes.	120
Table 19	Daily Salt Flux Densities for First Year Ice.	122
Table 20	Daily Salt Fluxes First Year Ice.	124
Table 21	Daily Salt Fluxes for Multiyear Ice.	126
Table 22	Daily Total Salt Fluxes.	128

Acknowledgments

I would like to express my appreciation to the members of my thesis advisory committee without whose help and encouragement this thesis would never have been possible. The members included Dr. Keith Echelmeyer, Dr. Joe Niebauer, Dr. Bill Stringer, Dr. Gerd Wendler, Dr. Gunter Weller and my principal advisor and Committee Chair, Dr. Willy Weeks. I would also like to thank a number of members of the staff of the Geophysical Institute for their advice on a variety of problem areas discussed in the thesis: Sue Ann Bolling, Richard Glenn, Rick Guritz, Shusun Li, Lew Shapiro, and Walter Rutherford. I would like to acknowledge the outstanding research of Dr. Gordon Cox, Dr. Gary Maykut and Dr. Norbert Untersteiner whose publications on the growth and properties of sea ice established the base upon which much of my thesis was built.

I would specially like to thank Dr. Weeks for giving me a variety of timely and pertinent suggestions and for helping me to find my way through the maze that people refer to as the geophysics of Arctic sea ice. His guidance was of immeasurable value.

This study would not have been possible without the support of NASA Training Grant NGT-50534 and the NASA Graduate Student Research Program. The thesis also includes field observations made at Barrow, Alaska on work supported by the Division of Polar Programs of the National Science Foundation on their grant DPP-8721977 and by the Office of Naval Research on Grant N00014-92-J-1429.

Chapter 1 General introduction

1.1 Dissertation Objectives

This dissertation is a study of several different aspects of the geophysics of sea ice. The first chapter sets the stage for what is to follow by briefly discussing some of the overall attributes of sea ice and why sea ice is currently of interest to the scientific community. Of particular interest here is the role sea ice plays in important regional and global interactions that effect the health of our planet. Also discussed is the role that remote sensing can play in exploring aspects of these interactions.

Chapter 2 investigates the surface energy balance of sea ice and further develops a growth model that is capable of estimating important properties of undeformed sea ice sheets. This chapter also discusses the physical properties of both first year and multiyear ice and how these properties change with time.

Chapter 3 is a theoretical discussion of the interaction of sea ice and synthetic aperture radar. It develops a formalism that enables one to predict sea ice backscatter coefficients (σ^o) using the output of the growth model. It also compares these predictions with time-series measurements of σ^o for fast ice located near Barrow, Alaska using data obtained by the European Space Agency's ERS-1 satellite.

Chapter 4 uses the theories and models developed in the previous two chapters in conjunction with images from ERS-1 to determine the temporal and areal extent of the three main ice classes: open water/new ice, first year ice, and multiyear ice. This chapter also attempts to characterize the ice thickness distribution in the High Arctic during the winter months using an approach based on SAR observations.

In chapter 5 the total heat and mass fluxes for an area of $100 \times 100 \text{ km}$ centered at 81.5° N and longitude 170.0° W (see Figure 1) are calculated for October 1991 to March 1992 based on the SAR observations and the model calculations. The

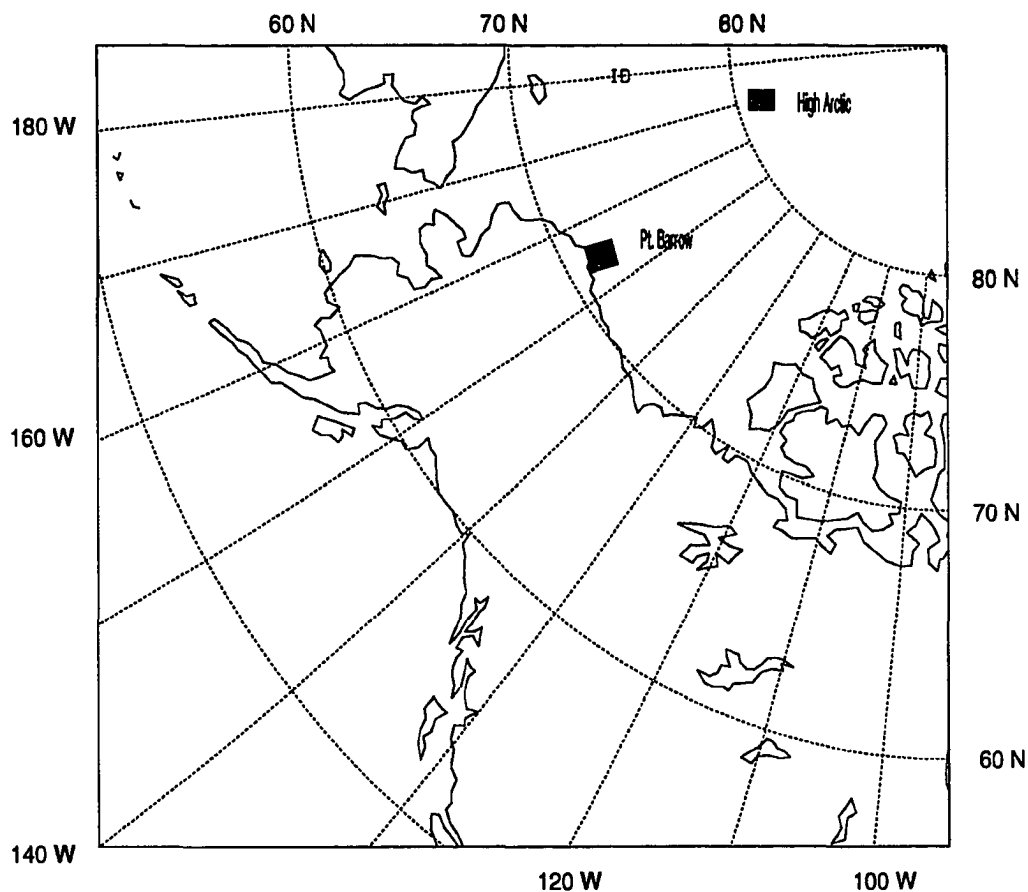


Fig. 1. Map Showing Study Areas.

estimates include the energy released to the atmosphere and the total influx of salt injected into the mixed layer of the ocean.

The final chapter 6 summarizes the findings of the previous chapters and suggests additional aspects of this general problem for future study.

1.2 Sea Ice and the Earth's Climate Machine

The earth may be viewed as a system which stores, transports and radiates energy. In a simplified view the earth is a sphere with energy entering along the equator and exiting

at the poles with the storage and transportation from the warmer equatorial regions to the colder poles generally performed by the oceanic and atmospheric advection of heat. While the atmosphere is believed to be the major contributor to this transportation process, the greater heat capacitance of the ocean makes it the main vehicle for energy storage. These processes may be seen in the weather patterns of the atmosphere and in the circulation of the ocean.

To better understand this view of the earth one must look at how the sun's radiation interacts with the varied components of the planet's surface and atmosphere. The solar radiation that reaches the upper layers of the atmosphere is either absorbed, reflected or transmitted depending on the characteristics of that particular part of the atmosphere. For example, water vapor in the form of high cirrus clouds tends to reflect much of the solar radiation, while the absence of water in the atmosphere creates an environment that transmits the radiation to lower levels.

The same type of situation occurs at the Earth's surface where the presence of ice and snow may lead to much of the radiation being reflected while the presence of open water or bare land leads to greater absorption. The reflection process generally reduces the amount of absorption and subsequent heat storage. This is generally true when the energy entering the system is at a different wavelength than the energy exiting the system, as is the case for the earth. The difference is, of course, the result of the fact that the surfaces of the Earth and the Sun are at vastly different temperatures. The Sun's surface temperature of about $6,000\text{ K}$ produces a maximum intensity of radiation at $0.5\ \mu\text{m}$ which is in the blue-green range of visible light while the Earth's lower temperature of 300 K results in a black body radiation maximum in the thermal infrared band at about $9.7\ \mu\text{m}$. The difference in the two radiation maxima is the reason why the earth is said to receive its energy by shortwave radiation while losing its energy by long wave radiation.

Clearly, any substance that effects the radiation balance at the Earth's surface has the potential to effect the Earth's climate if it covers enough of the Earth's surface. Sea

ice, the ice that forms when sea water freezes, is just such a material. It is particularly important since changes in sea ice extent have the ability to effect climate, while changes in climate, in turn, have the ability to effect sea ice extent. There are complex feedbacks involved. Although sea ice only represents about 0.1% of the total volume of snow and ice on the Earth's surface, it effects an extremely large area: between 6 and 7% of the total surface of the Earth and between 10 and 12% of the total surface of the ocean. At its maximum extent, sea ice covers about 10% of both the northern and the southern hemispheres affecting a total area of $20 \times 10^6 \text{ km}^2$ in the south and $15 \times 10^6 \text{ km}^2$ in the north. This represents an area of about two times that of the contiguous 48 states in the north and three times that in the south. At minimum ice extent, areal coverage drops to 50% of the maximum in the north and to about 15% of the maximum in the south. This makes sea ice the most important transient feature affecting heat and mass exchange between the ocean and atmosphere. In fact it ranks second only to snow as the most important transient feature affecting heat and mass exchange between the Earth's surface and the atmosphere. Here it must also be remembered that the occurrence of snow on the surface of large oceanic areas is only possible because sea ice supports the snow acting as its floating platform.

As a player in the climate system, sea ice works in a variety of ways, some of which are rather surprising. Foremost, the presence of sea ice causes a major change in the albedo (α) of the surface of the sea. Considering that sea ice invariably supports some snow cover, an ice covered region will typically exhibit albedos ranging between 0.80 to 0.90 while the open ocean exhibits an albedo of approximately $0.06 - 0.15$. This results in a drastic change in the amount of shortwave radiation that is absorbed by the ocean during spring and summer when the sun is high in the sky, and sea ice is absent. As the ice is also a good insulator and its snow cover is an even better insulator, the presence of sea ice causes a major change in the transfer of heat and mass between the ocean and atmosphere from summer to winter. In winter, polar air temperatures may consistently

be below -40°C . Yet, underneath the sea ice cover at depths of a few tens of centimeters to at most a few meters, sea water temperatures are -1.8°C . These differences in air and ocean temperatures, which are only possible because of the presence of the ice cover, are among the largest naturally occurring temperature gradients to be found on the surface of the Earth if localized phenomena such as the surficial extrusion of molten magma are excluded. Moreover ice itself is a major thermal buffer with a specific heat of $2.10 \times 10^3 \text{ J kg}^{-1} \text{ K}^{-1}$ and a heat of fusion of $335. \times 10^3 \text{ J kg}^{-1}$. Therefore the freezing and melting of ice requires the exchange of large quantities of heat.

Furthermore, the presence of ice greatly modifies the other physical interactions between the atmosphere and the ocean by modifying the transfer of momentum. It also modifies the surface wave field by essentially eliminating the shorter period wave. This tends to reduce vertical mixing in the upper ocean favoring the existence of a 50-m-thick low salinity surface layer in the Arctic Ocean that forms as the result of the desalinization processes associated with ice formation and the influx of fresh water from the large rivers of northern Siberia. This low salinity, cold surface layer contributes to the decoupling between the surface and the comparatively warm (temperatures of up to $+3^{\circ}\text{C}$) but denser water directly underlying the surface layer and prevents it from affecting the ice cover, an interaction that would further decrease sea ice extent and thickness.

As sea ice rejects approximately two-thirds of the salt initially present in the sea water from which it formed, its formation corresponds to a distillation process producing a low salinity component (the ice layer) and a high salinity component (the rejected brine). Both of these components play important geophysical roles. Most of the brine which is cold, rich in CO_2 and dense sinks to the bottom and ultimately contributes to the formation of deep water in the World Ocean. Although the importance of this process in removing CO_2 from the Earth's surface is still being debated, this clearly provides a connection between short-term near-surface process and long-term deep ocean process; clearly a matter of potential climate importance. Additionally, it has been shown by

Sarmiento and Toggweiler (1984) that three-quarters of the water masses of the World Ocean acquire their properties from high latitude regions which account for only about five percent of the global ocean surface. Thus, the polar regions are an important factor in determining the overall state of the ocean.

The freshened surficial layer of sea ice and lower salinity seawater are also of considerable interest, at least in the Arctic. The discharge of this lower salinity material occurs via the East Greenland Drift Stream between Svalbard and Greenland where it represents a freshwater transport of $2800 \text{ km}^3/\text{year}$. This is a discharge that is second only to the Amazon River. Currently there is speculation that in the past this freshwater flux may have been sufficient to even stop or at least alter the convective regimes of the Greenland, Iceland and Norwegian Seas. If this proves to be true, this is a sea-ice-driven, small scale equivalent of the so-called halocline catastrophe that has been proposed for past deglaciations when large quantities of meltwater from retreating glaciers are believed to have altered convective regimes in part of the World Ocean. Needless to say, these are matters of considerable interest to climatologists.

1.3 Sea Ice and Remote Sensing

To deal with the types of problems discussed in the previous section, one needs both a thorough understanding of the geophysics of sea ice formation and decay as well as an all weather method for monitoring the behavior of large areas of pack ice. In that some of the important geophysical processes only operate on a large scale, field sampling can be very difficult being hampered by low temperatures, long periods of darkness, poor working conditions and isolated field locations. Since sea ice is essentially a surface or a near-surface phenomenon, satellite-based remote sensing would seem to be the answer to many of the observational problems. Unfortunately, until recently the remote sensing capabilities that were available lacked the resolution to observe the sea ice in adequate detail and with continuous coverage. Where there was adequate coverage,

such as with passive microwave sensors, the resolution was very coarse (≥ 10 km) and where the resolution was adequate as with visible or infrared sensors, the coverage was limited because of darkness or cloud limitations. It is only recently with the launch of the Synthetic Aperture Radar (SAR) system on the European Space Agency (ESA) satellite ERS-1 that these problems are greatly reduced. Although coverage is not as extensive as might be desired, the SAR system offers both reasonably high resolution and all-weather capability. As SAR is an active instrument supplying its own "illumination" and operating at a frequency that penetrates clouds, it is a true all-weather system. In addition, its synthetic aperture produces images with resolutions that approach those available through high resolution instruments operating in the visible range.

While SAR appears to eliminate many of the past problems of remote sensing as applied to sea ice, it creates a series of new challenges. The images that are produced represent the response of a material that we only partially understand to a frequency of electromagnetic radiation with which we are not intimately familiar. We are unlike Superman in that we do not see with X-ray or radar eyes and therefore the interpretation of SAR imagery is far from straightforward to our eyes. Previously it was believed that SAR imagery could not be directly utilized to estimate ice thickness. Ice thickness, the one parameter that every student of sea ice wants measured, was believed to be valid only if obtained from 'remote sensing' systems operating either on or within a few meters of the sea ice surface.

The research upon which this thesis is based, was an attempt to circumvent the ice thickness problem by utilizing SAR in a manner that would allow one to obtain the ice thickness distribution, or at least the thin end of the distribution, via an indirect method using a combination of both SAR and modelling. In fact, we initially hoped to utilize ERS-1 imagery to keep track of the development of leads within the moving pack ice. Once an area of open water or thin ice was identified, we proposed to track it with SAR. Knowing when the lead formed, we could calculate how thick it would be at any

future time through the use of a growth model and meteorological data. As time passed, we planned to develop an ice thickness distribution for the thinner ice classes and to produce a time series of estimated heat, moisture and salinity fluxes that could serve as input into coupled atmosphere-ice-ocean models. Unfortunately, coverage limitations as well as restrictions on the amount of imagery available to any one project, restricted our ability to identify specific lead areas for adequate periods of time. It should be mentioned here that we still believe that our initial goals should be achievable when the wide-swath imagery becomes available upon the launch of Radarsat.

If we couldn't track leads for long periods of time, was there any possibility of using short sequences of images to obtain estimates of ice thickness that could be used with an ice growth model to calculate heat and mass fluxes? To do this, one would need an adequate ice growth model that would allow one to estimate fluxes if thicknesses could be estimated. One would also have to explore the possibility of obtaining better estimates of ice thickness, at least for undeformed first-year (FY) ice, directly from backscatter measurements made via ERS-1. Could this be done? We didn't know, but we thought that, if one tried, some interesting answers might be found and that some new questions might surface. It is hoped that you will agree that this is indeed the case.

Chapter 2 Sea Ice Growth Model

2.1 Introduction

The ice growth and properties model developed in this study is an extension and combination of several different earlier models. The surface energy balance routine is based on work of Maykut and Untersteiner (1971) and Maykut (1978). The ice property routines, such as brine volume, brine salinity, bulk salinity, brine expulsion, gravity drainage and ice densities are based on work by Cox and Weeks (1975;1988a). The non-linear temperature profile and the position of the freezing interface is determined by the finite-difference model that was developed for geothermal problems by Goodrich (1974). The initialization of the growth rate for the first layer utilizes the empirical ice growth relations of Bilello (1961), while the thermal properties such as latent heat, thermal conductivity and thermal capacitance are based on work by Schwerdtfeger (1963), Ono (1975) and Yen (1981).

Many of the original programming algorithms were initially developed by Cox in Rocky Mountain Basic. In that Rocky Mountain has not proven to be a commonly used programming language, a task that had to be completed in the initial stages of this study was to recode the initial Cox/Weeks program into a language that would allow the program to be run on a workstation. The recoding was carried out in Fortran 77 and utilizes NCAR GKS Graphics. This also allowed comparisons to be made between the original program and the more flexible and realistic program that will be developed here.

2.2 Program Structure

The ice growth program has five major parts:

- 1) an initialization of the first layer,
- 2) a calculation of the surface energy balance,
- 3) a determination of the properties of the ice at different levels in the ice sheet,

- 4) a treatment of the different aspects of the desalination process, and
- 5) a finite-difference routine to estimate the changes in the temperature profile and growth rate.

Although each of the major program components accomplishes a specific task, there are rather complex interdependencies between many of the components. For example, the finite-difference routine determines the position of the freezing interface and the temperature of each layer, but to do this it requires the ice surface temperature and the thermal properties of each of the layers. The ice surface temperature is determined by the surface energy balance routine and the thermal properties of each layer are determined by subroutine calls for each property.

The basic scheme of the program is as follows:

2.2.1 Initialization

The user specifies the number of days of ice growth, the starting day relative to September 1 and the snow accumulation rate. The program then reads the meteorological conditions (air temperature, wind speed and snow fall) for the site under study and determines the air temperature for the first freezing day. It then estimates the growth rate for the initial layer of ice by determining the freezing degree-day equivalent of one time step ($1/2$ hr) for the first freezing day (relative to -1.8°C) and estimates, using the Anderson empirical formula (Anderson 1961) discussed later, the amount of ice that will grow in that time thereby establishing an initial estimated growth rate. From this growth rate, the initial salinity may be determined and the surface energy balance calculated. The surface energy balance determines the surface temperature of the ice allowing the program to calculate the brine volume, the thermal conductivity, the latent heat and the heat capacitance for that layer (Yen 1981). After the initialization has been completed, the program continues on through the normal program loop with the exception of the desalination process which only occurs if there are at least two layers (2 cm) of ice present. One layer of ice is equal to 1 cm which also the node spacing.

2.2.2 Finite-Difference Routine

The normal program loop calls a finite-difference routine that solves the Stefan Problem of heat conduction involving a phase change. It accomplishes this by substituting the moving boundary condition of the phase change interface with an apparent latent heat source term added to the heat conduction equation. It then uses a forward looking and a backward looking Gaussian elimination process to localize the phase change interface between two nodes. For the element containing the ice-seawater interface, the routine uses a technique that follows the position of the moving interface and maintains the non-linearity of the problem (Goodrich 1978).

The finite-difference model is initialized with the first layer of ice having the thermal properties calculated during the initialization procedure. The remaining layers are assumed to have the thermal properties of a mixture of ice and sea water in a ratio of 1:3 at a temperature of -1.8°C . The reasons for this will become apparent later. The program steps through each time step of 1/2 hour, locating the freezing interface and establishing the temperatures at each node. After each time step, the ice thickness is checked and the program calculates the snow thickness, determines the ice surface temperature for the next iteration and updates the ice properties for all layers.

2.2.3 Surface Energy Balance Routine

The ice surface temperature is determined by the surface energy balance equation via the use of an iterative procedure. The air temperature, wind speed and snow thickness are derived from the meteorological data and input from a file. The incoming shortwave radiation, the incoming longwave radiation and the relative humidity, for each day, are estimated from a smoothed data set. Variations in the albedo as a function of ice thickness are estimated from the field measurements of Weller (1972). The latent heat flux is then related to the surface temperature through the specific humidity (Maykut 1978). The emitted longwave radiation, the latent heat flux, the sensible heat flux and

the conducted heat flux, are then iterated as a function of the ice surface temperature until the surface energy equation is balanced.

2.2.4 Ice Properties Routine

The ice properties routine first determines the snow cover and then calls the surface energy balance routine to determine the ice surface temperature. The program calculates the growth velocity from the ice thickness and the amount of time it took to grow the new layer. It then determines the initial salt entrapment and calculates the average temperature of the new layer. Using the average temperature and the initial salt entrapped, the brine salinity and the brine volume are determined and the latent heat and the heat capacity of the new layer are calculated.

2.2.5 Desalinization Process

If the program has grown more than two layers of ice, desalination of the layers above the new layer is initiated. For each layer above the new layer, the desalination process determines the average temperature of that layer. It also recalls the average temperature of that layer the last time desalination was called. It then uses this temperature change to determine the brine salinity and brine volume change, and calculates the salinity change due to brine expulsion. The salinity of the layer is then adjusted with the expelled brine going to the layer, either above or below, containing the higher brine volume (the brine is transferred to the adjoining layer with the higher permeability).

The temperature gradient between the layers, the brine volume and the time since last desalination are also used to calculate the salinity change due to gravity drainage. If the gravity drainage from the layer above is larger than the gravity drainage of the current layer, the difference is added to the current layer. If there is a layer of ice that has a brine volume less than 50 ppt, the gravity drainage is set to zero for all those layers above it. After the thermal properties of all the layers are updated, the

program enters the finite-difference routine and continues to grow ice until the number of target days has been reached.

2.3 Detailed Model Description

2.3.1 Surface Energy Balance

2.3.1.1 Introduction

The surface energy balance routine is largely based on work by Maykut (1978) and Maykut and Untersteiner (1971). The routine uses the Newton-Raphson iterative method to establish the ice surface temperature by taking as daily inputs incoming longwave radiation, incoming shortwave radiation, relative humidity, air temperature, wind speed and snow accumulation. It then determines the ice surface temperature by balancing the energy fluxes at the ice surface according to the following formula, valid for freezing conditions:

$$(1 - \alpha) F_r - I_o + F_l - F_E + F_s + F_e + F_c + F_o = 0 \quad (2.1)$$

where

F_r = incoming shortwave radiation,

αF_r = reflected shortwave radiation where α is the ice albedo,

I_o = net influx of radiation passing into the interior of the ice,

F_l = incoming longwave radiation,

F_E = emitted longwave radiation,

F_s = sensible heat flux,

F_e = latent heat flux,

F_c = conductive heat flux,

F_o = oceanic heat flux.

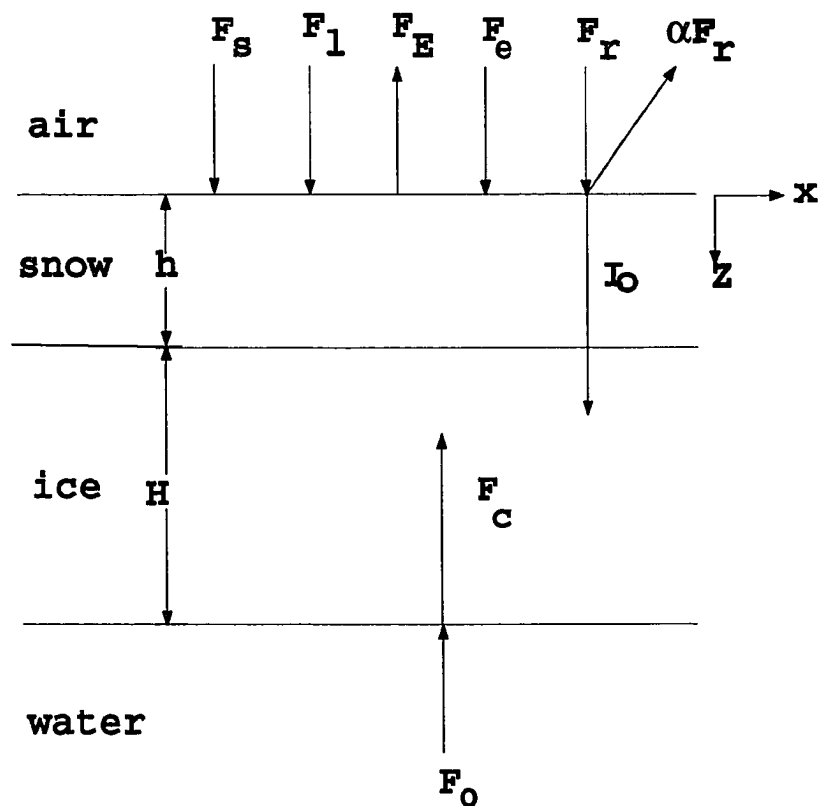


Fig. 2. Energy Flux Indices for Atmosphere-Ice-Ocean.

The convention that a flux towards the surface is positive (figure 2) will be followed here.

2.3.1.2 Incoming Shortwave Radiation (F_r)

The incoming shortwave radiation (F_r) values were taken from the monthly values given by Marshunova (1961). Each value was assumed to be representative of the middle of each month. Daily values were obtained by applying a polynomial smoothing function to the monthly values following the procedures of Maykut and Untersteiner

(1971). In that the origin of F_r is the sun which has a surface temperature of roughly 6000 K, the wavelength of the radiant energy peak λ_{max} (in μm) can be calculated from Wien's Displacement Law

$$\lambda_{max} = \frac{2.89}{T_o} \times 10^{-3} \quad (2.2)$$

giving a value of 0.5 μm .

2.3.1.3 Net Influx of Radiation to the Interior of the Ice (I_o)

The net influx of radiation (I_o) passing into the interior of the ice becomes

$$I_o = i_o (1 - \alpha) F_r \quad (2.3)$$

Based on measurements by Weller (1972), the albedo of the ice can be represented by a polynomial that is a function of the ice thickness H and is given by

$$\alpha = \beta_o + \beta_1 H + \beta_2 H^2 + \beta_3 H^3 \quad (2.4)$$

where H is in cm and

$$\beta_0 = 2.386 \times 10^{-1}$$

$$\beta_1 = 6.015 \times 10^{-3}$$

$$\beta_2 = -4.882 \times 10^{-5}$$

$$\beta_3 = 1.267 \times 10^{-7}$$

For ice thicker than 100 cm , α is 0.47. The suggestion by Maykut and Untersteiner (1971) that the net influx of radiation into the ice (i_o) is approximately 17% of the net shortwave radiation will be adopted here. This value of 17% is based on temperature profile

observations made during the melt season by Untersteiner (1964) and a heat balance suggested by Fletcher (1965). It is in conflict with Untersteiner's own estimate of 32% and is an area that needs further study. In that this study is largely concerned with the ice growth period when F_r values are near zero, this is not an major consideration here.

2.3.1.4 Incoming Longwave Radiation (F_l)

The values for the incoming longwave radiation (F_l) were also taken from Marshunova (1961) and treated in the same manner as the incoming shortwave radiation. That is, they were fit with a smoothing polynomial.

2.3.1.5 Emitted Longwave Radiation (F_E)

The emitted longwave radiation is given by the Stefan-Boltzmann Law,

$$F_E = \epsilon \sigma T_o^4 \quad (2.5)$$

where ϵ is the emissivity of the material, σ is the Stefan-Boltzmann constant ($5.67 \times 10^{-8} \text{ W m}^{-2} \text{ K}^{-4}$) and T_o is the ice surface temperature in degrees Kelvin. In the specific cases considered here, ϵ is the longwave emissivity of the surface layer of ice or snow and is taken to be equal to 1. In that the Earth's average surface temperature is of the order of 250 K, equation (2.2) indicates that the radiation emitted by the Earth will have a peak wavelength of roughly 12 μm .

2.3.1.6 Sensible Heat Flux (F_s)

The sensible heat flux is estimated by

$$F_s = \rho_a C_p C_s u (T_a - T_o) \quad (2.6)$$

ρ_a the average air density (1.3 kg m^{-3}),

C_p the specific heat at constant pressure ($1006 \text{ J kg}^{-1} \text{ K}^{-1}$),

C_s the sensible heat transfer coefficient (0.003),

u the wind speed in $m s^{-1}$, and

T_o and T_a the ambient and ice surface temperatures in degrees Kelvin.

2.3.1.7 Latent Heat Flux (F_e)

The latent heat flux (F_e) is calculated from equation (2.7)

$$F_e = \rho_a L C_e u (q_a - q_o) \quad (2.7)$$

which contains the following parameters

ρ_a the average density of the air ($1.3 kg m^{-3}$),

L the latent heat of vaporization ($J kg^{-1}$),

C_e the evaporation coefficient (0.00175),

u the wind speed, and

$q_a - q_o$ the specific humidities at some reference level above the ice q_a (in this case at 10 m) and at the surface q_o .

In equation 2.7 the latent heat of vaporization can be calculated from

$$L = [2.5 \times 10^6 - 2.274 \times 10^3 \times (T_a - 273.15)] \quad (2.8)$$

where L is again expressed in $J kg^{-1}$ and T_a is in degrees Kelvin. The difference in specific humidity can be calculated using a relation obtained by Maykut (1978)

$$(q_a - q_o) = \frac{0.622}{p_o} \times [a (f T_a^4 - T_o^4) + b (f T_a^3 - T_o^3) + c (f T_a^2 - T_o^2) + d (f T_a - T_o) + e (f - 1)] \quad (2.9)$$

where p_o is the surface atmospheric pressure (1013 millibars), f is the relative humidity, and a, b, c, d , and e are experimentally determined constants

$$a = 2.7798202 \times 10^{-6} (K^4)$$

$$b = -2.6913393 \times 10^{-3} (K^3)$$

$$c = 9.7920849 \times 10^{-1} (K^2)$$

$$d = -1.5863779 \times 10^2 (K)$$

$$e = 9.6531925 \times 10^3.$$

2.3.1.8 Conductive Heat Flux (F_c)

The conductive heat flux can be calculated from

$$F_c = \frac{k}{H} (T_b - T_o) \quad (2.10)$$

where H is the ice thickness in meters, T_b is the temperature of the ice-water interface ($-1.8^\circ C$). The thermal conductivity (k) of the surface ice layer of sea ice, or of any other layer, may be calculated using a relation developed by Ono (1975)

$$k = k_i (1 - V_b) + k_b V_b \quad (2.11)$$

where k_i ($Wm^{-1}K^{-1}$) is the conductivity of pure ice, equal to

$$k_i = 4.186 \times 10^4 \times [5.35 \times 10^{-3} - 2.568 \times 10^{-5} (T_i - 273.15)]. \quad (2.12)$$

The thermal conductivity of the brine (k_b) is

$$k_b = 4.186 \times 10^4 \times [1.25 \times 10^{-3} + 3.0 \times 10^{-5} \times (T_i - 273.15) + 1.4 \times 10^{-7} \times (T_i - 273.15)^2]. \quad (2.13)$$

The relative brine volume (V_b/V) can be calculated from

$$\frac{V_b}{V} = \frac{\rho S_i}{F_1(T)} \quad (2.14)$$

where ρ is the bulk density in $Mg\ m^{-3}$ and can be determined from

$$\rho = \frac{\rho_i \rho_b S_b}{[\rho_b S_b - S_i (\rho_b - \rho_i)]} \quad (2.15)$$

where S_i is the salinity of the ice in *ppt*, and values for $F_I(T)$ are obtained from a least-squares polynomial fitted to experimental data (Cox and Weeks, 1983)

$$F_I (T_i) = \alpha_0 + \alpha_1 T_i + \alpha_2 T_i^2 + \alpha_3 T_i^3 \quad (2.16)$$

where

$$\alpha_0 = -4.732 \quad -2 \geq T_i \geq -22.9$$

$$\alpha_1 = -2.245 \times 10^{+1} \quad -2 \geq T_i \geq -22.9$$

$$\alpha_2 = -6.397 \times 10^{-1} \quad -2 \geq T_i \geq -22.9$$

$$\alpha_3 = -1.074 \times 10^{-2} \quad -2 \geq T_i \geq -22.9$$

or

$$\alpha_0 = -9.899 \times 10^3 \quad -22.9 \geq T_i \geq -30$$

$$\alpha_1 = 1.309 \times 10^3 \quad -22.9 \geq T_i \geq -30$$

$$\alpha_2 = 5.527 \times 10^1 \quad -22.9 \geq T_i \geq -30$$

$$\alpha_3 = 7.160 \times 10^{-1} \quad -22.9 \geq T_i \geq -30$$

The change in the coefficients at $-22.9^\circ C$ is the result of the fact that this is the temperature where the solid salt $NaCl \cdot 2H_2O$ crystallizes from the brine included in the sea ice. Since $V/F_I(T) = \rho_b S_b$, the brine volume V_b can be determined from

$$V_b = \frac{\rho S_i}{\rho_b S_b} \quad (2.17)$$

Table 1. Table of Snow Accumulation Options.

OPTION	Sept. - Oct.	Nov. - Apr.	May	TOTAL
0	0	0	0	0
1	0 - 10 cm	10 - 15 cm	0 cm	15 cm
2	0 - 20 cm	20 - 25 cm	0 cm	25 cm
3	0 - 30 cm	30 - 35 cm	0 cm	35 cm
8	% of total snow accumulation			
9	actual snow accumulation	actual snow accumulation	actual snow accumulation	actual snow accumulation

2.3.1.9 Oceanic Heat Flux (F_o)

The oceanic heat flux, while an important component of the energy equation has not been adequately parameterized at this time. Estimated values range from less than $1 W m^{-2}$ to over $40 W m^{-2}$ depending upon the location and the time of year. Although the model is capable of handling variable oceanic heat fluxes, for the lack of a better parameterization a constant value of $2 W m^{-2}$ will be used in the present simulations.

2.3.1.10 Snow

The model is capable of handling snow cover in several different ways. The basic assumptions for snow are that for an ice thickness H , with a total snow thickness h and with the thermal conductivities of ice and snow given by k_i and k_s , the temperature at the snow/ice interface T_i can be calculated from

$$T_i = \frac{h k_i T_b + H k_s T_o}{h k_i + H k_s} \quad (2.18)$$

where T_o is the surface temperature of the snow. The thermal conductivity of the snow is assumed to be $k_s = 0.31 W m^{-1} K^{-1}$, and its albedo is taken as $\alpha = 0.8$.

There are five snow options available with three standard accumulation rates (Table 1). Options 1, 2 and 3 are standardized snow accumulation rates which follow ramp functions according to Table 1. Option 9 uses the actual snow fall, while option 8 allows the user to define the accumulated snow as a percentage of the actual snow fall. Phrased another way, in option 9 the snow only accumulates and does so at the measured rate while option 8 accumulates snow at some percentage of the actual. Option 8 was introduced here because, while the actual amount of snow that fell at a given location may occasionally have been measured, the amount that accumulates on the ice may be appreciably different as a result of wind-induced drifting as well as a number of other possible factors. Unfortunately, of the many things that we do not know about sea ice, one of the most glaring problems is the absence of quantitative data on the temporal and spatial distribution as well as the thermal properties of its snow cover. Therefore, all computer simulations in this study are run with zero accumulated snow fall unless stated otherwise.

2.3.2 Ice Properties

2.3.2.1 Introduction

The following additional ice properties routines are described in the following section:

initial sea ice salinity,
brine salinity,
brine density,
latent heat of fusion, and
heat capacitance.

2.3.2.2 Initial Salt Entrapment

The initial salinity of an ice layer is determined by the growth rate and the salinity of the underlying seawater. The initial salinity of the ice (S_i) is given by

$$S_i = k_{eff} S_w \quad (2.19)$$

where k_{eff} is the effective distribution coefficient and S_w is the salinity of the underlying seawater. The effective distribution coefficient may be estimated from the experimental work of Cox and Weeks (1975), who studied salt entrapment using radioactive sodium as a tracer. The relation that they suggested

$$k_{eff} = \left[\frac{0.26}{0.26 + 0.74 \exp(-7243 V)} \right] \quad (2.20)$$

is valid for growth velocities greater than $3.6 \times 10^{-5} \text{ cm s}^{-1}$. Here V is the sea ice growth velocity in cm s^{-1} . For lower values of V between 3.6×10^{-5} to 2.0×10^{-6} , the distribution coefficient is given by

$$k_{eff} = 0.8925 + 0.0568 \ln V \quad (2.21)$$

Finally, for velocities less than $2.0 \times 10^{-6} \text{ cm s}^{-1}$ the distribution coefficient is assumed to be constant with a value of 0.12.

2.3.2.3 Brine Salinity

The brine salinity may be calculated from equations derived by Cox and Weeks (1986)

$$S_b = \alpha_0 + \alpha_1 T_i + \alpha_2 T_i^2 + \alpha_3 T_i^3 \quad (2.22)$$

where T_i is the ice temperature ($^{\circ}\text{C}$) and S_b is the brine in ppt.

$$\alpha_0 = -3.9921 \quad -2 \geq T_i \geq -22.9$$

$$\alpha_1 = -22.700 \quad -2 \geq T_i \geq -22.9$$

$$\alpha_2 = -1.0015 \quad -2 \geq T_i \geq -22.9$$

$$\alpha_3 = -0.019956 \quad -2 \geq T_i \geq -22.9$$

or

$$\alpha_0 = 206.24 \quad -22.9 \geq T_i \geq -44$$

$$\alpha_1 = -1.8907 \quad -22.9 \geq T_i \geq -44$$

$$\alpha_2 = -0.060868 \quad -22.9 \geq T_i \geq -44$$

$$\alpha_3 = -0.0010247 \quad -22.9 \geq T_i \geq -44$$

2.3.2.4 Brine Density

The brine density (ρ_b) can be calculated from an equation by Zubov (1945)

$$\rho_b = 1 + cS_b \quad (2.23)$$

where c is a constant ($0.0008 \text{ Mg m}^{-3} (\text{ppt})^{-1}$).

2.3.2.5 Latent Heat of Fusion

The latent heat of fusion, expressed in J kg^{-1} , for sea ice can be calculated from a relation given by Yen (1981)

$$L = [79.69 - 0.505 T_i - 27.3 S_i + 4311.5 \left(\frac{S_i}{T_i} \right)] \times 4188 \quad (2.24)$$

with T_i the temperature of the ice ($^{\circ}\text{C}$) and S_b is the salinity (ppt).

2.3.2.6 Heat Capacitance

The heat capacitance (HC) of sea ice is

$$HC = C_s \rho_i = \frac{S_i L}{0.0182 \times T_i^2} - \frac{S_i}{0.0182 \times T_i} (C_w - C_i) + C_i \quad (2.25)$$

where $C_w = 4.23 \times 10^3 \text{ (J kg}^{-1} \text{ } ^{\circ}\text{C}^{-1})$ and $C_i = 2.01 \times 10^3 \text{ (J kg}^{-1} \text{ } ^{\circ}\text{C}^{-1})$.

2.3.3 Desalinization Process

2.3.3.1 Introduction

Natural sea ice shows a wide range of salinities ranging from as high as *20 ppt* in newly-formed ice to near *0 ppt* in the upper parts of old multiyear floes. The exact values are affected by a variety of processes including the amount of salt initially entrapped (see Section 2.3.2.2), brine expulsion, gravity drainage, brine pocket migration, and if the ice survives a melt season, by flushing.

The two dominant mechanisms involved in the desalination process of first year sea ice are brine expulsion and gravity drainage. Brine expulsion takes place in the ice during periods when the temperature is decreasing, reducing the volume of the individual brine pockets and increasing the fluid pressure as the result of the volume increase associated with the formation of ice from liquid phase. Gravity drainage, on the other hand, is the convective response due to the density instability resulting from cold, dense brine overlying warmer, less dense brine in the interconnected brine drainage networks that exist in sea ice.

2.3.3.2 Brine Expulsion

When ice initially forms, the dendrite nature of the freezing interface results in the entrapment of salt as inclusions within the ice. These so-called brine pockets are composed of a concentrated salt solution (brine) with a composition specified only by the temperature (Assur, 1958). As the ice sheet cools, additional ice forms thereby removing water from the brine causing the remaining brine to become more saline and the volume of the remaining brine to decrease (the brine pocket becomes smaller in volume). However the ice that forms during this process occupies approximately *10%* more volume than liquid water that was replaced. Therefore, although the volume of the brine is decreasing, the total volume of ice and brine increases over that of the initial brine pocket. In that the brine pocket is encased in ice and is not free to expand, this

produces an increase in the internal pressure of the brine. If the brine pressure rises above the pressure required to cause the ice to fail in tension, a crack results allowing the brine to escape. This process has been termed brine expulsion (Bennington, 1963; Untersteiner, 1967). Equations for describing the process have been developed by Cox and Weeks (1986). For gas-free sea ice during a cooling trend the equation is

$$\frac{S_i (T_2)}{S_i (T_1)} = \left[\frac{S_b (T_2)}{S_b (T_1)} \right]^{(1-\frac{1}{\rho_i})} \left[\frac{\rho_b (T_2)}{\rho_b (T_1)} \right] \times \exp \left[\frac{c}{\rho_i \{S_b (T_1) - S_b (T_2)\}} \right] \quad (2.26)$$

where S_i is the ice salinity, S_b is the brine salinity, ρ_b is the brine density, V_b is the brine volume at temperatures T_1 and T_2 , ρ_i is the density of pure ice taken as 918 kg m^{-3} , and c is equal to $d\rho_b/dT$ (0.8 kg m^{-3}). The values of S_b and ρ_b can be calculated from information presented in Cox and Weeks (1986) as noted earlier in this paper. For warming conditions, when $T_2 > T_1$, there is no brine expulsion.

2.3.3.3 Gravity Drainage

The second mechanism of the desalination process is gravity drainage. This process occurs whenever there is a layer of more dense brine above a layer of less dense brine. For sea ice during the winter, this is nearly always the situation in that, during the ice growth season, the ice sheet is invariably warmer at the bottom than at the top. Since the brine density and brine volume are functions of temperature, this positive temperature gradient (downward) causes the brine at the top of the sheet to be more dense than the warmer brine at the bottom, resulting in an unstable condition. The convective process that occurs from this instability is termed gravity drainage. Again, this process has been studied by Cox and Weeks (1975) using tracer techniques and

for brine volumes greater than 50 ppt

$$\left(\frac{\Delta S_i}{\Delta t} \right) = 1.68 \times 10^{-5} \times \left(\frac{\Delta T}{\Delta z} \right) - 3.37 \times 10^{-7} \times V_b \times \left(\frac{\Delta T}{\Delta z} \right) \quad (2.27)$$

where $\left(\frac{\Delta S_i}{\Delta t} \right)$ is the rate of change in salinity per mille per second, V_b is the brine volume and $\left(\frac{\Delta T}{\Delta z} \right)$ is the temperature gradient in degrees K per centimeter.

These equations for brine expulsion and gravity drainage were used in the ice growth program after each time step. Calculated salinity changes in a given layer were redistributed as follows. For brine expulsion the salinity change was removed from the layer and placed in the layer either above or below according to the following rules. If 90% of the brine volume of the upper layer is greater than 100% of the brine volume of the lower layer, the expelled brine is placed in the upper layer. Otherwise the brine is moved down into the lower layer. These differences in percentages were used in this scheme primarily to overcome a small oscillation of the temperature in the upper part of the ice sheet that is a by-product of the finite-difference routine. For gravity drainage, if the layer just above the current layer lost more salt than the current layer, the difference was added to the current layer. If the layer above lost less salt than the current layer, no additional salt was added.

2.3.4 Finite Difference Routine

2.3.4.1 General

The finite-difference routine for the ice growth program is based on the work of Goodrich (1978). The technique involves solving the heat conduction equation

$$\frac{\partial}{\partial t} (C T) = \frac{\partial}{\partial x} \left(k \frac{\partial T}{\partial x} \right) \quad (2.28)$$

which applies in the frozen and unfrozen regions on either side of the moving phase boundary. Here C is the heat capacity per unit volume and k is the thermal conductivity of the material. At the freezing interface ($x=z$) the following condition holds true

$$k_f \frac{\partial T}{\partial x}|_z - k_u \frac{\partial T}{\partial x}|_z = + L_v \frac{dz}{dt} \quad (2.29)$$

and

$$T(z, t) = T_f = \text{constant}$$

at the moving phase change interface. The plus (+) sign indicates a release of heat (i.e. that freezing is occurring).

In this treatment, the moving interface is replaced by a latent heat source term added to the conduction equation which leads to a heat conduction equation with an effective heat capacitance as follows.

$$\frac{\partial}{\partial t} (C_{eff} T) = \frac{\partial}{\partial x} \left(k \frac{\partial T}{\partial x} \right) \quad (2.30)$$

with

$$C_{eff} = C_u \text{ for } T > T_f$$

and

$$C_{eff} = C_f + L_v \frac{\partial \theta}{\partial T} \text{ for } T < T_f \quad (2.31)$$

where

C_{eff} is the effective heat capacity per unit volume,

C_u is the heat capacity per unit volume of the unfrozen medium,

C_f is the heat capacity per unit volume of the frozen medium

L_v is the latent heat per unit volume, and

$\theta = \theta (T, x) =$ unfrozen volumetric moisture content.

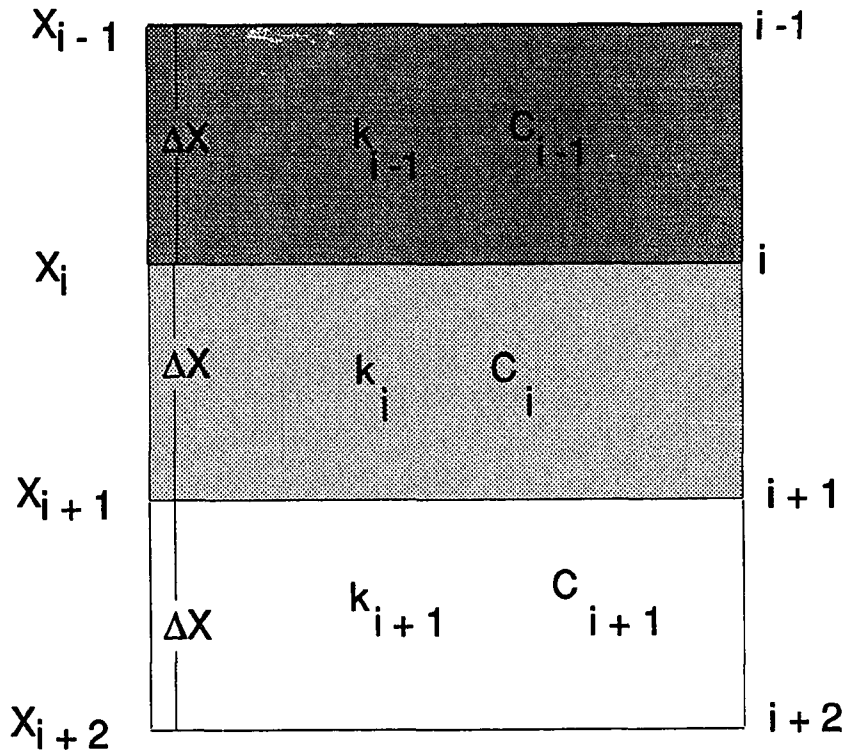


Fig. 3. Finite-Difference Grid Indices.

For a layered system with N layers (Figure 3), the difference equation may be written as

$$\begin{aligned}
 HC_i (T_i^{m+1} - T_i^m) = & \\
 CN_{i-1} (T_{i-1}^{m+1} - T_i^{m+1} + T_{i-1}^m - T_i^m) + & \quad (2.32) \\
 CN_i (T_{i+1}^{m+1} - T_i^{m+1} + T_{i+1}^m - T_i^m) &
 \end{aligned}$$

where the space indices are the subscripts (i), the time indices are the superscripts (m) and the i node temperature at time m for a time step Δt is $T_i^m = T(x_i, m\Delta t)$.

The heat capacity coefficients (HC) and the conductance coefficients (CN) are defined as

$$HC_i = \frac{(C_{i-1}\Delta x_{i-1} + C_i\Delta x_i)}{\Delta t} \quad (2.33)$$

and

$$CN_i = \frac{k_i}{\Delta x_i} \quad (2.34)$$

where k_i is the thermal conductivity of element i , C_i is the volumetric heat capacity of element i and Δx is the node spacing.

Equation 2.32 may be rearranged such that

$$\begin{aligned} & -CN_{i-1} T_{i-1}^{m+1} + \\ & (HC_i + CN_{i-1} + CN_i) \times \\ & T_i^{m+1} - CN_i T_{i+1}^{m+1} = RHS_i \end{aligned} \quad (2.35)$$

where the right-hand side (RHS_i) is equal to

$$\begin{aligned} RHS_i = & CN_{i-1} T_{i-1}^m + \\ & (HC_i - CN_{i-1} - CN_i) T_i^m \\ & + CN_i T_{i+1}^m \end{aligned} \quad (2.36)$$

These equations represent a system of linear algebraic equations which may be solved by a Gaussian elimination procedure. Since the temperatures at the upper and lower surfaces ($i=0$ and $i=N$) are known, the remaining node temperatures may be determined by using a forward and backward Gaussian elimination.

2.3.4.2 Forward Elimination

For forward elimination

$$E_o = T_o^{m+1} \quad (2.37)$$

$$S_o = 0 \quad (2.38)$$

$$E_i = \frac{(RHS_i + CN_{i-1} E_{i-1})}{D} \quad (2.39)$$

$$S_i = \frac{CN_i}{D} \quad (2.40)$$

where T_o^{m+1} is known and

$$D = HC_i + CN_{i-1} + CN_i - CN_{i-1} S_{i-1} \quad (2.41)$$

with i varying from $i=1$ to $N-1$. Once the coefficients E_i and S_i are evaluated, they may be substituted into

$$T_i^{m+1} = S_i T_{i+1}^{m+1} + E_i \quad (2.42)$$

where i is decreased from $i=N-1$ to 1 and T_N^{m+1} is a known temperature.

2.3.4.3 Backward Elimination

For backward elimination

$$E'_N = T_N^{m+1} \quad (2.43)$$

$$S'_N = 0 \quad (2.44)$$

$$E'_i = \frac{(RHS_i + CN_i E_{i+1})}{D'} \quad (2.45)$$

$$S'_N = \frac{CN_i}{D'} \quad (2.46)$$

where T_N^{m+1} is known and

$$D' = HC_i + CN_{i-1} + CN_i - CN_i S_{i+1} \quad (2.47)$$

with i decreasing from $i=N-1$ to 1 . Again, once the coefficients E'_i and S'_i are evaluated, the node temperatures may be determined from

$$T_i^{m+1} = S'_i T_{i-1}^{m+1} + E'_i \quad (2.48)$$

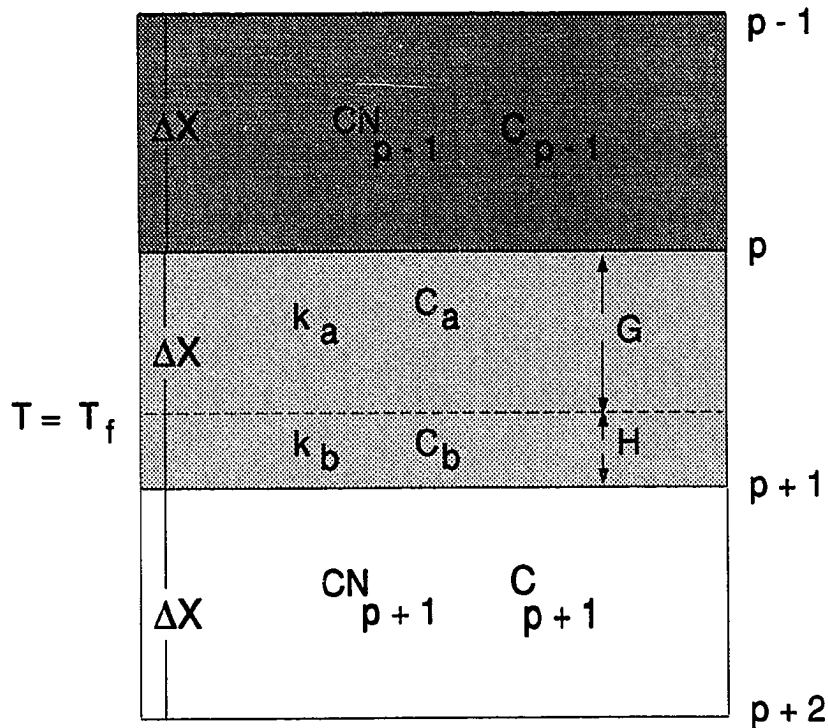


Fig. 4. Finite Difference Grid for Region Containing the Phase Boundary.

with $i=1$ to $N-1$ and T_o^{m+1} known.

The use of the forward and backward elimination localizes the phase change interface between two nodes. From here the element may be split into two regions (a and b) with thermal properties C_a, k_a and C_b, k_b (Figure 4). The heat balance at the upper node where $i=p$ is

$$\frac{(C_{p-1} \Delta x_{p-1} + C_a \bar{G}) (T_p^{m+1} - T_p^m)}{\Delta t} = \frac{CN_{p-1} (T_{p-1}^{m+1} - T_p^{m+1} + T_{p-1}^m - T_p^m) - \frac{k_a}{\bar{G}} (T_p^{m+1} + T_p^m)}{\quad} \quad (2.49)$$

where $\bar{G} = \frac{1}{2} (G^{m+1} + G^m)$ and G^{m+1} and G^m are the distances of the phase change interface from x_i at the end and beginning of the time step, respectively.

The heat balance at the lower node where $i=p+1$ is

$$\frac{1}{2} \frac{(C_{p+1} \Delta x_{p+1} + C_b \bar{H}) (T_{p+1}^{m+1} - T_{p+1}^m)}{\Delta t} = \frac{1}{2} CN_{p+1} (T_{p+2}^{m+1} - T_{p+1}^{m+1} + T_{p+2}^m - T_{p+1}^m) - \frac{1}{2} \frac{k_b}{\bar{H}} (T_{p+1}^{m+1} + T_{p+1}^m) \quad (2.50)$$

where $\bar{H} = \Delta x_p - \bar{G}$. The moving boundary condition may be approximated by the following difference equation

$$\frac{L_v (G^{m+1} - G^m)}{\Delta t} + \frac{1}{2} \left\{ \frac{1}{2} C_a (T_{p-1}^{m-1} + T_{p-1}^m) - \frac{1}{2} C_b (T_{p+1}^{m+1} + T_{p+1}^m) \right\} = \frac{1}{2} k_a \frac{(T_p^{m+1} + T_p^m)}{\bar{G}} + \frac{1}{2} k_b \frac{(T_{p+1}^{m+1} + T_p^m)}{\bar{H}} \quad (2.51)$$

The coefficients E_i and S_i can be determined from the forward elimination formula by evaluating them successively from $i=1$ to $p-1$. The heat balance equation for node $i=p$ leads to

$$E_p = \frac{CN_{p-1} (T_{p-1}^m + E_{p-1})}{C_{p-1} \frac{\Delta x_{p-1}}{\Delta t} + \frac{C_a \bar{G}}{\Delta t} + \frac{k_g}{\bar{G}} + CN_{p-1} (1 - S_{p-1})} + \frac{(C_{p-1} \frac{\Delta x_{p-1}}{\Delta t} + \frac{C_a \bar{G}}{\Delta t} - CN_{p-1} - \frac{k_g}{\bar{G}}) T_p^m}{C_{p-1} \frac{\Delta x_{p-1}}{\Delta t} + \frac{C_a \bar{G}}{\Delta t} + \frac{k_g}{\bar{G}} + CN_{p-1} (1 - S_{p-1})} \quad (2.52)$$

and the node temperature at $i=p$ becomes $T_p^{m+1} = S_p T_f + E_p$, where T_f is the phase change temperature. Using backwards elimination for the region below the freezing interface, the equations give $T_{p+1}^{m+1} = E'_{p+1}$, where E'_i and S'_i are evaluated successively from

$i=N-1$ to $i=p+2$ leading to the equation

$$E'_{p+1} = \frac{CN_{p+1} (T^m_{p+2} + E'_{p+2})}{C_{p+1} \frac{\Delta x_{p+1}}{\Delta t} + \frac{C_b \bar{H}}{\Delta t} + \frac{k_b}{\bar{H}} + CN_{p+1} (1 - S'_{p+2})} + \frac{(C_{p+1} \frac{\Delta x_{p+1}}{\Delta t} + \frac{C_b \bar{H}}{\Delta t} - CN_{p+1} - \frac{k_b}{\bar{H}}) T^m_{p+1}}{C_{p+1} \frac{\Delta x_{p+1}}{\Delta t} + \frac{C_b \bar{H}}{\Delta t} + \frac{k_b}{\bar{H}} + CN_{p+1} (1 - S'_{p+2})} \quad (2.53)$$

2.4 Meteorological Data

Model estimates of the meteorological conditions for the high Arctic were obtained from the Unidata Program Center located in Boulder Colorado. The generation of this data set is managed by the University Corporation for Atmospheric Research and is sponsored by the National Science Foundation. Unidata is a national program for providing near-real-time meteorological data to university users. The data are transmitted by a satellite downlink under contract with Zephyr Weather Information Service, Inc.

Meteorological variables of zonal and meridional wind speeds u and v (m/s), temperature T (K), geopotential height H (m), and relative humidity R (%) are available at 2.5° latitude and 5° longitude grid points. These variables are obtainable at vertical levels of 1000, 850, 700, 500, 400, 300, 250, 200, 150 and 100 mb for forecast times of 0, 6, 12, 18, 24, 30, 36, 42, 48 and 60 hours. The 0 hour forecast designates the observed (assimilated and initialized) data of the NMC Medium Range Forecast Model. The daily 0 hour and 12 hour temperature and wind forecasts at the 1000 mb vertical level were averaged and used as the inputs to the sea ice growth model for the high Arctic study area. The accuracies of these data are unknown at this time. Of general concern here are the surface temperatures which may be overestimated by several degrees due to the presence of local inversions which the numerical model fails to parameterize correctly.

Meteorological data from the NOAA Air Sampling Station located just northeast of the village of Barrow, Alaska were also used for the model calculations involving the

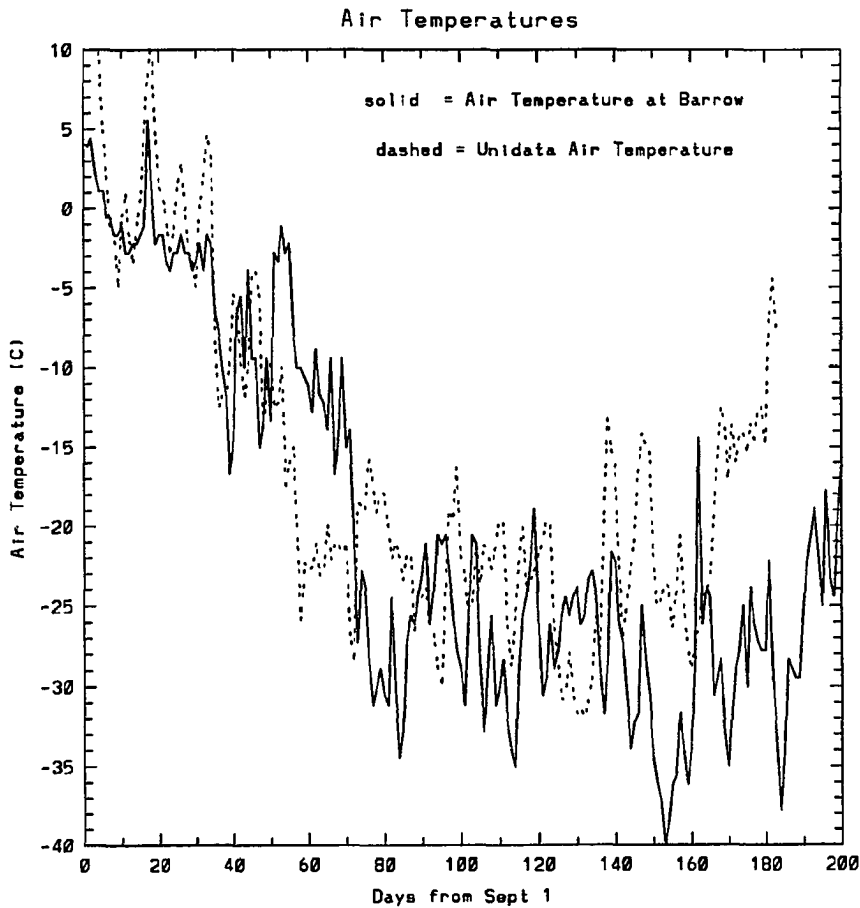


Fig. 5. Comparison of Unidata air temperatures versus NOAA Station air temperatures.

state of fast ice in the Dease Inlet/Elson Lagoon region of the Alaskan Beaufort Sea coast. Because of the nearness of the NOAA station to these fast ice sites as well as the extreme flatness of the terrain, these data are believed to be particularly representative. The mean wind and surface temperature measurements were used as the model inputs.

Figure 5 shows a plot of temperatures at Point Barrow taken from the NOAA Station and as derived from Unidata.

2.5 Model Results

2.5.1 First Year Ice

In the following section, the growth model will be used to examine some of the complex interrelations between the meteorological conditions, the amount of ice grown, and the resulting sea ice properties. Although the large scale feedbacks on a regional to global scale between sea ice and climate parameters have recently received considerable attention in the literature, it is well to note that the “simple” problem of sea ice growth also contains complex feedbacks, although on a local scale. The following figures (Figures 6 and 7) show the computer temperature, salinity and brine volume profiles for first year sea ice “grown” via the growth model using the meteorological inputs for Point Barrow, Alaska as representative of the nearby Dease Inlet as discussed above. In Figure 6 the ice was allowed to grow for 200 days beginning on 10 October 1991 (day 40) and ending on 8 May 1992 (day 240). As this was approximately the maximum length of time sea ice could have grown during this year, the resulting ice thickness of *176 cm* can be taken as representing a maximum first year ice profile for this region. Note the non-linear temperature profile with a warming temperature wave propagating downward. This figure will be referred to again in the section on the radar backscatter of sea ice.

The figure (Figure 7) shows the temperature, salinity and brine volume profiles for the same date (8 May 1992) for ice that began growing 39 days later on 18 November 1991 (day 78). When comparing these plots, the most marked difference is observed in the salinity profile. The more rapid growth rate of the ice that initially formed in November, as a result of the lower temperatures in November (-30°C) than in October (-14°C), caused an increase in the initial salt entrapment in the ice resulting in high salinity and brine volumes in the upper layers of the November ice sheet. This decreased the thermal conductivity of these layers and ultimately slowed the growth of this particular ice sheet.

The next two figures (Figures 8 and 9), which are representative of first year ice growth in the high Arctic, demonstrate the importance of the salinity and brine volume

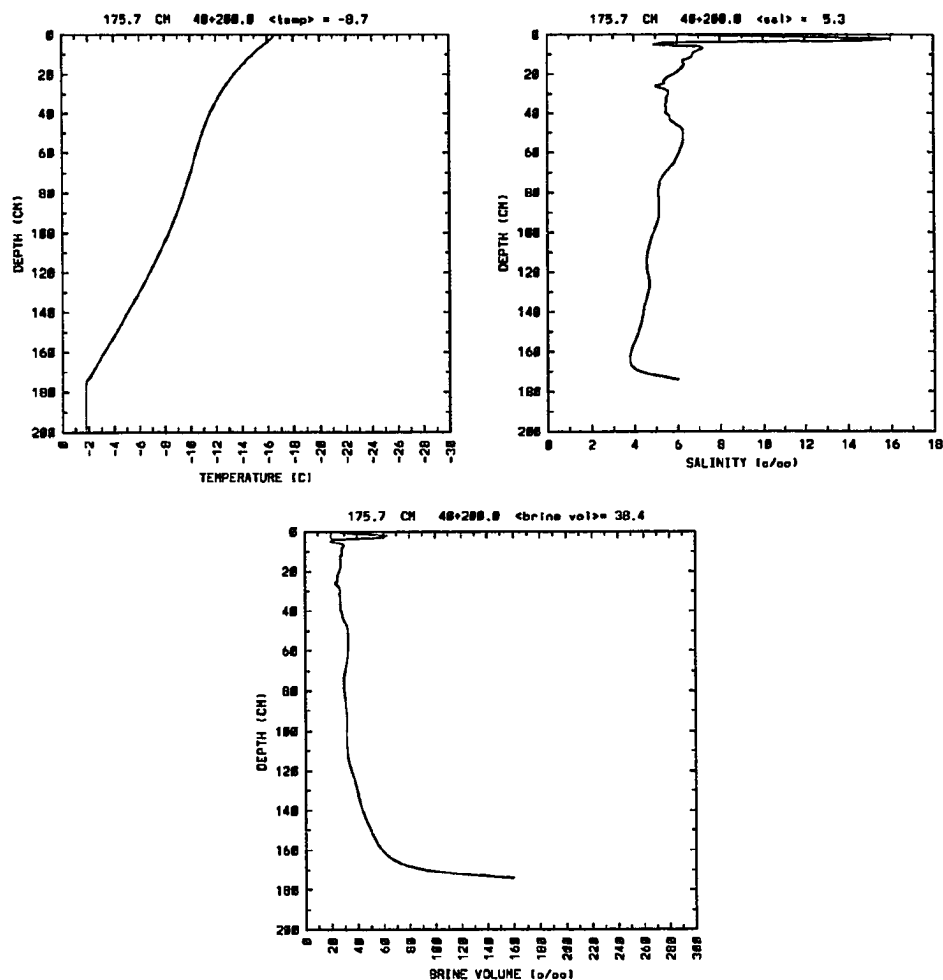


Fig. 6. Dease Inlet First Year Ice Profile 1; growth started on 10 October 1991.

profiles in determining the conducted heat flux through the ice and thus the overall thickness. They also demonstrate the curious fact that, within limits, during a period of continuous ice growth the ice sheet that formed first is not necessarily thicker, or even as thick, as an ice sheet that formed a few days later. Figure 8 shows the profiles of an ice sheet on 19 March 1992 (day 210) that began growing on 1 November 1991 (day 61) and grew for 149 days. Figure 9 shows the results for an ice sheet that began growing 2 days later (day 63) and grew 2 days less at only 147 days. The interesting

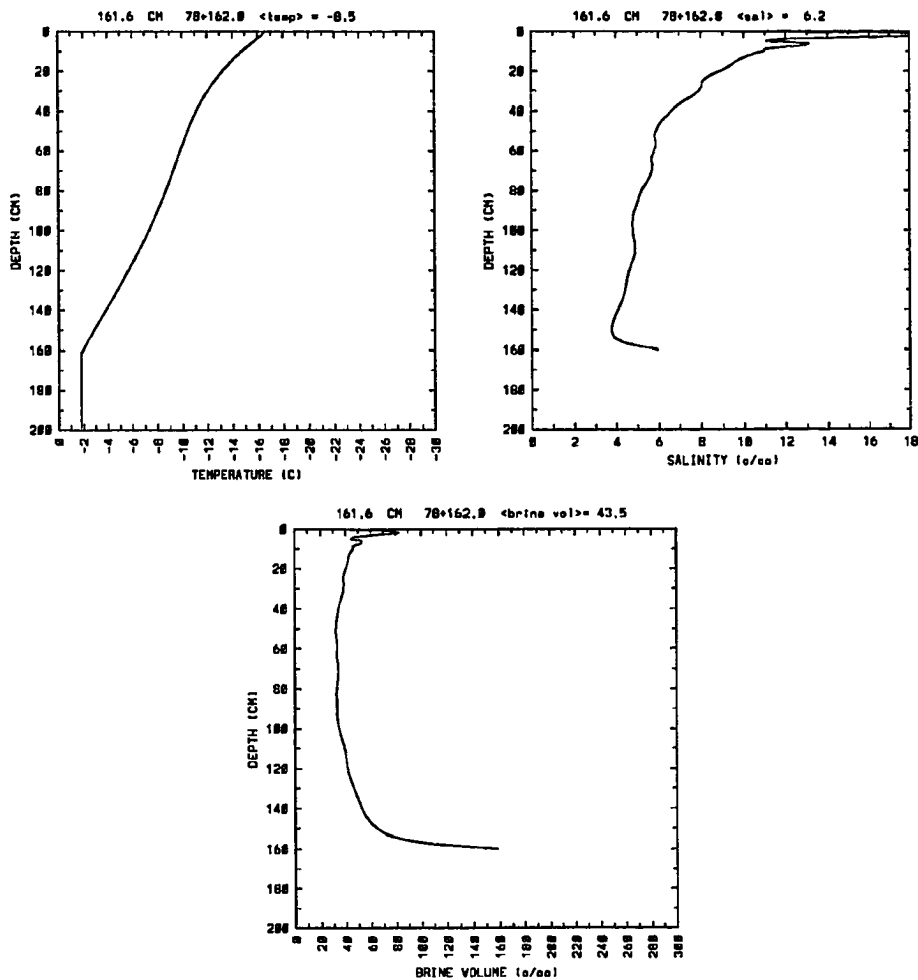


Fig. 7. Dease Inlet First Year Ice Profile 2; growth started on 18 November 1991.

point here is the fact that the ice that grew for a shorter period of time actually grew *9.4 cm (6.2%)* more ice (*149.4 cm* versus *140.0 cm*) than the ice that grew for 149 days. The reason this occurred is the result of the different meteorological conditions that took place at the onset of freezing for each ice sheet. On 1 November 1991 the temperature was -18°C with a *12 m/sec.* wind; conditions that promote rapid ice growth resulting in an initial ice layer with a very high salinity. The high salinity and resulting high brine

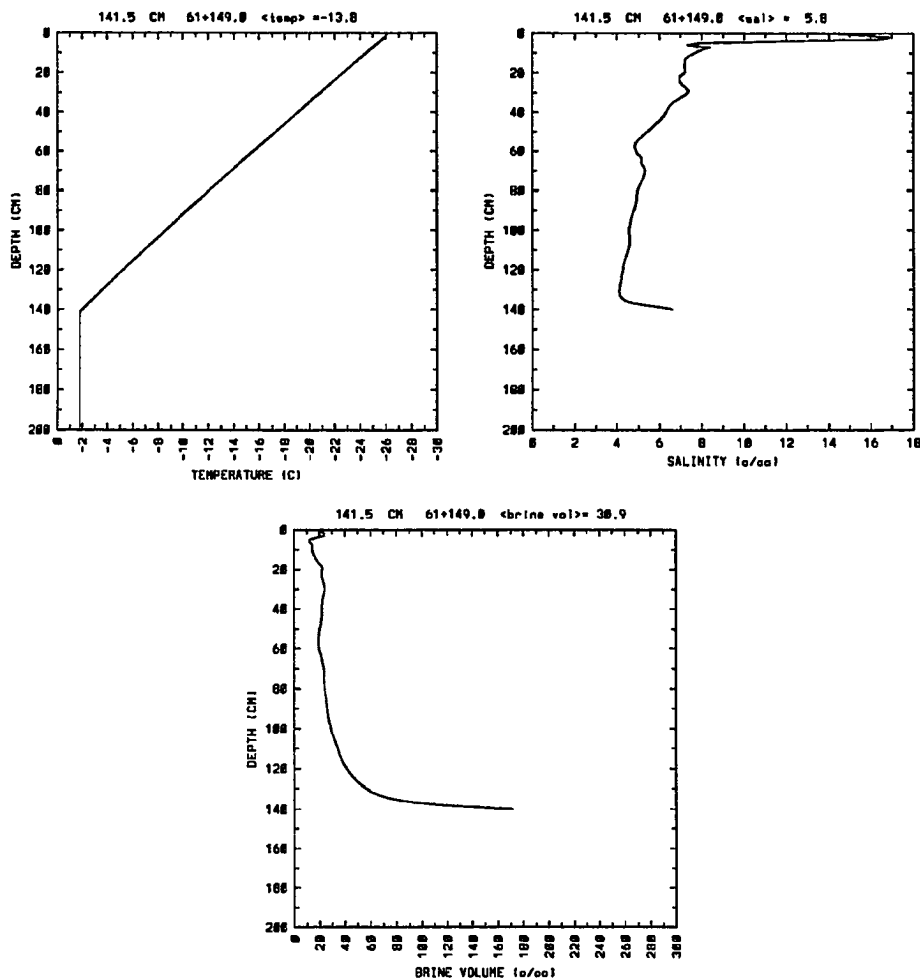


Fig. 8. High Arctic First Year Ice Profile; growth started on 1 November 1991.

volume of this initial ice would reduce the thermal conductivity thereby lowering the conducted heat flux. This, in turn, would slow subsequent ice growth.

The ice that began growing on 3 November 1991 had a temperature of -10°C with a 7 m/sec wind blowing. These are significantly less severe freezing conditions than previously encountered resulting in a lower initial growth rate. However, the fresher ice, resulting from the lower growth rate, would have an increased thermal conductivity

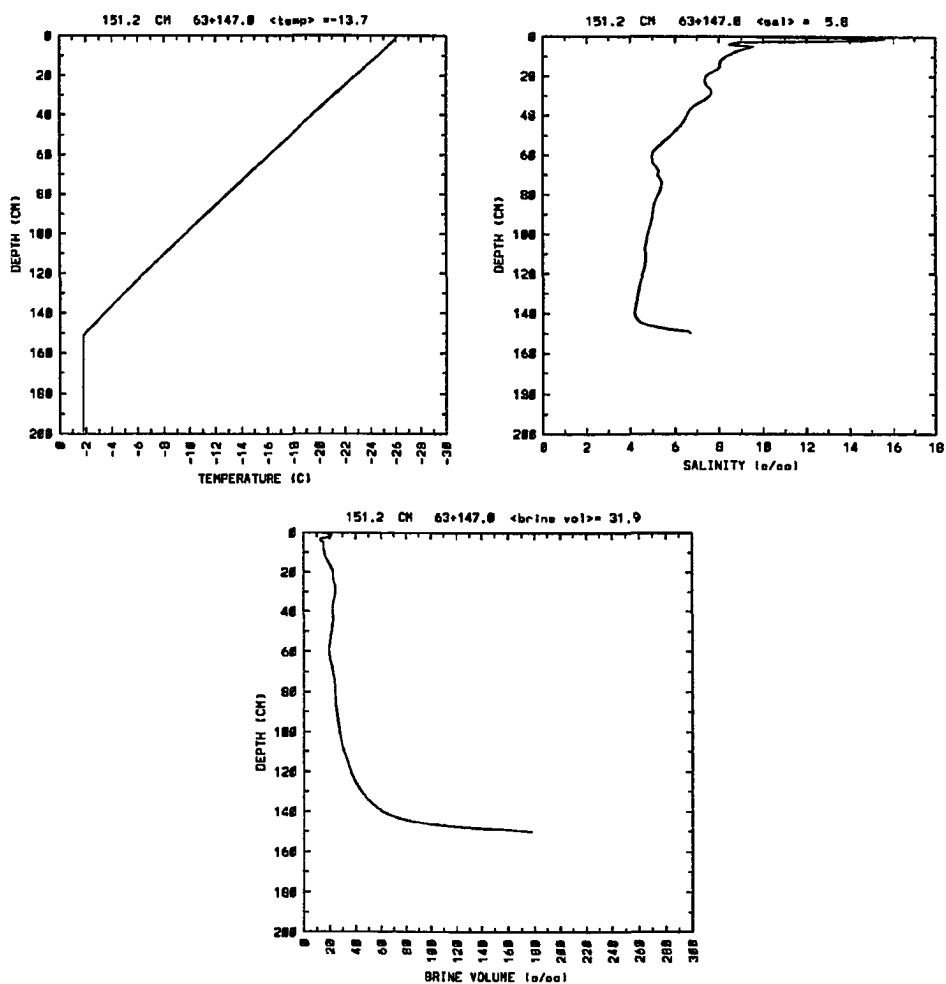


Fig. 9. High Arctic First Year Ice Profile; growth started on 3 November 1991.

thereby resulting in a higher conducted heat flux; a situation that would eventually produce a thicker ice sheet than in the previous situation.

2.5.2 Multiyear Ice

To date there have been no serious attempts to model the first year to multiyear transition. Therefore a preliminary attempt was made to explore this problem by producing an approximation of the multiyear ice formation process by growing the

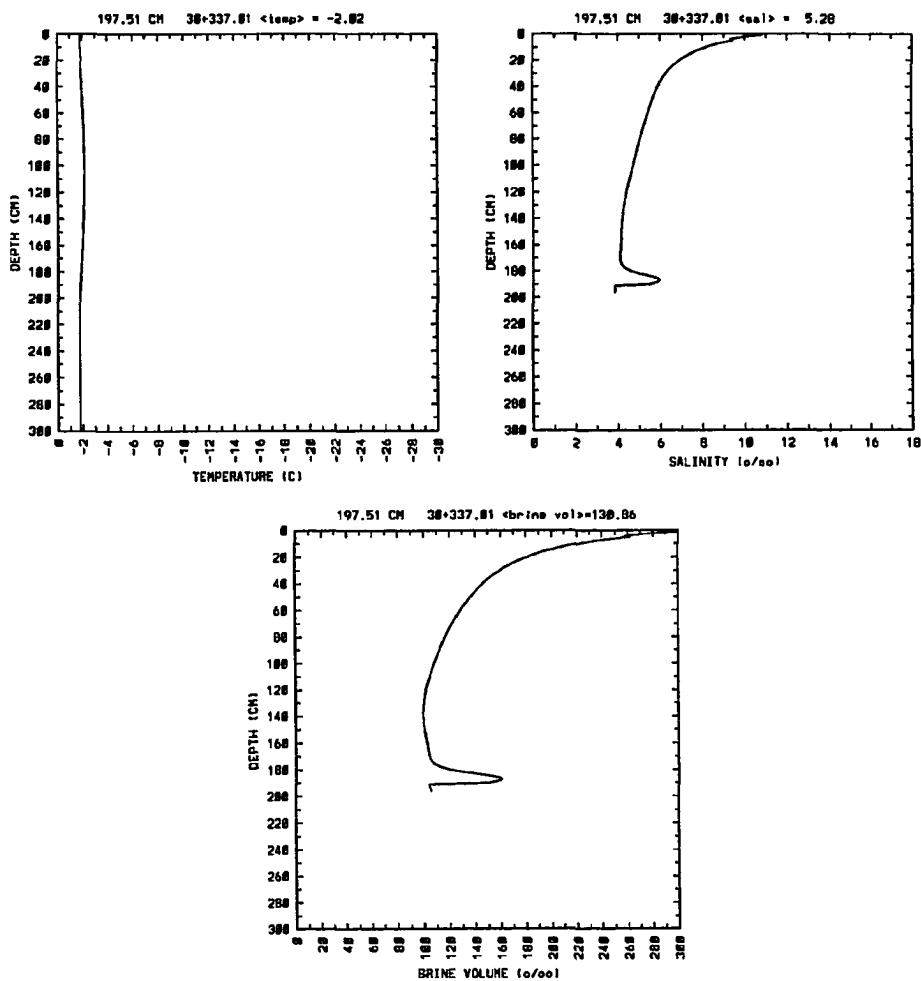


Fig. 10. Multiyear Ice on September 1 without Meltwater Desalination.

maximum amount of first year ice during the freezing season and then restricting the ice surface temperature to -5.5°C (to prevent ablation at the lower interface) during the summer months. This arrested ice growth during the summer while continuing to desalinate the ice sheet through gravity drainage. The inputs to the growth model for these simulations were smoothed average values for the central high Arctic as described earlier with the following exceptions. The summer inputs for days between 212 and 365 were held constant at their day 212 value. After day 365 the inputs for days

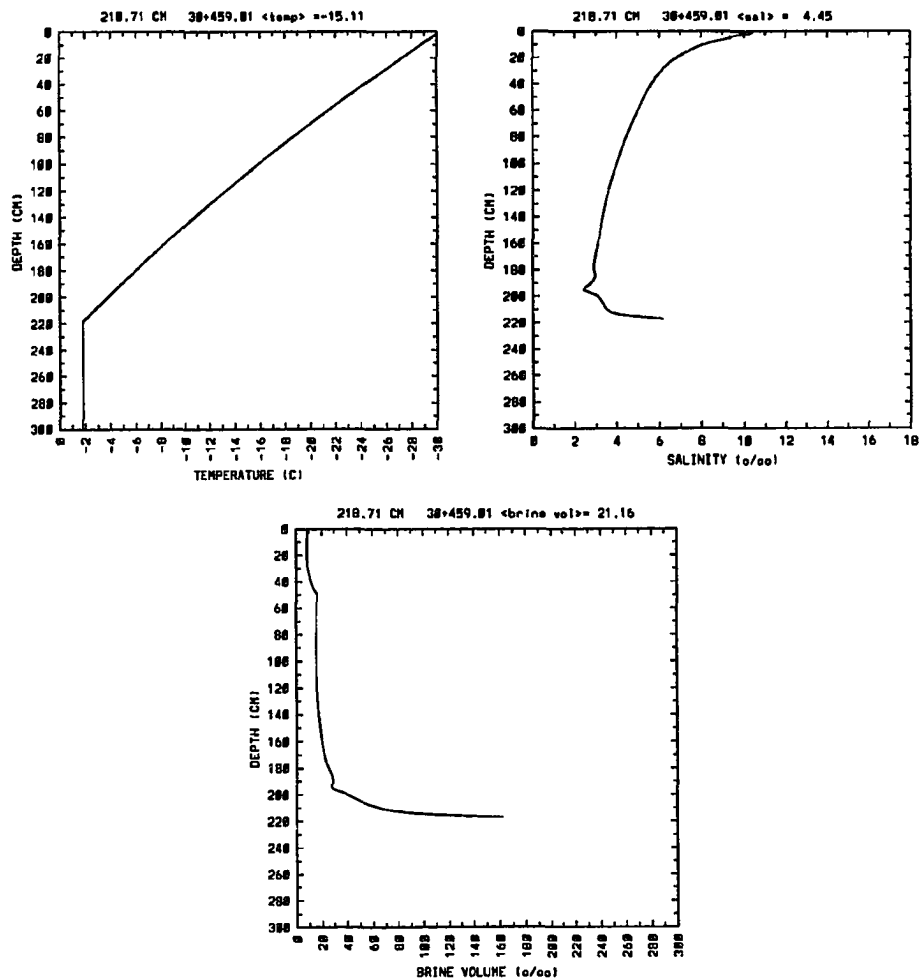


Fig. 11. Multiyear Ice on January 1 without Meltwater Desalination.

1–365 were repeated. For example, the growth model inputs for day 366 would be identical to those for day 1.

The next three figures (Figures 10, 11 and 12) show the temperature, salinity and brine volume profiles for the second year ice on 1 September, 1 January and 15 May. From Figure 10 it can be seen that the total ice thickness is 197.5 cm and the temperatures of the ice and surrounding water are nearly isothermal at -2.0 to -1.8°C . However the salinity and brine volume profiles are more typical of first year ice than multiyear ice

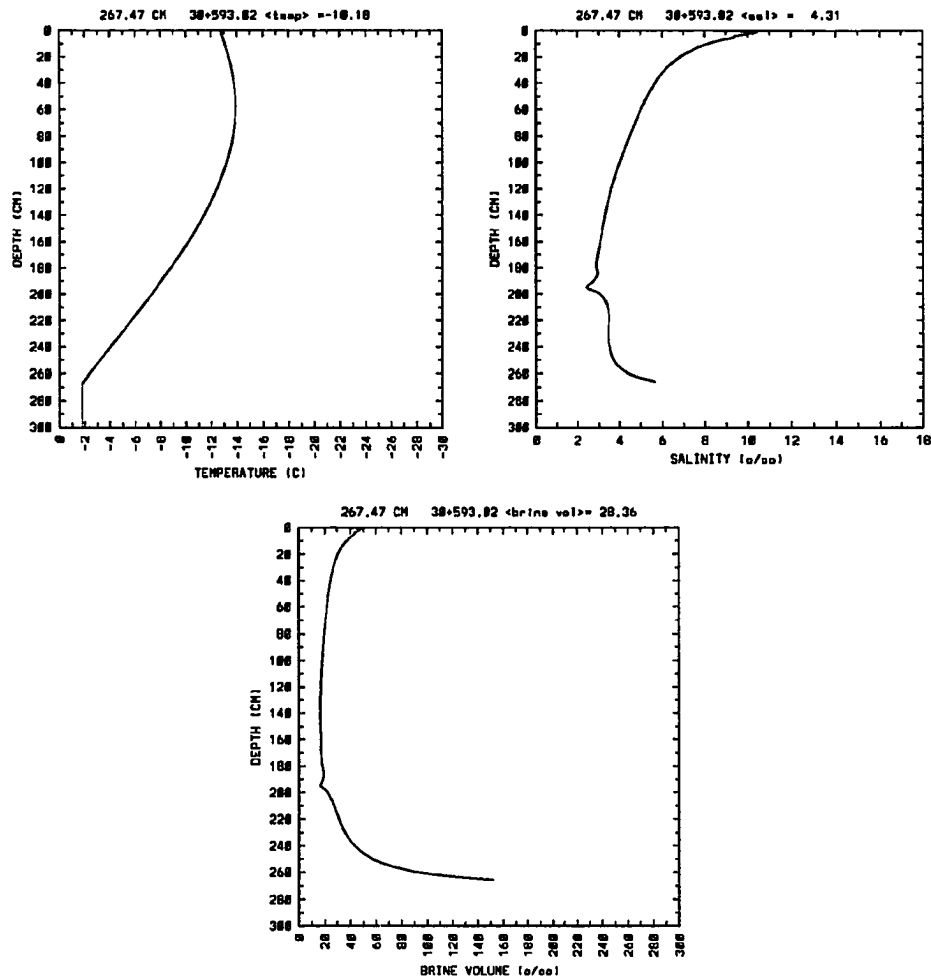


Fig. 12. Multiyear Ice on May 15 without Meltwater Desalinization.

(the small bump at the bottom of the ice is due to the small amount of growth during the summer). From the next two figures (Figures 11 and 12) it is evident that this process simply grows thicker first year ice. This result is not particularly surprising since the model is missing the desalinization processes of summer. Most notably missing is the process of flushing that occurs when a portion of the top layer melts and drains through the ice sheet. This process has been suspected of contributing greatly to the desalinization of multiyear ice (Untersteiner, 1967) and the previous simulations would

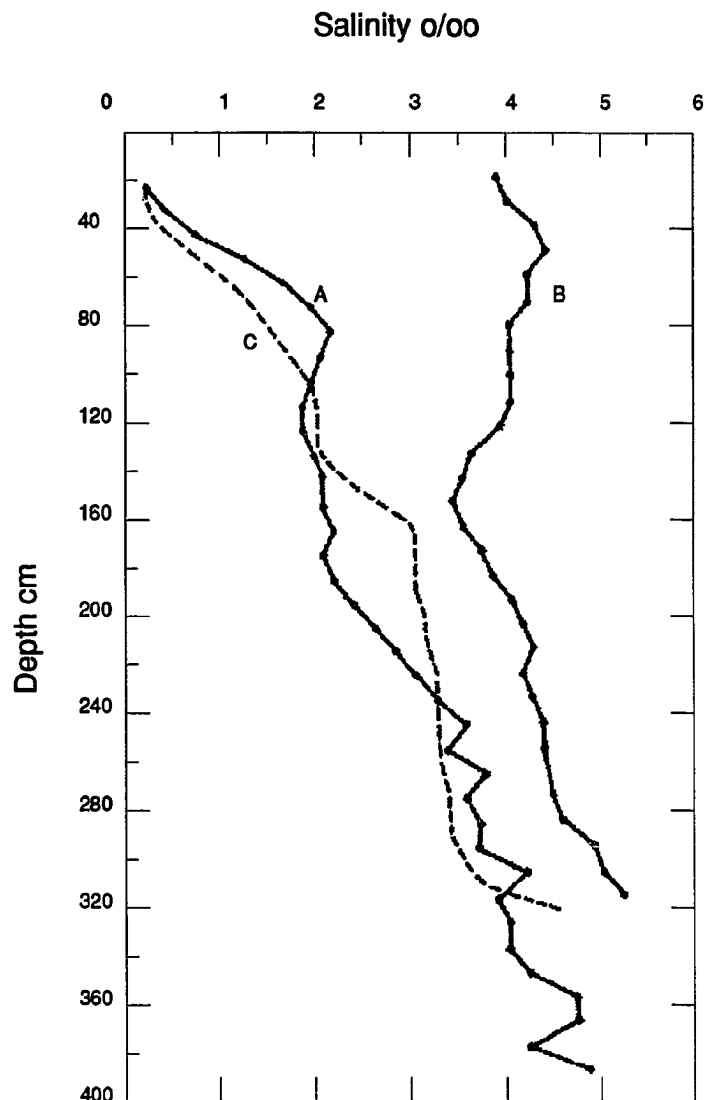


Fig. 13. Average MY Salinity Profiles for Hummocked (A), Depressed Ice (B) and Average MY Profile from Station Alpha(C). (Cox and Weeks 1975).

tend to confirm this hypothesis. Unfortunately there is no detailed formulation of this important process in the literature.

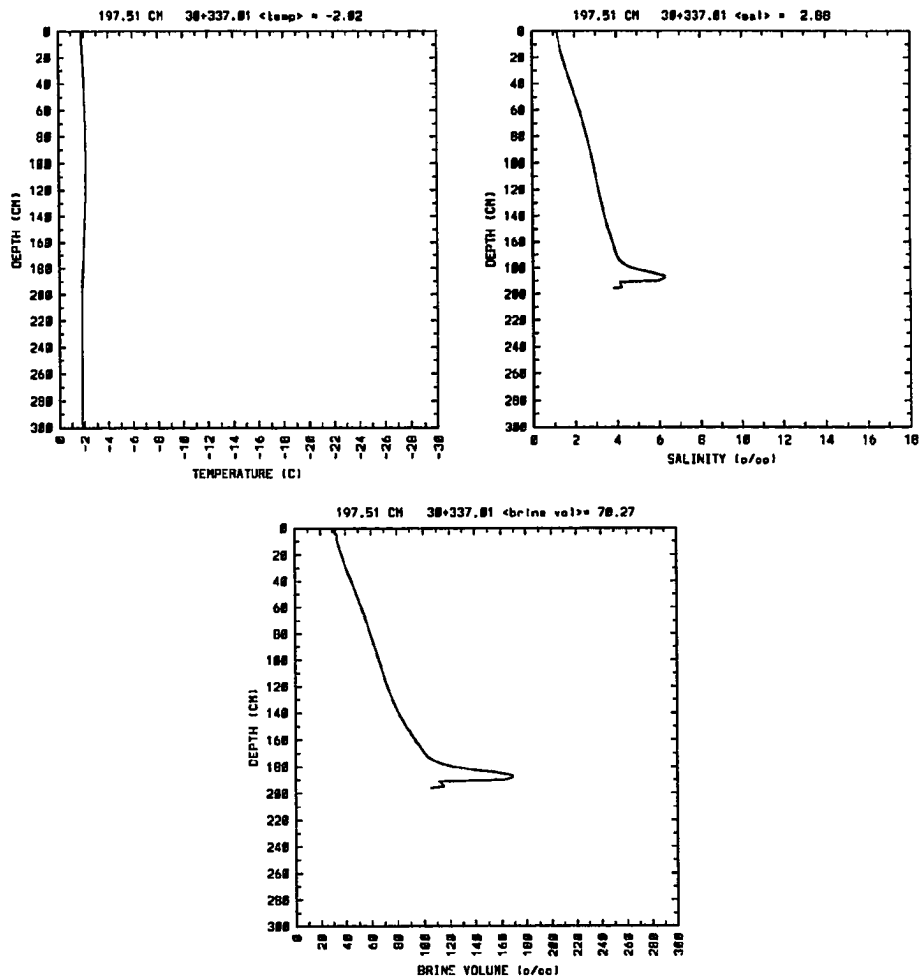


Fig. 14. Multiyear Ice on September 1 with Meltwater Desalinization.

In a completely arbitrary attempt to produce reasonable salinity and brine volume profiles, the following procedure was devised. After growing the maximum amount of first year ice during the first winter, at the end of the following summer the entire ice sheet was reduced in salinity in a linear fashion such that the top of the sheet was reduced by 90% and the bottom was reduced by 0%. This process produced salinity and brine volume profiles for the second year ice that more closely approximated those measured in multiyear ice (Figure 13).

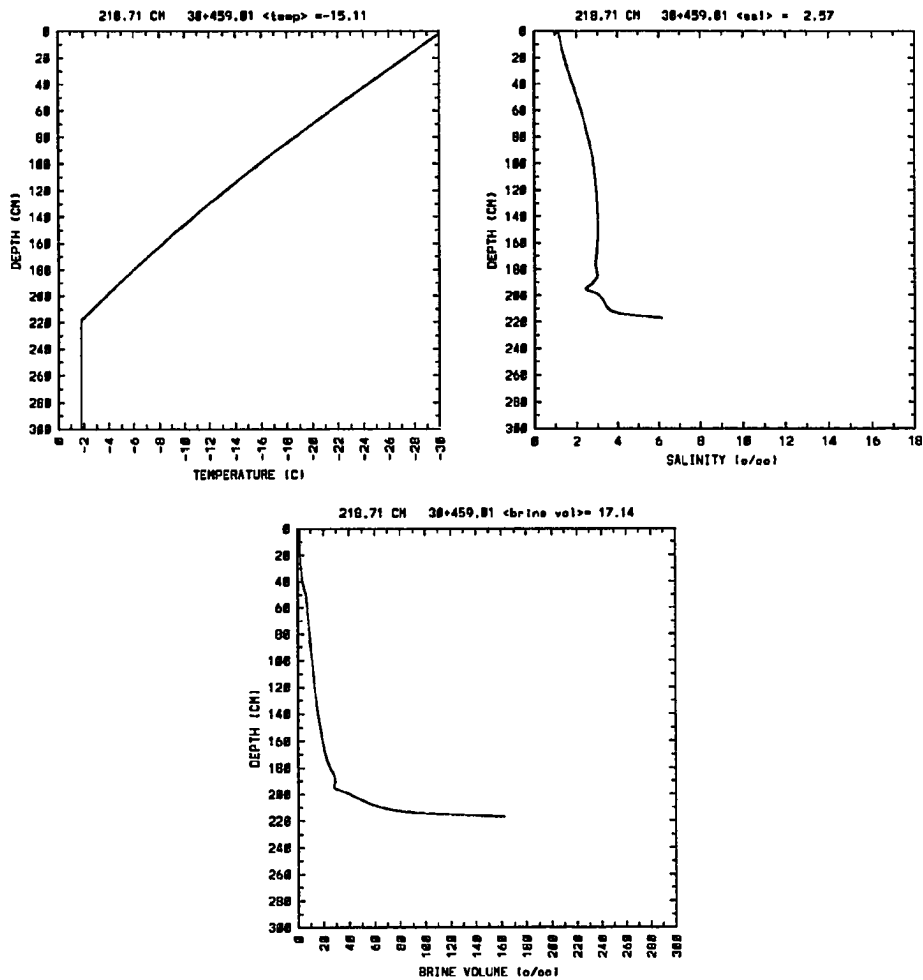


Fig. 15. Multiyear Ice on January 1 with Meltwater Desalination.

The following three figures (Figures 14,15 and 16) show the temperature, salinity and brine volume profiles for the multiyear simulations on 1 September, 1 January and 15 May, respectively.

Although the resulting multiyear profiles are encouraging, they do show significant deviations from reality. For instance, the upper portion of the ice sheet (above the sea level or freeboard) has not been desalinated to the degree that is commonly observed in nature (Schwazacher, 1959; Cox and Weeks, 1974) where this part of the multiyear

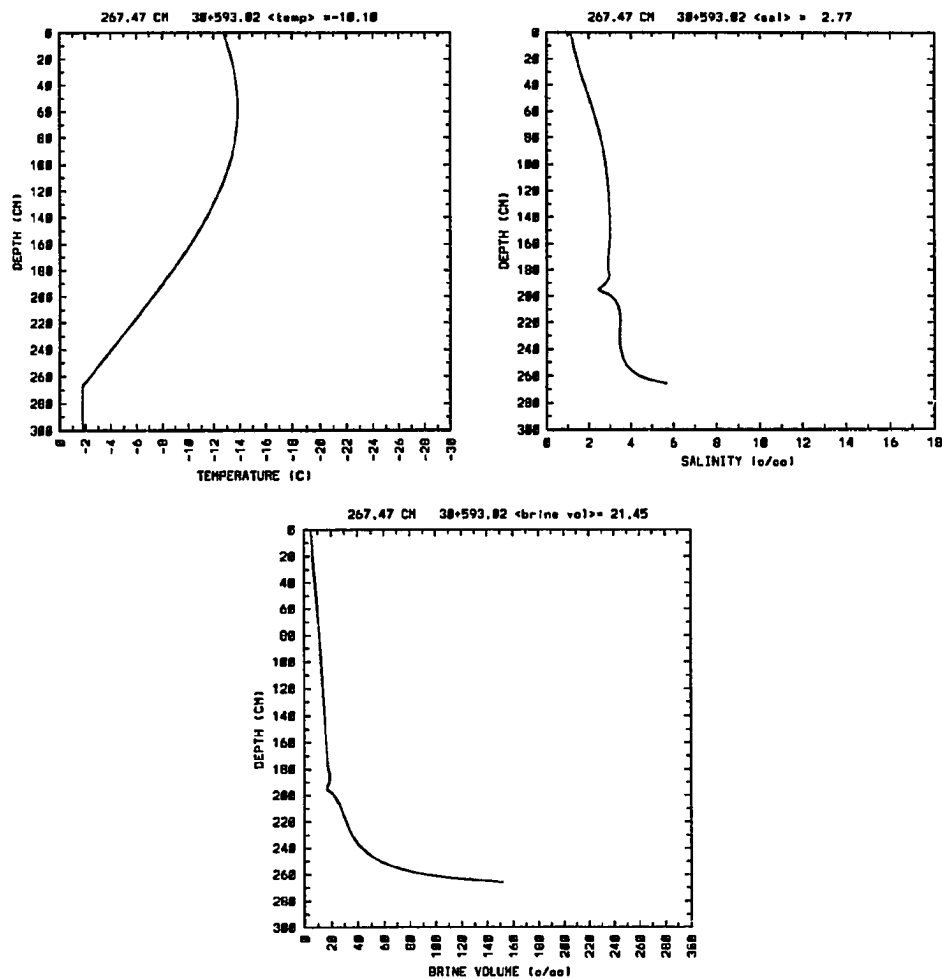


Fig. 16. Multiyear Ice on May 15 with Meltwater Desalination.

profile commonly shows values that are near 0 ppt . The salinities in the lower portion of the ice are, however, quite reasonable showing values roughly 5.5 ppt . The difference here again is that the present modeling does not attempt to adequately formulate the process of flushing. It is believed that the present results suggest that if a realistic parameterization of this process could be added to the current model then the resulting combination should be capable of simulating the complete ice growth, ice temperature, ice salinity and brine volume of an undeformed sea ice sheet from the formation of

the initial ice skim to the development of a Zubovian steady state floe. The flushing component of the model would presumably be activated by the initiation of surface melting in either the snow pack or the top level of the sea ice. The model would also have to include a consideration of the apparent fact that flushing works differently in the above-sea-level portion of the ice sheet than in the below-sea-level portion. In the above-sea-level portion the mechanism is presumably simple drainage while in the below-sea-level region the salinity is probably reduced by dilution into a diffusion limited environment (i.e. there is no convection as the lowest salinity brine is located in the upper part of the ice).

2.6 Model Comparisons

2.6.1 Introduction

There are several important differences between the current model and previous linear temperature profile models. The first difference is the use of a finite-difference routine to establish the freezing interface and to characterize each layer. The assumption of a linear temperature profile for the ice sheet is not an unreasonable assumption by itself in that the ice sheet generally has a temperature profile that closely resembles a straight line except during times of abrupt atmospheric temperature fluctuations. This is a point stressed by Maykut (1986) and clearly supported by the temperature profiles in Figures 8 and 9. Even during sudden changes in temperature, the ice responds within several days and returns to a linear profile fairly quickly. The problem arises, not from the linear temperature profile assumption, but from the assumption of a uniform thermal conductivity throughout the ice sheet. This difficulty is exacerbated when this uniform conductivity is assumed to be equivalent to that of the top layer as was assumed by Cox and Weeks (1988a).

The top of the ice sheet is generally the coldest part of the ice and, because the thermal conductivity is a strong function of brine volume and brine volume is a

strong function of temperature, the cold top layer has a high thermal conductivity (low temperature \implies low brine volume \implies high thermal conductivity). This high value when used for the bulk thermal conductivity of the ice sheet, produces high conductive heat fluxes and correspondingly high growth velocities. However, the factor limiting the ice growth velocity is the upward conduction of the latent heat of formation liberated at the phase change boundary. This heat must pass through the bottom layers and on up to the ice surface where it is released into the atmosphere. In reality, it is not the thermal conductivity of the top layer that restricts the conductive heat flux, but rather the lower thermal conductivities of the bottom layers where the ice is warm with high brine volume and a resulting low thermal conductivity.

The linear models generally assume a bulk thermal conductivity and fixed values for the latent heat of formation and heat capacitance even though these parameters are also functions of the brine volume and change significantly with temperature. In fact, during the ice growth season the bottom layers of the ice sheet are invariably warmer, resulting in higher brine volumes, higher heat capacitances, lower densities and lower latent heat of formation and lower thermal conductivities than in the upper portion of the ice sheet.

Also the linear models assume that the values of these parameters are linear with temperature, which they are not. Due to this assumption, the linear models have higher latent heat of formation, lower ice sheet heat capacitances, higher conductive heat fluxes, higher ice surface temperatures and higher growth velocities. In fact, as will be shown in the next section, a comparison of observed sea ice thickness as a function of freezing-degree-days for the linear model and the non-linear model shows that the linear model tends to grow too much ice by a factor of nearly two (see Figure 17). Cox and Weeks (1988) were aware of this general problem in the linear model, but not of its cause. They specifically noted that, when they attempted to use the more rigorous description of the latent heat of freezing developed by Ono (1967, 1975), unrealistically high growth rates and ice salinities were obtained. They also recommended that this

difficulty be studied in future investigations.

2.6.2 Ice Thickness

It is, of course, desirable to compare the results of the linear and non-linear models with observed data. Unfortunately this proved to be difficult as the result of a lack of field sites where simultaneous growth rate, meteorological data and salinity profiles are available. While there is ice thickness information available for a number of sites in the North American Arctic (Bilello, 1961), the specifics of the incoming radiation and meteorological data are invariably lacking as is any information on the salinity of the ice. Therefore it was decided to utilize several of the general freezing-degree-day equivalent formulas available in the literature as a test set. Figure 17 shows ice thickness plotted as a function of accumulated freezing-degree-days for the linear model, the current non-linear(1:3) model, the current non-linear(1:1) model and four empirical models discussed in Bilello (1961). The two different non-linear models represent different initialization and will be discussed later. A brief description of each of the empirical models follows.

The Lebedev equation (Figure 17) was derived from ice station measurements in the Kara, East Siberian, Chukhotsk, Barents and Laptev Seas taken over a 24 year period. The resulting equation was

$$h = 1.33 (\Sigma \theta)^{0.58} \quad (2.54)$$

where h = ice thickness in *cm* and $\Sigma \theta$ = accumulated degree days. The Graystone equation

$$h = 1.53 (\Sigma \theta)^{0.59} \quad (2.55)$$

was fitted to ice thickness data taken in Button Bay near Churchill, Manitoba. The data on which this curve was based are a bit "peculiar" in that the field site was near the mouth of a large river which accounts for the fact that more ice grew at this site for a given number of accumulated degree days than at any of the "normal" sea ice sites.

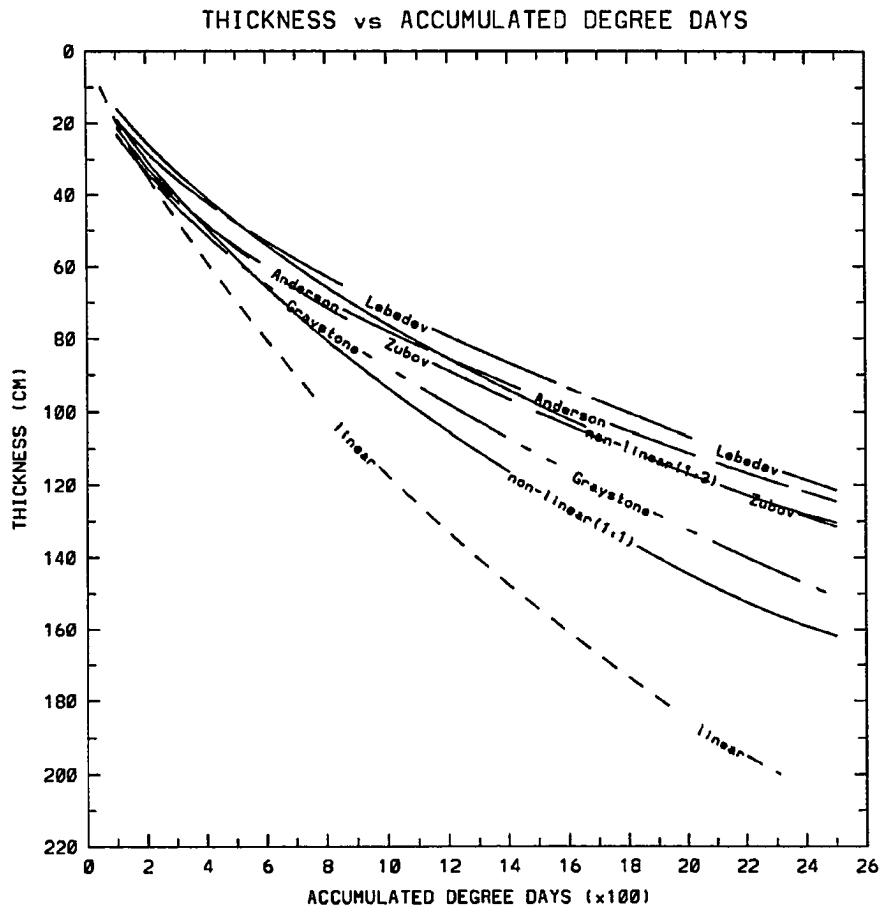


Fig. 17. Growth Rate Comparison.

Graystone and Langleben (1963) also reported that the ice showed salinities that were lower than normal sea ice. The Zubov equation

$$h^2 + 50h = 8 \Sigma \theta \quad (2.56)$$

was derived from ice station observations made in the Kara and Chukhotsk Seas. This relation also provides a reasonable fit to ice growth observations made at 5 stations (Alert, Eureka, Isachsen, Mould Bay and Resolute) in the Canadian Arctic as reported by Bilello (1961). The final equation is by Anderson (1961) which was fitted to thin ice

growth observations made at Tule, Greenland and is also identical in form to Zubov's relation in that it includes both h and h^2 terms.

$$h^2 + 5.1 h = 6.7 \Sigma \theta \quad (2.57)$$

A note on the growth rate seems in order here. While the current ice growth model attempts to incorporate as much physics as possible, there are still effects of certain tuning parameters that greatly influence the overall growth rate of the model. Perhaps the major tuning parameter for the growth rate is the initialization of the thermal properties of the fluid phase in the finite-difference program. Figure 17 also shows the effects of changing the thermal properties of the fluid phase. The line labeled non-linear(1:3) represents the ice growth for the model with the initial thermal properties of the fluid phase having the characteristics of ice-to-water at a ratio of 1:3. The non-linear(1:1) line shows the growth rate of the model with the initial thermal properties changed such that the properties were 50% water and 50% ice (i.e. conductivity = $3.18 \times 10^{-3} \text{ cal cm}^{-1} \text{ sec}^{-1} \text{ }^\circ\text{C}^{-1}$ and heat capacity = $0.729 \text{ cal cm}^{-3}$). This produces a higher thermal conductivity and lower heat capacitance than for the 1:3 ice/water combination (i.e. conductivity = $2.12 \times 10^{-3} \text{ cal cm}^{-1} \text{ sec}^{-1} \text{ }^\circ\text{C}^{-1}$ and heat capacity = $0.972 \text{ cal cm}^{-3}$) for the first plot.

The reason that this particular change in the program has such a large effect upon the overall growth rate is detailed as follows. In any finite-difference program there is an approximation made about the conditions between each spatial node. The space between the nodes is assumed to be of a uniform material (ice, water, etc.) and does not change until the freezing interface travels completely through to the new node at which time the material properties are updated. So, if the freezing interface is just past a node and we have initialized the space between this node and the next to have the thermal properties of water, we will be increasingly incorrect as the interface progresses downward through the layer. On the other hand, if we initialize the layer as having the thermal properties of ice, we will begin with an incorrect value and get increasingly more accurate as the

interface progresses through the layer. In both cases, the finite difference scheme is only truly correct when the interface is exactly at the node.

The important point to remember is that if we initialize the liquid phase with thermal properties of water, the thermal conductivity will be too low and the model will grow too little ice. However, if we initialize the liquid phase as having thermal properties of ice, the thermal conductivity will be too high and the model will grow too much ice. So the thermal properties of the liquid phase were chosen (i.e. $1/3$ ice and $2/3$ water) such that in the absence of snow the model would grow approximately the correct amount of ice according to the empirical formulas. This choice also appears reasonable when we realize that sea ice does not freeze at a planar interface. The bottom of sea ice contains a "lacy" skeletal layer that is mostly an interlayer mixture of ice and water.

It should be noted here that the choice of the liquid phase thermal properties of $1:3$ was driven by the fact that the simulations were run in the absence of a snow cover and this ratio produced ice thicknesses that approximated reality (i.e. the model was "tuned"). A simulation was run to determine the thermal properties required to grow the correct amount of ice in the presence of 20 cm of accumulated snow on the ice. This was done using snow fall option 8 of the program with 40% of the actual snowfall (51 cm) at Dease Inlet for the 1991–92 ice season and growing ice for the length of the ice growth season (200 days). The approximate first year ice thickness for this region was $170\text{--}175\text{ cm}$ (R. Glen personal communicate) and the ice growth model with $1:3$ ice to water ratio grew 176 cm . Changing the ice to water ratio to $1:1$ and allowing a total of 20 cm of snow to accumulate the ice growth model also produced ice of 176 cm . Thus the result of changing the ice to water ratio offset the thermal insulating effect of the snow.

2.6.3 Ice Properties

The validation of the salinity profiles encountered the same difficulties as the growth rate validation effort. While there are data available that, during one winter, characterize the salinity profiles for given sites such as Eclipse Sound (Nakawo and Sinha, 1981),

the incoming radiation and meteorological data were not readily available. The approach to validation of salinity and brine profiles was to utilize the linear temperature profile model of Cox and Weeks (1988a) . This linear model grows approximately two times the desired amount of ice, yet it produces salinity and brine profiles at any given thickness, that are near those observed.

While we have determined that the linear models tend to grow too much ice because their growth velocities are high, the question arises as to why then do these models give the correct salinity profiles? Since the initial salt entrapment is a function of the growth velocities, why do the linear models produce salinity profiles that are correct when their growth velocities are too high? It would seem that with high growth velocities, these models should produce salinity profiles that are too saline.

The current model utilizes a finite-difference routine to calculate the heat conduction through each layer and determines the position of the freezing interface. In addition, the program uses a non-linear latent heat of formation and the heat capacitance for each layer to calculate the heat conduction through that layer and ultimately the temperature. These factors, coupled with the fact that the conductive heat flux is determined by the thermal conductivity of the bottom layers and not the upper layers, reduce growth velocity and the initial salt entrapment. This reduced growth velocity produces roughly the correct amount of ice but the overall salinity of the ice sheet is below those typically encountered.

The solution to the problem of low salinities for the current model was found by observing that the linear model of Cox and Weeks calculates the brine expulsion and gravity drainage for each layer and simply removes this quantity of brine from the entire ice sheet. In reality the brine from one layer must migrate to one of the layers above or below and can only leave the ice sheet through the top or bottom layer. In the current model the excess brine from layer to layer moves within the ice sheet and largely escape through the bottom layer.

This is also the reason the earlier models produced the correct salinity profiles while

growing about twice as much ice as normally seen. The growth velocities were high, producing high initial salt entrapment, while the brine expulsion and gravity drainage were correct for each layer but overestimated for the ice sheet as a whole. Thus, the combination of entrapping too much salt and over desalinization of the ice sheet produced correct salinity profiles proving that two negatives make a positive.

The current model generally produces lower growth velocities and therefore, the initial salt entrapments are lower than the linear model. The process of placing the brine from one layer back into the next layer (i.e. conserving brine) and allowing the brine to escape only through the bottom layer, keeps the overall salinities within realistic values.

Chapter 3 Synthetic Aperture Radar

3.1 Introduction

The scale, remoteness and frequently inhospitable nature of the polar regions make them difficult areas to study. The considerable expense involved with mounting polar expeditions, the long periods of darkness and the extremely low temperatures during the winter plus the large variations in climate and terrain all contribute to these problems. Conversely these factors also appear to make the polar regions an ideal place to apply remote sensing procedures. In many senses this is true. Unfortunately, remote sensing procedures also have their limitations when applied in these regions.

Ideally, remote sensing of the polar regions would utilize systems that operate at either visible or infrared frequencies. There are several reasons for this. First, both visible and infrared sensors result in imagery that is of sufficiently high resolution to resolve almost all sea ice features of interest. Second, visible sensors produce images that are similar to what one sees. As such they provide information that we “think” we understand, or at least are comfortable with. Although infrared images are quite different from what one sees, there are compensations in that IR delineates open water and thin ice area “hot spots” very clearly, which is information that is of considerable use. Unfortunately, visible and IR remote sensing in the polar regions is confronted with two primary problems: the long periods of darkness during the winter months and the common occurrence of fog and clouds during the summer months. These two factors make visible and infrared sensors impractical for long-term monitoring in that they are limited by both clouds and darkness respectively, making it impossible to obtain data on demand.

This problem does not affect imagery collected by microwave systems since these function independent of clouds and darkness, providing a practical opportunity to monitor the polar regions with consistent coverage. However, to date the passive microwave

systems that have been deployed on satellites are only capable of coarse resolutions (>10 km) which do not resolve most sea ice features of interest. Also the interpretation of the resulting data is far from simple (see the discussions in Carsey, 1992).

The advent of satellite-borne synthetic aperture radar (SAR) has given the polar researcher a much needed tool for remote sensing since such radar systems both penetrate darkness, clouds and fog as well as provide adequate resolution to identify specific sea ice features. This is not to suggest that the use of active microwave techniques is simpler than using passive ones, only that individual small scale features can be identified in most SAR images which is of considerable assistance in image interpretation.

SAR systems achieve their high resolution by sequentially using a large number of low resolution returns obtained by a small antenna to numerically synthesize the equivalent of a high resolution return as obtained from a very large antenna. For the ERS-1 satellite this is done by using the satellite's speed of roughly 8 km/sec and the phase information of the radar to computationally create the equivalent of a large antenna.

As the SAR satellite moves over the Earth's surface, it transmits and receives a radar pulse every few meters. In the case of the ERS-1 satellite, this distance is every 4 meters. Therefore data will be collected from 1000 returns as the satellite travels 4 kilometers. In that the satellite is travelling at roughly 8 kilometers per second and has no on-board storage or data compression capability the data have to be transmitted to ground stations such as the Alaskan SAR Facility at very large data transmission rates between the satellite and the ground (105 Mbits/s). At the ground station these data are digitally processed to form an image by using 1000 returns to synthesize the high resolution return at each point. It is the 4 kilometers the satellite traveled during these 1000 returns that is important since this distance represents the size of the synthetic high resolution aperture (Ulaby et al. 1982).

There are several points that the radar observer must keep in mind while viewing radar imagery. Since the radar uses a different wavelength than visible light, the

interaction of the radiation with the material that it impinges upon is very different than that of visible light. Electromagnetic radiation that impinges on a medium from above will divide its energy between a backward scattering component and a forward transmitted component that will penetrate the lower medium. If the lower medium is homogeneous and semi-infinite, the surface backscattering component is the only contributor and the problem is one of surface scattering. However, if the lower medium contains inhomogeneities, there will be a contribution due to volume scattering from these discontinuities. Surface scattering is characterized by the difference in dielectric constants between the two media and the surface "roughness". In general, for a given surface, the greater the difference in dielectric constants between the two media the greater the surface scattering. If the difference in dielectric constants is small, there will be very little surface scattering from the interface.

The apparent roughness of a surface is dependent on the frequency of the radiation and a surface that appears rough to visible light may appear "smooth" for radar frequencies. Two parameters that define the roughness of a surface are the standard deviation of the surface height variation (or rms height) and the surface correlation length. In other words, the "roughness" of a surface depends upon the height of the deviations and the distance between them relative to the wavelength of the radiation. This means that more surfaces will appear "rough" to a C-band radar than an L-band radar because the C-band radar has a smaller wavelength than the L-band. However, the L-band radar will penetrate deeper into most materials than the C-band and therefore volume scattering may become a bigger factor in determining the radar backscatter.

The C-band SAR on the ERS-1 satellite is a active microwave radar operating at a wavelength (λ) of 5.6 cm with vertical transmit and receive polarization (VV). The microwave signature is the result of the two basic scattering mechanisms, surface and volume scattering. For surface scattering: a) the scattering strength is proportional to the relative complex dielectric constant of the surface and b) its angular scattering pattern

is governed by the surface roughness. For volume scattering: a) the scattering strength is proportional to the dielectric discontinuities inside the medium and the density of the inhomogeneities and b) its angular scattering pattern is determined by the roughness of the boundary surface, the average dielectric constant of the medium and the geometric size of the inhomogeneities relative to the incoming wavelength.

For a radar with the antenna serving as both the transmit and receive antennae, the basic radar equation may be written as (Ulaby et al. 1986)

$$\overline{P_r} = \frac{\lambda^2}{(4\pi)^3} \int_{area} \frac{P_t G_t G_r \sigma^0 dA}{R^4} \quad (3.1)$$

where $P_t(\theta, \phi)$ defines the incident direction of the transmitted power at polarization t , R is the range distance to the target, G_t and G_r are the transmitter and the receiver gain, λ is the radar wavelength, A is the area and σ^0 is the scattering coefficient of the target scattering behavior for a given frequency and incident angle. The scattering coefficient is a measure of the medium's reaction to radar frequency radiation and is independent of the transmitted power, the gain of the receiver, the range and the area of illumination. It is a function of the scattering medium (and the roughness of its surface) and may be broken into surface scattering and volume scattering components. The digital number (DN) obtained is a measure of the received radar intensity and includes the system noise, the range effects, the effects of the area of illumination, and any gain variations in receiving and during processing. Thus, a correction to σ^0 is usually made to eliminate these factors and allow comparisons between images.

One method to determine the relative contribution of surface scattering and volume scattering is to calculate the depth of penetration of the radar pulse. The depth of penetration is a measure of the "active layer" of the medium which is sea ice in our case and is the depth to which the radiation may penetrate and still give a signal return that is discernible. The depth of penetration ($\delta_p = 1/(2\alpha)$) is defined as the depth at which the power falls to $1/e$ of the power at the surface of the medium. The field

attenuation coefficient α is generally defined as

$$\alpha = \frac{2\pi}{\lambda_0} [\text{Im} (\sqrt{\epsilon})] \quad (3.2)$$

where $\epsilon = \epsilon_1 - i\epsilon_2$ is the relative dielectric constant and $\lambda_0 = 5.6$ cm is the radar wavelength of the ERS-1 SAR. The imaginary part of the complex dielectric constant ($\sqrt{\epsilon}$) is equal to

$$\text{Im} (\sqrt{\epsilon}) = (\epsilon_1^2 + \epsilon_2^2)^{\frac{1}{4}} \times \left\{ \sin \left[\frac{\tan^{-1} \left(\frac{\epsilon_2}{\epsilon_1} \right)}{2} \right] \right\} \quad (3.3)$$

The primary parameter for influencing the dielectric constant in sea ice is the brine volume (Vant et al. 1978). An expression for the relative dielectric constant (for the 5.3 Ghz C-Band radar) as a function of brine volume (V_b) may be calculated utilizing the equations by Kim (1984) and Vant (1978)

$$\epsilon_1 = (0.995 - 0.00154 \times (5.3)) \epsilon'_1 \quad (3.4)$$

$$\epsilon_2 = (0.914 - 0.00546 \times (5.3)) \epsilon'_2 \quad (3.5)$$

where the brine volume dependence of the coefficients is

$$\epsilon'_1 = 3.05 + 7.20 V_b \quad (3.6)$$

$$\epsilon'_2 = 0.024 + 3.29 V_b \quad (3.7)$$

Once the penetration depth has been established, the relative magnitudes of the two scattering mechanisms (surface and volume) becomes evident. A rough approximation of the relative dielectric constant for the ice was made by assuming the brine volume of the top layer was representative of the entire ice sheet and the depth of penetration

was calculated using the above equations. While it is true that the brine volume of the top layer was generally lower than anywhere else in the ice, this gives an estimate of the theoretical maximum depth of penetration and is therefore a maximum measure of the thickness of the "active layer". In that, this layer represents the majority of the ice-radar interactions; its properties will determine the intensity of the radar backscattering signature received by the antenna.

3.2 Surface Scattering

The C-band backscatter coefficient for sea ice is generally a strong function of the surface scattering coefficient. The primary reason for this is that most sea ice surfaces appear "rough" to the small wavelength of the C-band radar. The two surface parameters that characterize the ice surface are the standard deviation of surface height (σ) and the surface correlation height (l). The standard deviation of surface height is

$$\sigma = \left(\overline{z^2} - \bar{z}^2 \right)^{1/2} \quad (3.8)$$

where

$$\bar{z} = \frac{1}{L_x L_y} \int_{-\frac{L_x}{2}}^{\frac{L_x}{2}} \int_{-\frac{L_y}{2}}^{\frac{L_y}{2}} z(x, y) dx dy \quad (3.9)$$

and

$$\overline{z^2} = \frac{1}{L_x L_y} \int_{-\frac{L_x}{2}}^{\frac{L_x}{2}} \int_{-\frac{L_y}{2}}^{\frac{L_y}{2}} z^2(x, y) dx dy \quad (3.10)$$

The surface correlation length is defined as the displacement l' for which

$$\rho(l) = \frac{1}{e} \quad (3.11)$$

where

$$\rho(\hat{x}) = \frac{\int_{-\frac{L_x}{2}}^{\frac{L_x}{2}} z(x) z(x + \hat{x}) dx}{\int_{-\frac{L_x}{2}}^{\frac{L_x}{2}} z^2(x) dx} \quad (3.12)$$

is the one-dimensional autocorrelation function for a surface $z(x)$ where the autocorrelation function is a measure of the similarity between the points x and x' .

There are many different criteria for the "smoothness" or "roughness" of a surface, some are more stringent than others. One measure of the surface is given by the Rayleigh criterion and another is the phase dependent Fraunhofer criterion. The Rayleigh criterion defines a "smooth" surface as one that has a standard deviation less than

$$\sigma < \frac{\lambda}{8 \cos(\theta)} \quad (3.13)$$

where θ is the incidence angle and λ is the radar wavelength. For the C-band SAR of ERS-1 the incidence angle is $\theta = 23^\circ$ and the wavelength is $\lambda = 5.6 \text{ cm}$. This means that a surface with a standard deviation less than $\sigma = 0.76 \text{ cm}$ or less will be considered "smooth" by the Rayleigh criterion.

For a surface to be considered "rough", the Rayleigh criterion is such that the standard deviation must be greater than

$$\sigma < \frac{\lambda}{4.4 \cos(\theta)} \quad (3.14)$$

which for the ERS-1 SAR translates to a standard deviation greater than $\sigma = 1.38 \text{ cm}$. This means that the height difference in the standard deviation between a smooth and a rough surface is less than 0.7 cm according to the Rayleigh criterion.

The Fraunhofer criterion is an even more restrained criterion in that it requires the maximum phase difference between incoming rays to be less than $\pi/8$ radians. For a smooth surface, this leads to a standard deviation for the surface height of

$$\sigma < \frac{\lambda}{32 \cos(\theta)} \quad (3.15)$$

Therefore for a C-band radar a "smooth" surface would have a surface standard deviation $\sigma = 0.19 \text{ cm}$ or less. These values for smoothness criteria demonstrate why most surfaces appear "rough" to a C-band radar.

The backscattering coefficient for a "slightly rough" surface, where both the surface standard deviation and the correlation length are smaller than the radar wavelength (Ulaby et al 1986) may be represented by the equation

$$\sigma_s^0 = 8k^4 \sigma^2 \cos^4 \theta |R(\theta)|^2 W(2k \sin \theta, 0) \quad (3.16)$$

where σ is the standard deviation of the surface roughness, $W(2k \sin \theta, 0)$ is the Fourier transform of the surface correlation coefficient or the normalized roughness spectrum, and $|R(\theta)|^2$ is the complex Fresnel reflection coefficient. For a surface with an isotropic roughness spectrum or Gaussian correlation coefficient with correlation length l and wave number $k = 2\pi / \lambda$ this equation may be rewritten as

$$W(2k \sin \theta, 0) = \frac{l^2}{2} \exp \left[-(kl \sin \theta)^2 \right] \quad (3.17)$$

The Fresnel reflection coefficient is given by

$$|R(\theta_r)|^2 = \frac{\left[\cos \theta_r - \sqrt{r} \cos \left(\frac{\theta}{2} \right) \right]^2 + r \sin^2 \left(\frac{\theta}{2} \right)}{\left[\cos \theta_r + \sqrt{r} \cos \left(\frac{\theta}{2} \right) \right]^2 + r \sin^2 \left(\frac{\theta}{2} \right)} \quad (3.18)$$

where

$$\theta = \tan^{-1} \left[\frac{\epsilon_2}{\epsilon_1 - \sin^2 \theta_r} \right] \quad (3.19)$$

$$r = \left\{ [\epsilon_1 - \sin^2 \theta_r]^2 + \epsilon_2 \right\}^{\frac{1}{2}} \quad (3.20)$$

and θ_r is the angle of incidence and ϵ_1 and ϵ_2 are the real and imaginary part of the complex dielectric constant.

Inserting these expressions into the equation for the surface backscattering coefficient leads to

$$\sigma_s^0 = 8k^4 \sigma^2 \cos^4 \theta |R(\theta)|^2 \frac{l^2}{2} \exp \left[-(kl \sin \theta)^2 \right] \quad (3.21)$$

For a given surface with standard deviation σ and correlation length l , the only parameter in this equation that is independent of the surface characteristics is the complex Fresnel reflection coefficient. Therefore for a given surface, this equation may be rewritten as

$$\sigma_s^0 = C |R(\theta)|^2 \quad (3.22)$$

where C is a constant whose value depends upon the surface characteristics and the incidence angle and may be determined for each radar image.

3.3 Volume Scattering

In general, most natural media contain numerous dielectric inhomogeneities. If the medium has some transparency to the radiation wavelength, these dielectric discontinuities will cause volume scattering. The magnitude of the volume scattering will be established by two factors: 1) the effective depth of penetration and 2) the difference in dielectric constant between the media and the inhomogeneities.

The second term in a radar return is the volume backscattering coefficient which may be represented by the following equation.

$$\sigma_v^0(\theta) = \frac{N \sigma_b \cos(\theta)}{2 \kappa_e} \left[1 - \frac{1}{L^2(\theta)} \right] \quad (3.23)$$

In this expression N is the number of scatterers per unit volume (all assumed to be identical), σ_b is the backscattering cross-section of one scatterer, κ_e is the extinction coefficient of the scattering layer, and $L^2(\theta)$ is the two way loss factor indicative of the medium. The loss factor may be represented by

$$L^2(\theta) = [\exp (\kappa_e d \sec \theta)]^2 \quad (3.24)$$

where d is the round trip distance in the medium, κ_e is the extinction coefficient and θ is the incidence angle.

In general, the volume scattering term for first year sea ice is relatively small when compared to the surface scattering term. For multiyear ice, the volume term is no longer insignificant, however, the dominant scattering occurs at the air inclusions rather than the brine pockets. At least during the winter, these air bubbles would not be expected to vary appreciably with time nor temperature and the volume scattering term tends to remain stable. It is for these reasons that the volume scattering term may be replaced by a constant which depends upon whether the model characterizes first year or multiyear sea ice. Therefore the equation for the volume backscattering coefficient becomes

$$\sigma_v^0(\theta) = D \quad (3.25)$$

where D is different for first year and multiyear ice.

There is a one word of caution required for this treatment that relates to the incidence angle dependence of the volume scattering. This dependence may or may not be a significant influence on the backscattering signature of the ice. It is a function of the relative contribution of the volume scattering term to the overall return and its effect will vary depending upon its magnitude. For example, if the volume scattering term has a large contribution relative to the overall return the incident angle dependence for volume scattering will be significant. However, if the volume scattering contribution is small then the incidence angle dependence will also be small. The incidence angle dependencies, whether they be volume or surface, are characteristics of the scattering medium and are not removed during image calibration which only removes instrument system dependencies.

3.4 Sea Ice Backscattering Model

Neglecting any surface and volume interactions, the scattering coefficient may be broken down into its surface scattering and volume scattering components and treated as a combination of these two effects. For sea ice, the total radar backscattering coefficient

may be represented by the following equation

$$\sigma^0 = \sigma_s^0 + Y^2(\theta) \left[\sigma_v^0 + \frac{\sigma_i^0(\theta')}{L^2(\theta')} \right] \quad (3.26)$$

where σ_s^0 is the backscattering coefficient due to the surface scattering, $Y^2(\theta)$ is the two way power transmissivity, σ_v^0 is the volume scattering, σ_i^0 is the backscatter from the ice-water interface, and $L^2(\theta')$ is the two way loss factor and is equal to

$$L^2(\theta') = \exp \left(\kappa_e d \frac{1}{\cos \theta} \right) \quad (3.27)$$

where d is the layer thickness, θ is the incidence angle and κ_e is the extinction coefficient.

As the freezing interface of sea ice is a dendritic structure with a negligible scattering coefficient, the interface scattering term of the backscattering coefficient for sea ice may be neglected and equation 3.26 may be written as

$$\sigma^0 = \sigma_s^0 + Y^2(\theta) \sigma_v^0 \quad (3.28)$$

Here the two-way transmissivity ($Y^2(\theta)$) is equal to

$$Y^2(\theta) = \exp \left(-\frac{2\tau}{\cos \theta} \right) \quad (3.29)$$

where τ is referred to as the "optical thickness" and is defined by

$$\tau(r_1, r_2) = \int_{r_1}^{r_2} \kappa_e dr \quad (3.30)$$

Here κ_e is the extinction coefficient or power attenuation coefficient.

Substituting the expressions for the surface scattering term and the volume scattering term into the total radar backscattering equation for sea ice above, leads to the equation

$$\sigma^0(\theta) = 8 k^4 \sigma^2 \cos^4 \theta \times |R(\theta)|^2 \times \frac{l^2}{2} \exp [-(k l \sin \theta)^2] + \frac{N \sigma_b \cos(\theta)}{2 \kappa_e} \left\{ 1 - \frac{1}{\left[\exp \left(\frac{\kappa_e d}{\cos \theta} \right) \right]^2} \right\} \quad (3.31)$$

Table 2. Model Constants.

ICE TYPE	C VALUE (dB)	D VALUE (dB)
FIRST YEAR ICE	188.9	-35.0
MULTIYEAR ICE	188.9	-29.0

where the first term is the surface scattering contribution and the second is that due to volume scattering. Making the assumptions about each term as in the previous sections the equation becomes

$$\sigma^0 = C |R(\theta)|^2 + D \quad (3.32)$$

The form of equation 3.31 using assumptions based on work by Kim, et al. (1985) was first formulated by Soulis et al. (1989).

The theoretical sea ice backscattering model uses the output of the ice physical properties from the ice growth model to determine the penetration depth as outlined in the section 3.1. It then determines the average ice properties for a layer whose thickness is equal to the penetration depth and uses these characteristics to calculate the predicted backscattering coefficient using the following values.

The values in the previous table were established from ERS-1 SAR measurements of first year ice in the Dease Inlet area near Point Barrow, Alaska. First, images from 4 September 1991 to 7 June 1992 were radiometrically corrected according to the procedure outlined in Appendix A and backscattering values were noted from a representative area of first year ice. Next, the mean and variance of these measurements were calculated and compared to the mean and variance of the predicted Fresnel coefficients. Then, the values for the constants C and D were adjusted in order to scale and translate the predicted values to match the range and mean of the measured values. The resulting values are shown in Table 2.

3.5 Incident Angle Dependence

The ERS-1 SAR has a look angle of 23° at the center of the image. In reality, the look angle (or incident angle) ranges from 20° at the near range to 26° at the far range. Although the range dependency of the antenna may be taken out of the image by making the corrections for σ_o as outlined in Appendix A, there remains an incident angle dependency that is a function of the backscattering medium. To better understand this effect we need to look at the backscattering model.

In the current model for the radar backscattering coefficient, the signature is a function of the Fresnel coefficient which, in turn, has a look angle dependence in the form of $\cos \theta_r$. The strength of this dependency is a function of the dielectric constant and will vary with brine volume. Figure 18 shows the theoretical backscatter as a function of look angle for brine volumes of 20, 60, 100, 140, 180, 220, 260 and 300 ppt with the highest returns from the highest brine volumes.

3.6 SAR Model Results

3.6.1 First Year Backscatter Values

To determine the usefulness of this technique, it was important to obtain, over a nearly complete ice growth season, SAR images of sea ice whose thicknesses were fairly well known, from an area where meteorological conditions were measured during the greater portion of the ice growth season. The Dease Inlet area east of Point Barrow Alaska (Figure 19) seemed like a reasonable candidate in that the barrier islands just north of the inlet trapped the ice, allowing the thermal history to be documented while the meteorological station at Barrow (approximately 50 km to the west) collected the required meteorological data. While the exact thickness of the ice growing in the Dease Inlet was not known, a reasonable estimate can be obtained from the ice growth model and from past field experience in this region

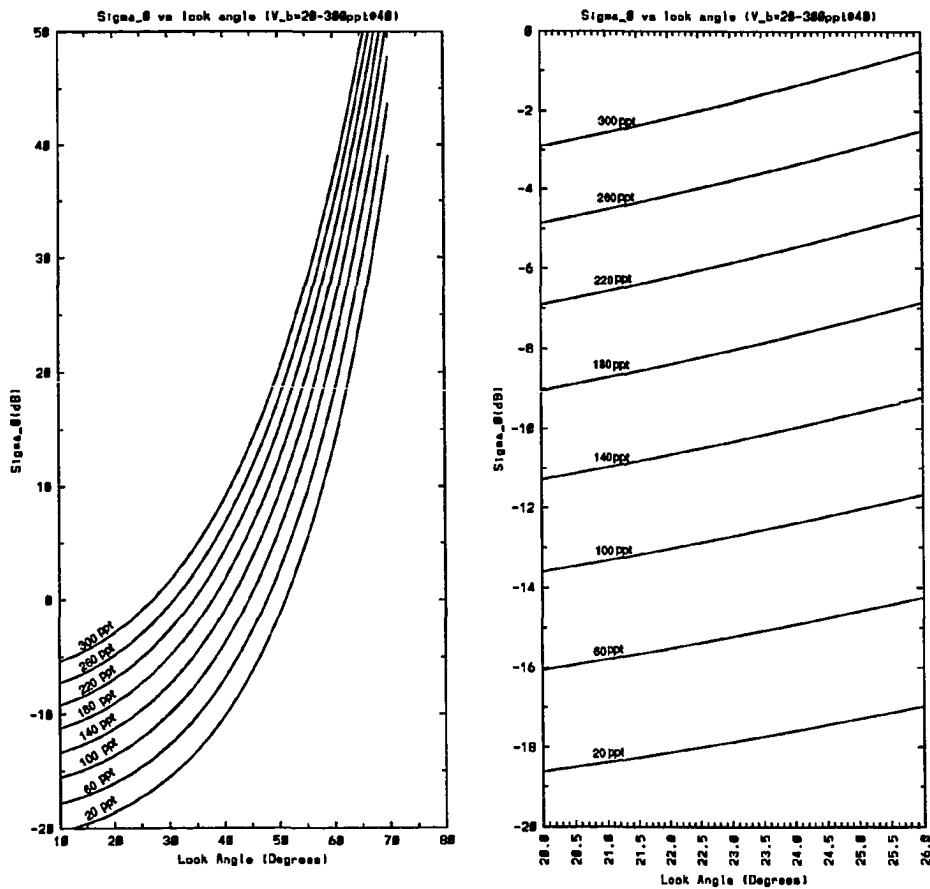


Fig. 18. Look Angle Dependence.

Figure 20 shows the relevant radar characteristics of the growing sea ice at Dease Inlet from 10 October 1991 to 28 April 1992. The physical properties of this ice sheet on 8 May 1992 may be seen in figure 6 in chapter 2. The values of the penetration depth, brine volume and temperature are those of the "active layer" as described earlier and represent the value for any given day. It should be noted that the backscatter values (σ^0) are plotted against theoretical thickness rather than days of growth. Because there was no melting, each day has associated with it a unique theoretical thickness associated with it.

ERS-1 SAR images were obtained for the Dease Inlet/Point Barrow area covering

the time period mentioned above, except for a period during December 1991 when the satellite orbit was altered. These images were corrected radiometrically as described in Appendix A and average backscattering values were taken from two areas highlighted by a square and an oval in Figure 19. This image was taken 17 January 1992 and shows the area of measurements for Dease Inlet profile 1 as a square and the area for Dease Inlet profile 2 as an oval. A comparison with the measured values from this area with the predicated values generated by the model is shown in figure 21.

The gap in measurement data between *80 cm* and *100 cm* is due to a change in the orbit of the satellite from the Commissioning Phase to the Ice Phase. The upward trend in the curves that occurs around *150 cm* is a result of the warming trend of the ice. The mismatch beginning at this point may be due to many things that are not taken into account in this model such as brine salinity changes, the presence of liquid water in the snow cover and surface roughness changes.

The agreement between the calculated and observed backscatter is surprisingly good considering that other factors may also influence radar returns. The general trend of the backscatter is a slowly decreasing function of time with the effects of short-term temperature fluctuations superimposed. The slope of this decrease depends strongly upon the date of formation of the ice; for instance ice that forms in the fall shows a more pronounced decrease in σ^o with time than ice that forms during the colder periods. The general decrease in backscatter is believed to be the combined result of a general decrease in the salinity of the upper portion of the ice with time and a simultaneous cooling of the penetration layer; both effects leading to a decrease in the complex dielectric constant. Removing the temperature fluctuations from the return and correlating the resulting signal with ice growth suggests that σ^o may be used to estimate ice thickness throughout much of the ice growth season.

If the predicted values are representative, this technique provides a means of estimating the approximate thickness of sea ice from the backscattering values of SAR

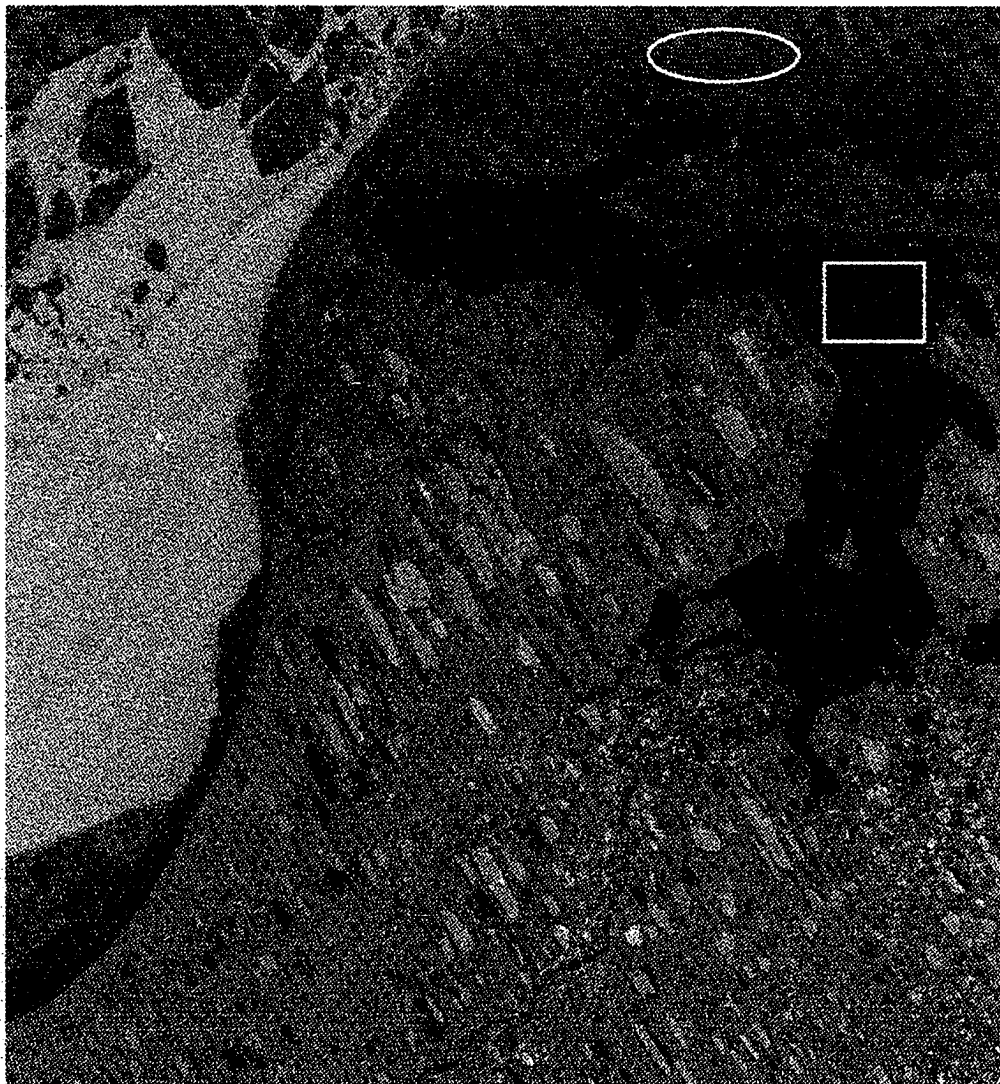


Fig. 19. Measurement Areas Near Point Barrow, Alaska, showing the two areas analyzed.

images. As stated earlier the general downward trend of the backscattering values is believed to be a combination of cooling and desalinization of the ice. As the ice gets colder, the brine volume decreases, the dielectric constant goes down and the backscatter drops. It appears that SAR indirectly senses the thermal state of the ice through the sensitivity of the brine volume to temperature change. If this is true, there should be

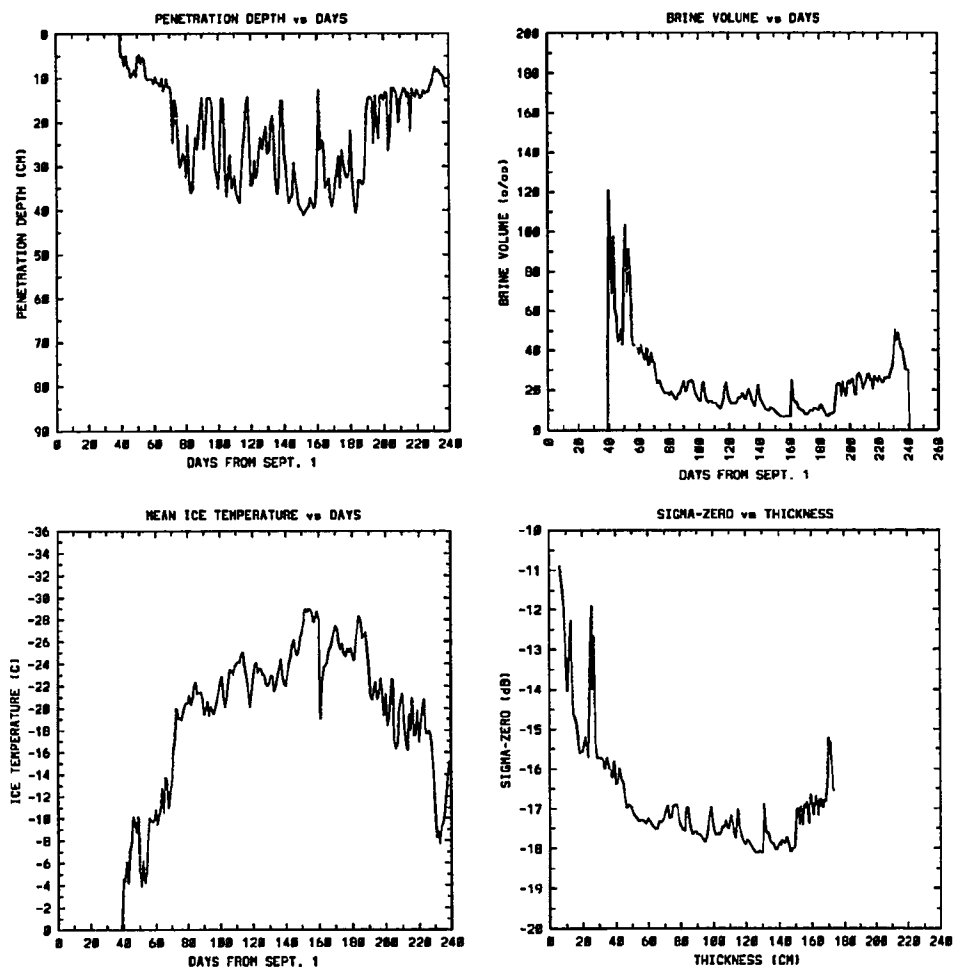


Fig. 20. Dease Inlet Profile 1.

a thickness signal imbedded within the backscattering plot which is due to the lower mean temperatures and brine volumes of thicker ice.

This may be more easily visualized by considering the conducted heat flux through both thick ice and thin ice. If the ocean and atmosphere are at different temperatures, then there exists some temperature gradient between them. The amount of heat that is conducted along this gradient is a function of the thermal conductivity and the thickness of the ice. For instance, for similar thermal conductivities, thick ice conducts less heat

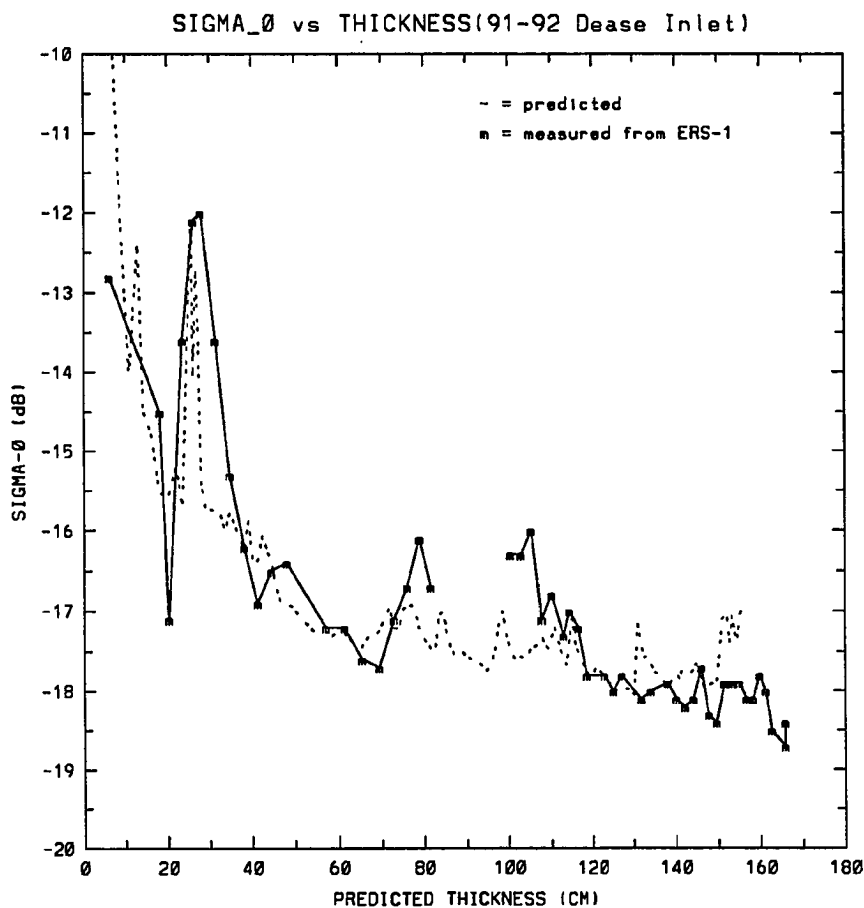


Fig. 21. Predicted vs Measured Backscatter for Dease Inlet 1.

than does thin ice which effects the temperature of the ice which changes the brine volume and the dielectric constant and ultimately the radar backscatter.

Figure 22 shows the predicted backscatter σ^0 as a function of the number of days since the first of September for ice of different thicknesses. This simulation was run using constant inputs for the air temperature ($T_{air} = -15^{\circ}C$), wind speed ($u_{wind} = 5$ m/sec) and snow (0 snow fall). Under these conditions ice that began growing earlier will always be thicker than ice that started growing later. Each line represents a 40 day

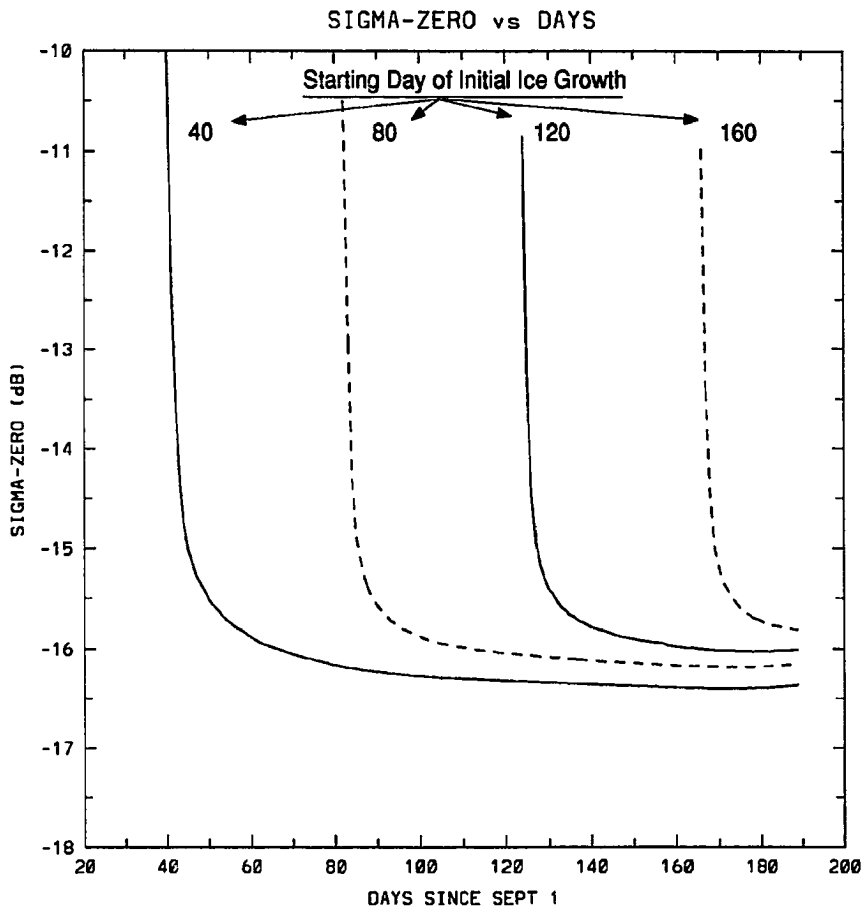


Fig. 22. Backscatter vs days for ice with initial growth starting on various days – Ideal.

delay in growth and therefore a decrease in thickness. The key point in this simulation is the fact that the thicker ice always has a lower backscattering value than the thinner ice.

While figure 22 shows much promise, in reality the situation is much more complicated as may be seen in figure 23. In this figure the actual meteorological data are used resulting in a rather confusing plot. However on close examination it can be seen that even here the thicker ice commonly shows a lower backscattering value than the thinner ice. Both the thick and thin first year ice respond to the atmospheric

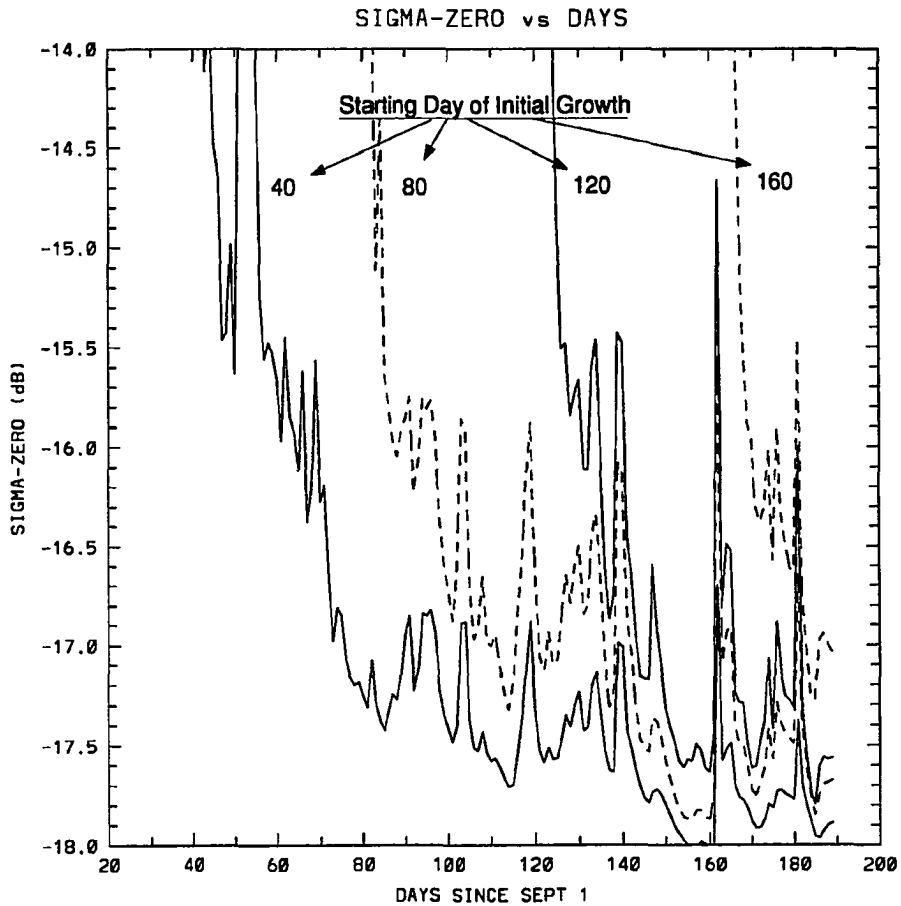


Fig. 23. Backscatter vs days for ice with initial growth starting on various days – Reality.

temperature fluctuations in similar ways with the thinner ice amplifying the upward trends more than the thick ice.

The basic idea behind using this technique to estimate ice thickness is as follows. A SAR image for a given date would be obtained and the backscatter value measured for the ice of interest. The backscattering value of the ice could be compared to the values in figure 23 for that date and an estimate of the beginning date of growth would be established.

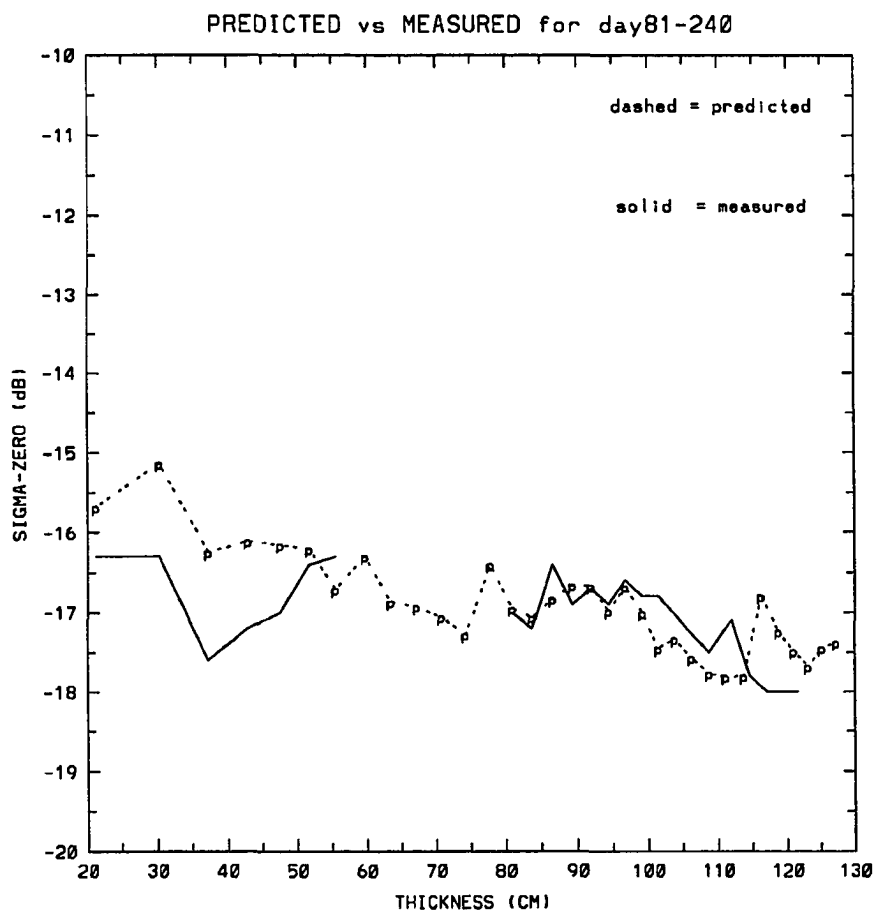


Fig. 24. Predicted vs Measured Backscatter for Dease Inlet 2.

A second comparison between measured and predicted values was performed on a lead that opened just north of Point Barrow some time between 18 November and 21 November 1991 (there exists an uncertainty of up to 3 days due to the 3 day repeat cycle of the satellite). Backscatter measurements were taken of this lead from 21 November 1991 to 17 February 1992 when the ice was swept away. The results are seen in figure 24. The area of these measurements is shown as the oval in the top of the image of figure 19. It should be noted that the results of the predicted backscatter are very sensitive to the date of opening and the time of the first observation of the lead. If the

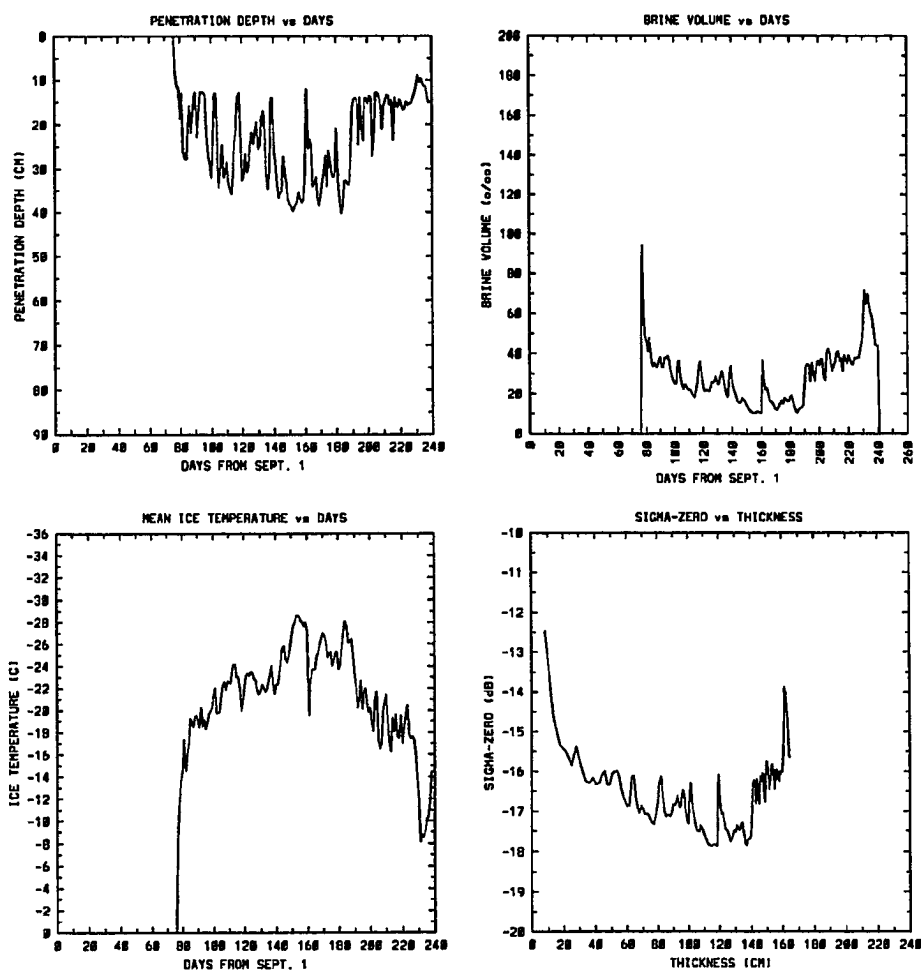


Fig. 25. Dease Inlet Profile 2.

lead opened on 18 November, just after the satellite passed over, by 21 November (the first observation of the lead) the ice would have grown over 20 cm in thickness and the mean ice temperature would have been much colder and the backscatter lower than if the lead had opened on the 20 of November only 1 day before the first observation.

It is the initial cooling of the ice and subsequent reduction of brine volume that produces the large drop in backscatter that may be seen in the σ^0 vs thickness plot of figure 25 (the lower right hand figure). The ice temperature by way of the brine

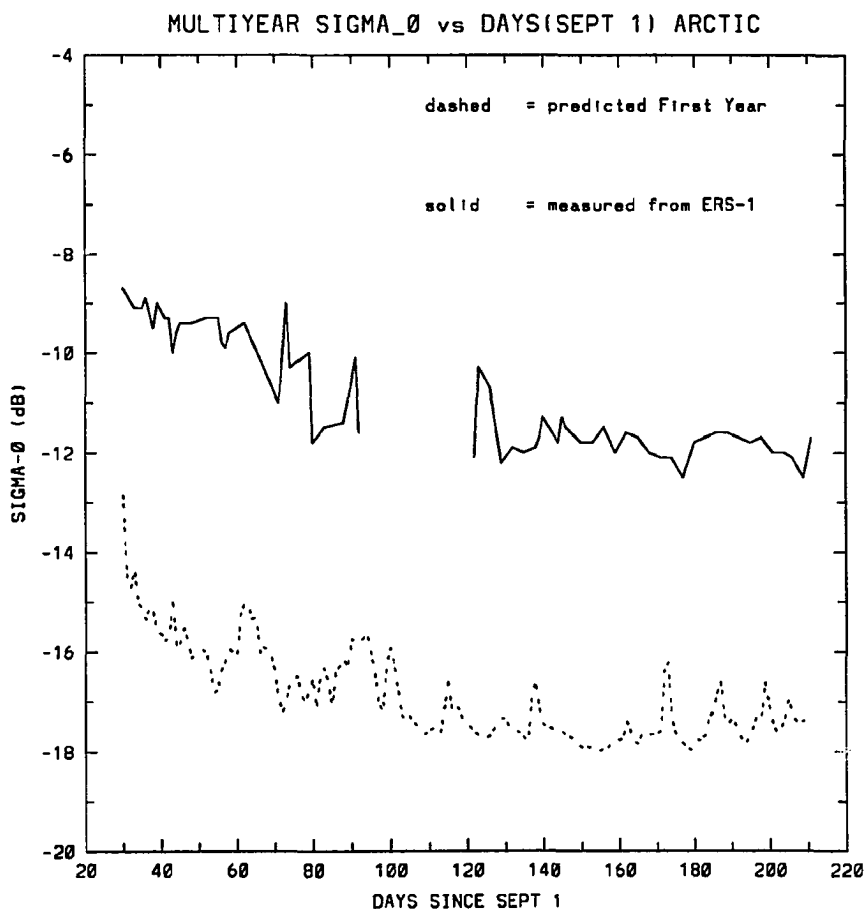


Fig. 26. Measured Backscatter for Multiyear Ice.

volume sets the actual backscattering value while the thickness decreases or increases the fluctuations. The thicker the ice becomes the more the fluctuations are damped.

3.6.2 Multiyear Backscatter Values

Low-resolution ERS-1 SAR images were obtained for an area in the high Arctic within a radius of 30 km located at 81.5°N latitude and 170.0°W longitude for the period of 1 October 1991 to 30 March 1992. As might be expected this area is dominated by multiyear ice with a typical area percentage cover of 95–97%. In an attempt to measure the stability of the backscatter from multiyear sea ice, values were extracted

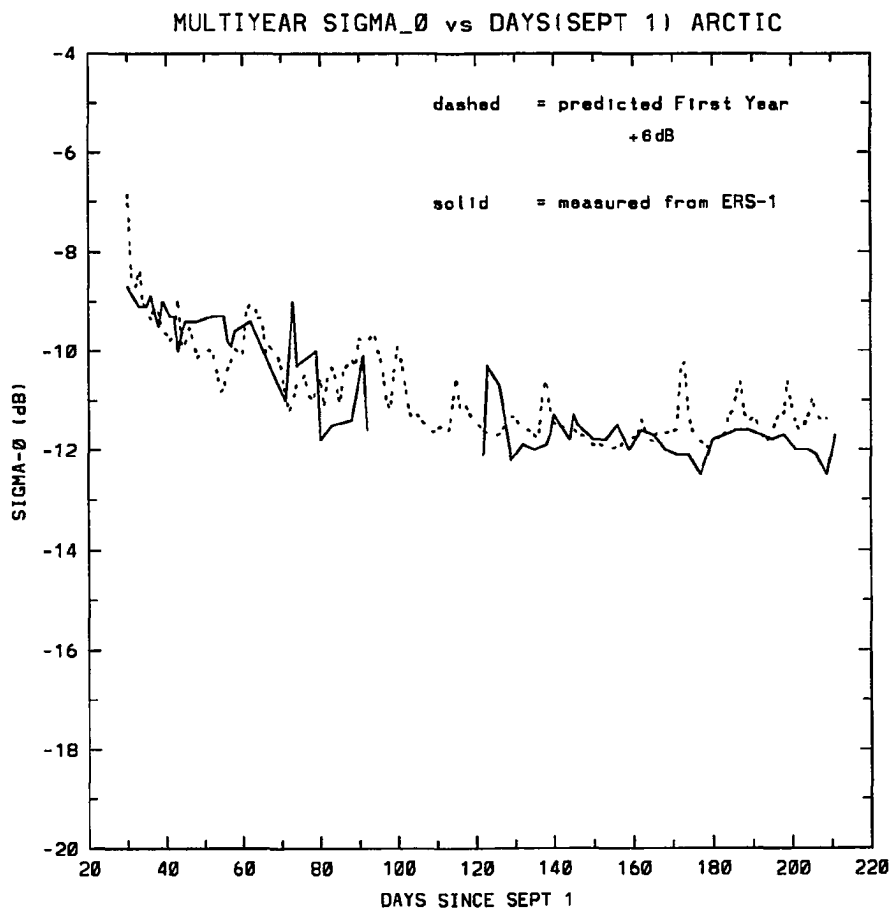


Fig. 27. Multiyear Predicted and Measured Backscatter.

from the ERS-1 images every three days and corrected radiometrically according to the procedure outlined in Appendix A. The recorded values are shown in Figure 26. Also shown is the predicted backscatter curve for first year ice. One of the most obvious features of this plot is the similarity to the backscattering plots of first year sea ice, showing generally decreasing values plus a scatter presumably caused by short-term temperature fluctuations. Multiyear returns appear to be approximately +6 dB above the first year returns.

Figure 27 shows the result of rescaling the first year ice backscatter values by adding

+ 6 dB to the original values. The fit to this curve is quite reasonable and the results are very surprising in that multiyear ice seems to react to the meteorological temperature fluctuations in the same manner as first year ice.

Chapter 4 Ice Thickness Estimates

4.1 Introduction

Although on a large scale, the ice cover may appear to be a uniformly smooth sheet of ice, in reality it consists of a large grouping of individual pieces with a variety of geometrical, physical, chemical and thermal properties. One of the major factors in determining the properties of sea ice is its overall thickness. Variations in thickness have a substantial influence upon the mechanical strength (compressive, flexural and tensile), the growth rate, the surface temperature, the thermal exchange between the ocean and atmosphere, the salt content of the ice and the salt rejection rate into the ocean. The ice thicknesses in any given region of the polar ocean may range from zero in open leads and polynyas to tens of meters for highly deformed ice in rubble fields and ridges. Each thickness class of the ice reacts differently to the mechanical and thermal forcing which are continually transforming the pack depending upon its internal structure and growth history.

The thickness at any point on the ice cover is the result of two processes: first, the thermodynamic processes of freezing and melting which are ramifications of changes in the heat balance between the ocean and atmosphere and second, the mechanical processes of ridging and lead formation which are a response to the internal and external stresses exerted on the ice cover. Each of these actions tends to generate ice of specific thicknesses if allowed to operate for a specific period of time. For example, the thermodynamics of ice growth and decay will ultimately produce ice tending towards a mean ice thickness determined by the meteorological conditions of the region (Zubov, 1945; Maykut and Untersteiner, 1971). On the other hand, the mechanical processes of ice dynamics tend to create a deformation continuum ranging from many small deformation features to a few extreme features. The end result of these deformations

shifts the ice thickness distribution by adding both to the very thin end via the formation of thin ice in leads and to the thick end by the ridging process.

The problem of delineating the thickness distribution in pack ice areas has been addressed by many investigators since the idea was put forth by Thorndike et al. (1975). Even though most of these attempts have not been particularly successful, most investigators agree that the mean thickness of undeformed multiyear ice in the Arctic is in the range of 3 to 5 meters. The reason for this variation is that the ice thickness is extremely variable in both time and space. This characteristic of sea ice and the fact that, at present, there is no instrument that will measure ice thicknesses on anything other than a very local scale, makes estimating the ice thickness distribution a very difficult problem.

Ice thickness estimations fall into three major categories (Wadhams and Comiso, 1992); direct measurements, indirect measurements and theoretical approaches. The direct approach utilizes such instruments as upward-looking sonar and active electromagnetic devices such as laser profilometers and impulse radars. All of the direct methods are limited by their narrow swath widths and the major expense of operating an instrument platform such as an aircraft or submarine. Also, to date, only a limited amount of the upward-looking sonar data that has been collected by the Navy has been made available to the science community. The indirect methods generally infer the ice thickness by measuring some ice thickness-dependent quantity such as emitted passive microwave energy. For instance, passive and active microwave observations can be used to place ice in the multiyear (MY) category which also implies that its thickness is > 2.5 m. The major problem with inferring the thickness is the lack of adequate models which are required to relate the measurements with real ice thicknesses.

The theoretical approach has been outlined by Thorndike et al. (1975), and Thorndike (1992). In this approach the evolution of the thickness distribution is described by a differential equation involving the three terms of advection, growth and redistribution. Once accurate estimates of each of the terms are available this approach could lead to

an adequate statistical characterization of pack ice on the regional scale.

In the present study a combination of theoretical and indirect measurements will be utilized to estimate the distribution of ice thickness. Three ice types will be defined and ice classifications will be performed on SAR images to determine the percentage of area covered by each type. Each image will then be divided into percentages of new ice/open water, of first year ice and of multiyear ice. In addition, the theoretical ice growth model developed here will be used to provide an estimate of the ice thickness for each ice type.

Each ice type will have a thickness that depends on the date of observation. For example, first year ice in October will have a maximum possible thickness which is much lower than the maximum possible thickness of FY ice in March. While it is possible the FY ice observed in March will have the same thickness as that observed in October, it is not possible for ice observed in October to have the same thickness as that observed in March. Therefore, it seems incorrect to use the same ice thickness estimate for all cases and since the thickness distributions within each class are unknown, the mean of all possible thicknesses was chosen.

The thickness estimate for the new ice/open water ice type will be $1/2$ the maximum theoretical thickness grown from the previous 2 days. For the first year ice type, the thickness will be $1/2$ the maximum thickness of the oldest first year ice (i.e. $1/2$ the thickness of the ice that began growing on the first day of freeze-up which was taken to be 1 October 1991). Multiyear ice estimates will be calculated for ice with a starting thickness of 200 cm and 300 cm on 1 October 1991.

4.2 Supervised Ice Type Estimates

Low-resolution (240 m) SAR images were obtained within a 30 km radius of 81.5°N latitude 170.0°W longitude on approximately a three day repeat cycle beginning on 1 October 1991 and ending on 30 March 1992. These images were radiometrically corrected to remove the system noise and to correct for any antenna or range variations

present in the image. The digital values for each pixel were processed and converted to the log values corresponding to the differential backscattering coefficient (σ^o). The σ^o values were then mapped onto a 255 level grey scale representing a dynamic range for the signal from -25.5 dB to 0.0 dB where the grey scale value of 0 representing a σ^o of -25.5 dB. A more extensive explanation of these radiometric corrections is provided in Appendix A.

A supervised ice classification was performed on each image by executing a clustering routine on the pixels in the intensity domain to determine the dominant ice types. Then, a training area was manually defined for each ice class present in the image and statistics were generated to determine the maximum, minimum, mean and standard deviation. A theoretical backscattering value for first year ice was calculated each day using the ice growth and backscatter models of the previous chapters. These predicted values were used as the mean for the FY ice class and applied to the image corresponding to the day of the prediction. The statistics from the training areas for MY ice and new ice/open water and the predicted FY ice values were then used as inputs into an optimal thresholding technique based on a maximum likelihood classification scheme.

The maximum likelihood classification provides an optimal approach to labeling pixels when the expected variations within each ice type are large and the distributions are well known. The pixels are classified such that for a given pixel value x and ice cluster C_i , the distribution densities $p(x/C_i)$ and the a priori probabilities $P(C_i)$ are maximized so that

$$x \sim C_i \quad P(C_i) p(x/C_i) = \text{maximum} \quad (4.1)$$

Table 12 in Appendix B shows the percent coverage values derived from the supervised classification scheme as described above giving the areal coverage and an estimate of the predicted maximum ice thickness for each ice type as a function of date. Figure 28 shows the areal percent coverage of each ice type with the multiyear ice type scale reduced by 90 (i.e. values of 8 for multiyear ice represent 98% coverage).

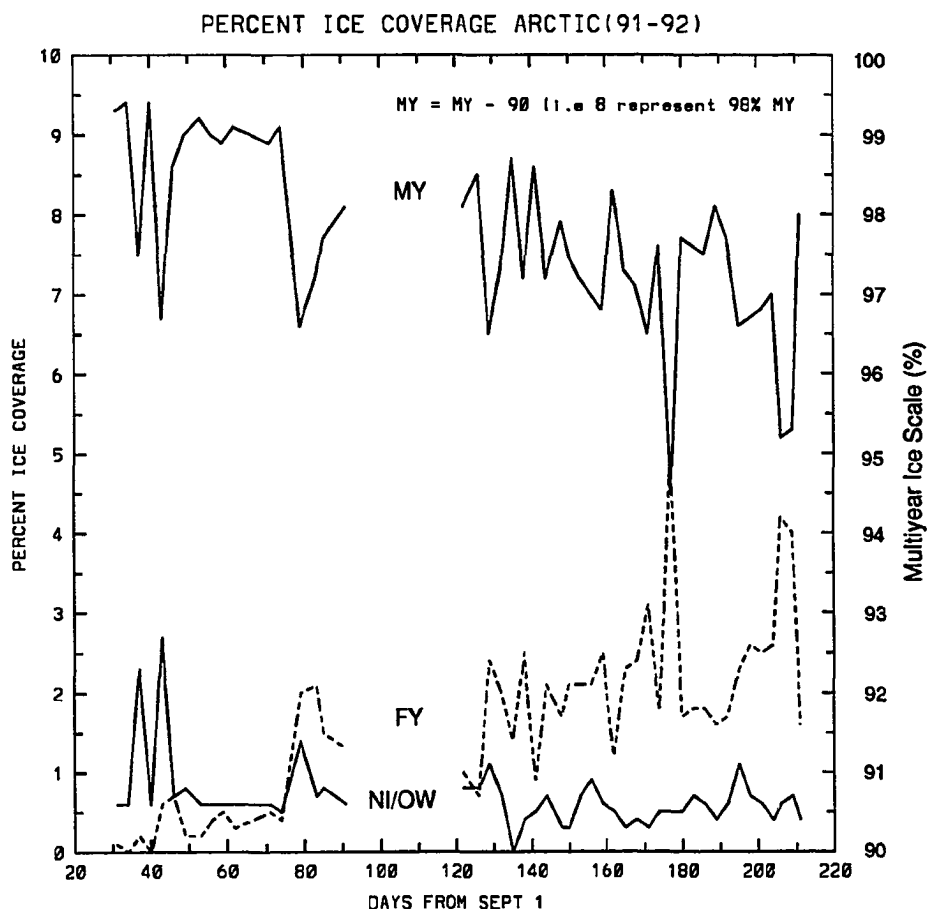


Fig. 28. Area Coverage For multiyear (MY), first year (FY) and new ice/open water (NI/OW).

The data gap between 1 December 1991 and 1 January 1992 was due to a change in the satellite orbital parameters. Prior to 1 Jan. 92 the ERS-1 satellite was in the Commissioning Phase (6 Aug. 91 to 9 Dec 91) of the mission. This portion of the mission was designed to allow the satellite systems to stabilize prior to reaching full operational capacity. However, in retrospect, the data collected by the satellite during the Commissioning Phase proved to be quite acceptable. At the end of the Commissioning Phase, ERS-1 was repositioned into a stable three day repeat orbit with the satellite track displaced approximately 40 km west of the orbits of the Commissioning Phase.

This new orbital course was known as the Ice Phase which began 28 Dec. 91 and ended on 2 Apr. 92.

A discussion seems appropriate here regarding the general interpretation of the sea ice types in SAR imagery. At the present time, there is a controversy concerning the multiyear ice fraction in the high Arctic. Passive microwave estimates of the multiyear ice fraction range from 54 to 92% with a typical value around 80% (Parkinson et al. 1987). The 54% value is derived from the difference in total ice extent in the winter and summer with the reasoning that the ice that exists at the end of summer will become the multiyear ice fraction in the winter. The current SAR interpretation of the winter multiyear ice fraction range between 90 to 95% (Kwok personal communication). The 90 to 95% values were also observed in this study with the following caveat. While observing MY ice in SAR images from October to the end of March, the multiyear ice backscatter progressively darkens (see figure 26). The darkening appears in the form of "blotchy" or "grainy" areas within the larger assumed multiyear floes. These dark areas were also observed by Gineris and Fetterer (1993) and the generally accepted interpretation of these dark areas is that they are melt ponds on top of multiyear ice floes. However, the backscattering values and the backscatter history with its slow decrease are consistent with those of first year ice. As these darker areas represent 15 to 20% of the total multiyear area, they would have a substantial impact on the heat flux if they were FY ice or melt ponds. It seems that if there were a substantial amount of open water in the high Arctic during the summer, that random close packing of the multiyear floes during the winter would produce a high percentage of open spaces which would eventually become first year ice. This is an important point that needs further investigation. However, for this study the conventional view will be taken and the interpretation of the dark grainy areas will be that of melt ponds over multiyear ice.

4.3 Unsupervised Ice Type Estimates

Unsupervised classifications were performed on each of the images within the study area. This was accomplished by utilizing the automatic ice classification scheme currently being run by the Geophysical Processing System at the Alaskan SAR Facility. This system lauses a clustering approach to the problem of identifying various ice types plus a lookup table established by R. Kwok, E. Rignot and B. Holt (Kwok et al. 1992). It is also assumed that the multiyear signature remains stable throughout the winter with a value of -10.0 dB. As was noted earlier in this study, observations show that this is not true. The ice type look-up table currently in use in the GPS software is presented in Table 3.

Table 3. Lookup Table for JPL Classification Algorithm.

Principal Type Ice type	Mixtures of ice types	Backscatter Table in dB with (S.D.)
Multiyear/Old Ice	Multiyear, Deformed First Year, Ridges	-10.0 dB (1.0)
Fisrt Year type 2	Deformed First Year	-14.0 dB (1.0)
First Year Type 1	Undeformed FY	-17.0 dB (1.3)
Open Water/New Ice	Smooth ice, new ice, Nilas, Smooth open water	-22.0 dB (1.7)

It should be noted that the unsupervised ice classification scheme by JPL is only believed to be accurate between the day of the year (DOY) 270 and 120 for locations north of 73° latitude and at temperatures below $-10^\circ C$. For the 1991–92 ice season, this translates into the days between 27 September 1991 to 29 April 1992.

Table 4. Supervised vs Unsupervised Ice Coverage Comparison.

Classification Scheme	<OW/NI percentage>	<First Year Ice percentage>	<Multiyear Ice percentage>
Supervised	0.7	1.6	97.7
Unsupervised	0.1	5.0	94.9

The table 13 (Appendix B) presents the ice types as classified by the unsupervised scheme of the GPS with the two classes (FY and Ice Type 4) combined into one first year class.

There are several major differences in the estimated percentages for the various ice types between the supervised and the unsupervised classification schemes. This is not particularly surprising since it is clearly very difficult to develop an adequate unsupervised classification considering the large signature variation shown by sea ice. In general, the supervised classification produced higher percentages for both the multiyear ice and open water/new ice classes, while the unsupervised scheme produces a higher percentage of first year ice as shown in Table 4.

In addition, the unsupervised classifier occasionally classified the entire image as first year ice (25 Feb.92, and 2 Mar.92), a condition that is extremely unlikely considering the high latitude of the area and time of year. The cause of this difficulty would appear to be the slow decrease in the backscatter of multiyear ice which decreased almost 4 dB during the study period while, as mentioned earlier, the classifier assumed a constant value for multiyear backscatter of -10.0 dB with a standard deviation of 1.0 dB. When the multiyear ice signature drops below about -12.0 dB, the classifier considers these pixels to be first year ice. The slow drift in the backscatter values for multiyear ice also cause an increase in the percentage of multiyear ice that is misclassified as deformed first year ice. The result is a clear overestimate of first year ice occurrence and an underestimate of multiyear ice in the unsupervised classification. Therefore the

supervised classification scheme is believed to be superior and its results are taken as the better estimate of the areal coverage of the different ice types. The heat and mass fluxes that follow were made using these results.

..

Chapter 5 Flux Calculations

5.1 Introduction

Sea ice is an excellent insulator with the amount of heat that flows through an ice sheet in the Arctic influenced by many factors such as the thickness, thermal conductivity, heat capacity, and density of the ice as well as the meteorological conditions. While examples of the importance of the meteorological conditions and the thermal properties of the ice have been discussed in the previous sections, the major variable controlling the heat flux through the ice at any given time is its thickness. Thin ice conducts far more heat per unit area from the ocean to the atmosphere than does thick ice. For example, thin ice will be shown to have a heat flux density up to 30 times greater than thick ice. Nevertheless, the major contributor to the overall heat flux in the 100×100 km high Arctic area under study is the thicker multiyear ice which accounts for approximately 5 times the heat flux of thin ice as the result of the fact that over 95% of the ice (areally) in this part of the Arctic appears to be multiyear ice.

All of the following flux calculations are derived from the basic surface energy balance equation (2.1) as described in Chapter 2 with smoothed data inputs for the incoming shortwave and longwave radiation and actual meteorological inputs for the ambient air temperature and wind speed. The reader is again reminded that the snow accumulations were set to zero in these simulations for lack of quantitative data. Also the reader should be aware that there is an error introduced by using smoothed incoming radiation inputs in conjunction with real meteorological inputs as the result of emitted longwave, the incoming shortwave, and the turbulent heat flux being coupled to the meteorological inputs. This will be discussed in the final chapter.

In the following discussion, several descriptive terms will be used that are defined as follows:

$$\text{Net Radiation} = (1 - \alpha) F_r - I_o + F_l - F_E \quad (5.1)$$

$$\textit{Turbulent Heat} = F_s + F_e \quad (5.2)$$

$$\textit{Emitted Longwave} = F_E \quad (5.3)$$

with the standard terms calculated as defined previously. Using the descriptive terms and rearranging, the surface energy balance equation becomes

$$\textit{Net Radiation} + \textit{Turbulent Heat} = -F_c - F_o \quad (5.4)$$

For convenience, throughout the remainder of this dissertation the term heat flux density (W/m^2) will be used as the units for all terms in equation 5.4.

A word of caution is in order here regarding the average values calculated in the next several sections. There are two methods of calculating the average flux and they result in different values. The first method takes the average value of the daily flux densities and multiplies by the average area covered. The other method involves taking the average value of the daily fluxes. In the following tables the first method was utilized.

5.2 New Ice / Open Water Fluxes

The ice thickness estimate for open water/new ice will be a function of the timing of the image data taken to observe the amounts of the different ice types present. As the SAR repeat interval was generally every 3 days, the ice thickness estimate for the open water/new ice class will be taken as 1/2 of the maximum ice thickness grown in the previous 2 days as explained previously. The estimates of the daily heat flux values for this ice category are given in Appendix C. On the average during the whole study period from 1 October 1991 to 30 March 1992, the heat flux for this ice type in the high Arctic study area was $-250.4 W/m^2$. Taking the average areal coverage of 0.7% for this ice type from the supervised classification presented in Table 4, the area

Table 5. New Ice/Open Water Heat and Salt Flux Summary.

New Ice / Open Water Ice Class	Thickness Range (5.3 - 6.9 cm)
Average Percentage of Total Area	0.7%
Average Area Covered	70.0 Mm ²
Average Heat Flux Density	-250.4 W/m ²
Average Heat Flux	-17.5 GW
Area Averaged Heat Flux Density	-1.8 W/m ²
Average Salt Flux Density	1.5 kg/day/m ²
Average Salt Flux	96.3 Mkg/day
Area Averaged Salt Flux Density	0.0096 kg/day/m ²

covered by this category is $70 \times 10^6 \text{ m}^2$ which contributes an average of $-17.5 \times 10^9 \text{ W}$ or -17.5 GW of heat. However, for an area averaged flux density value, this corresponds to a value of only -1.8 W/m^2 .

To get a better feel for these numbers, an average heat flux density of -250.4 W/m^2 is equivalent to lighting a 250 W light bulb every meter on a 1 meter grid for an area with dimensions of $8.4 \times 8.4 \text{ km}$. To obtain an area averaged flux density of -1.8 W/m^2 the 250 Watt bulbs would be replaced by a 1.8 Watt bulb. Additional values for the new ice/open water class are shown in Table 5.

The salt fluxes which consist of the initial brine rejection plus the expulsion and drainage through the bottom ice layer can also be calculated from the growth velocity and the brine expulsion and gravity drainage terms as discussed in Chapter 2. The initial salt rejection can be estimated from

$$F_{salt_r} = \rho_i f(H) [1 - k_{eff}] S_w \quad (5.5)$$

where

ρ_i is the density of the ice (918 kg/m^3),

$f(H)$ is the growth velocity (m/s),

Table 6. First Year Ice Heat and Salt Flux Summary.

First Year Ice Class	Thickness Range (7.8 - 80.9 cm)
Average Percentage of Total Area	1.6 %
Average Area Covered	160.0 Mm ²
Average Heat Flux Density	-43.9 W/m ²
Average Heat Flux	-7.0 GW
Area Averaged Heat Flux Density	-0.7 W/m ²
Average Salt Flux Density	0.33 kg/day/m ²
Average Salt Flux	52.8 Mkg/day
Area Averaged Salt Flux Density	0.0053 kg/day/m ²

k_{eff} is the effective distribution coefficient, and

S_w is the salinity of the unfrozen sea water.

The daily salt flux values are presented in Appendix D and represent the sum of the initial rejection, the expulsion term and the drainage term for each day. For the new ice/open water category the average salt flux contribution per square meter is about 1.5 kg m^{-2} per day, while the area averaged value, which represents the total new ice/open water contribution distributed over the entire $100 \times 100 \text{ km}$ area, is only 9.6 g m^{-2} per day. So, while the local salt contribution can be very high, the area-wide contribution is still fairly low. In fact, although the total new ice/open water salt flux is higher than the contribution from the first year ice, it is only roughly $1/7$ of the salt flux from the 2 m multiyear and $1/5$ that of the 3 m multiyear.

5.3 First Year Ice Fluxes

The ice thickness estimate for first year ice will also be a function of the time of year the ice classification image was taken. In this study the thickness estimates for the first year ice type will be assumed to be $1/2$ the maximum thickness of the oldest first year ice (i.e. $1/2$ the thickness of the ice that began growing on the first day of freeze-up).

Table 6 shows the representative values of both the heat and mass fluxes for first year ice. The average flux density for first year ice ranging in thickness between 7.8 and 80.9 cm from 1 Oct. 1991 to 30 Mar. 1992 is 43.9 W m^{-2} . Using the average percentage of first year ice from the supervised ice classification scheme of 1.6%, the total average area is $160 \times 10^6 \text{ m}^2$ and the total average heat flux for first year ice is 7.0 GW. This corresponds to an area averaged value of 0.7 W m^{-2} . The average percentage of first year ice from the unsupervised ice classification scheme is 5.0%, representing a total area of $500 \times 10^6 \text{ m}^2$ and producing an average heat flux for first year ice of 22.0 GW and an area average contribution of 2.2 W m^{-2} .

The area-average salt fluxes for first year ice are generally an order of magnitude lower than those of both thicknesses of multiyear ice. The salt flux density of first year ice is about $1/3 \text{ kg}$ per square meter per day which is equivalent to $333 \text{ g day}^{-1} \text{ m}^{-2}$. However, the area-averaged contribution is $5.3 \text{ g day}^{-1} \text{ m}^{-2}$.

5.4 Multiyear Ice Fluxes

Multiyear ice flux density calculations were performed using ice thickness estimates of 200 cm and 300 cm on 1 October 1991. The ice thickness was then allowed to grow as the season progressed producing ice of 243.3 cm and 330.3 cm by 30 March 1992. The two ice thicknesses were used to estimate the effect that a 33% increase in ice thickness would have on the overall flux estimates, with the result showing only an 11% decrease in the average heat flux contribution.

Tables 7 and 8 show the average flux and mass values for the two different thicknesses of multiyear ice. The large percentage of area covered by multiyear ice makes it the biggest contributor to both the overall heat loss to atmosphere and the salt infused into the ocean mixed layer. While the flux densities of multiyear ice are relatively small when compared to the younger ice types, when multiplied by the huge area covered the resulting effect is a large flux component. For example, the heat flux

Table 7. 2m Multiyear Ice Heat and Salt Flux Summary.

2m Multiyear Ice Class	Thickness Range (199.1 - 239.4 cm)
Average Percentage of Total Area	97.7 %
Average Area Covered	9770.0 Mm ²
Average Heat Flux Density	-8.4 W/m ²
Average Heat Flux	-82.1 GW
Area Averaged Heat Flux Density	-8.2 W/m ²
Average Salt Flux Density	0.067 kg/day/m ²
Average Salt Flux	654.6 Mkg/day
Area Averaged Salt Flux Density	0.066 kg/day/m ²

Table 8. 3m Multiyear Ice Heat and Salt Flux Summary.

3m Multiyear Ice Class	Thickness Range (299.9 - 330.3 cm)
Average Percentage of Total Area	97.7 %
Average Area Covered	9770.0 Mm ²
Average Heat Flux Density	-7.5 W/m ²
Average Heat Flux	-73.1 GW
Area Averaged Heat Flux Density	-7.3 W/m ²
Average Salt Flux Density	0.044 kg/day/m ²
Average Salt Flux	431.9 Mkg/day
Area Averaged Salt Flux Density	0.043 kg/day/m ²

density of the new ice/open water type is -250.4 W m^{-2} which is more than 30 times that of both multiyear ice values (-8.4 W m^{-2} for 2m and -7.5 W m^{-2} for 3m). However, while the area averaged value of new ice/open water goes down to -1.8 W m^{-2} , the values for multiyear ice remain nearly the same as the unaveraged values at -8.2 W m^{-2} for 2-m and -7.3 W m^{-2} for 3-m.

An interesting calculation that can be made is the crossover percentage where the new ice/open water area averaged heat flux contribution becomes larger than the multiyear contribution. If the only two ice types were present in the study area were

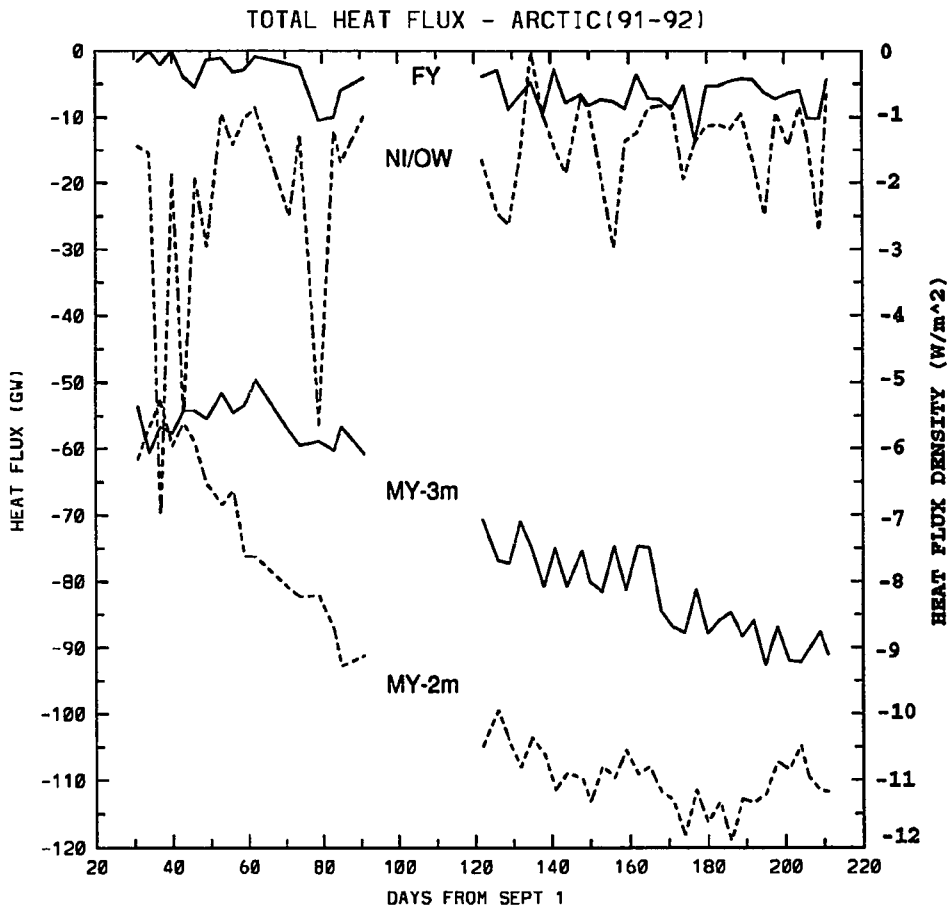


Fig. 29. Area Total Heat Flux For MY-2m, MY-3m, FY and NI/OW.

open water/new ice and multiyear ice and using the average values for the heat flux densities, at what percentage would the two contributions be equal? This cross-over point is around 3% open water/new ice (97% multiyear ice) with the value being slightly higher for the 2-m multiyear ice and slightly lower for the 3-m multiyear ice.

Figure 29 is a plot of the total heat flux contribution by each ice type with the negative sign indicating a flux away from the ice surface and into the atmosphere. In general, the thinner ice types contribute 5 to 10 times less heat over the growth season than the multiyear ice contribution, except early in the winter when the new ice/open

Table 9. Monthly Heat Flux Densities After (Maykut, 1982).

W/m ²	Oct.	Nov.	Dec.	Jan.	Feb.	Mar.	Average
NI/OW	-1.7	-2.5	-1.5	-1.2	-0.7	-1.5	-1.5
FY	-5.1	-9.7	-12.3	-7.3	-4.8	-5.5	-7.5
MY	-12.9	-13.5	-11.6	-11.6	-12.5	-8.6	-11.9
TOTAL	-19.7	-25.7	-25.4	-20.1	-18.0	-15.6	-20.9

Table 10. Monthly Heat Flux Densities for Current Study.

W/m ²	Oct.	Nov.	Dec.	Jan.	Feb.	Mar.	Average
NI/OW	-2.5	-2.2	-1.0	-1.4	-1.5	-1.4	-1.7
FY	-0.2	-0.5	-0.4	-0.6	-0.7	-0.6	-0.5
2m-MY	-5.9	-8.4	-9.1	-10.7	-11.1	-11.1	-9.4
TOTAL-2m	-8.6	-11.1	-10.5	-12.7	-13.3	-13.1	-11.6
3m-MY	-5.5	-5.7	-6.1	-7.6	-8.2	-8.9	-7.0
TOTAL-3m	-8.2	-8.4	-7.5	-9.6	-10.4	-10.9	-9.2

Table 11. Soviet NP-23 and NP-4 Heat Fluxes.

W/m ²	Dec.	Jan.	Feb.	Mar.	Average
NP-23	-7.0	-11.2	-14.7	-16.8	-12.4
NP-4	-9.1	-13.3	-14.7	-7.0	-11.0
TOTAL-2m	-10.5	-12.7	-13.3	-13.1	-11.6
TOTAL-3m	-7.5	-9.6	-10.4	-10.9	-9.2

water term actually exceeds that of the multiyear. This figure (Figure 29) also represents the area averaged flux densities as indicated by the scale on the right-hand side of the plot.

5.5 Comparison of Flux Results With Previous Studies

Figures 9 and 10 show the monthly heat flux densities as estimated by Maykut (1982) and the equivalent values calculated in this study.

A more recent study by Makshtas (1991) calculates the heat flux of multiyear ice from observations taken at the Soviet ice camp North Pole 23 during the 1976–77 ice season and North Pole 4 during the 1956–57 season. The errors in the linear temperature profile assumption were estimated and removed from the calculations and the results for December through March with the current totals for the 2 *m* and 3 *m* multiyear ice are presented in figure 11 . The results of the Soviet study are in much better agreement to the findings of the present study.

Area averaged salt flux calculations during the ice growth season by Maykut (1982) indicate a range from 1 to 5 kg mo⁻¹ m⁻² compared to the current values of 1.7 kg mo⁻¹ m⁻² and 2.4 kb mo⁻¹ m⁻² derived from the 3m-MY and the 2m-MY totals respectively.

Chapter 6 Summary and Recommendations

6.1 Sea Ice Growth

The growth of sea ice appears to be a simple problem when a linear temperature profile and constant thermal conductivity are assumed. However, in reality, the non-linearities and the inter-dependencies between the growth rate, desalination processes and the various thermal parameters create a very complex feedback structure which can have a profound effect on the ice. It was discovered that the initial freezing conditions encountered by a given ice sheet could enhance or retard the overall growth rate by altering the conducted heat flux. A forming ice sheet with initially high growth velocities will entrap excessive amounts of brine in its upper layers causing an increase in the salinity, brine volume and thermal capacity, which in turn, will lower the thermal conductivity, conducted heat flux and ultimately long-term growth rate.

The development of a non-linear ice growth model has facilitated our understanding of the growth processes and physical properties of sea ice. The program produces realistic ice thicknesses and ice properties when the meteorological conditions are known. It does have the shortcoming of using an averaged and smoothed incoming solar radiation primarily due to the fact that these types of measurements are not readily available. The major difficulty in using this approach arises from the fact that the emitted longwave radiation, which is the major contributor of outgoing energy in the winter, is a function of the incoming shortwave and longwave radiation and the ambient air temperature and these terms are not independent variables. It is difficult to estimate the error introduced in using this approximation primarily because the correlation between the incoming radiation and the ambient air temperature is not well understood, especially with the introduction of a cloud cover. For example, under cloudy conditions the incoming shortwave is reduced, the incoming longwave is increased, the ambient temperature generally increases and the emitted longwave is high. In the model, if the temperatures

are above the average the ice surface temperature will generally be higher and the longwave emitted will be overestimated because, using the average value, the incoming longwave will have been underestimated. For these conditions the ice growth will be overestimated. In the reverse case, where the temperatures are low relative to the average, it is even difficult to estimate the direction of the error, since in cold conditions the skies may be clear or there may be ice fog each altering the estimates in different directions. Figure 30 shows the 1991–92 Unidata predicted ambient air temperatures for the high Arctic plotted against the historical average air temperatures which correspond to the averaged incoming radiation. Any deviation from the mean temperature would introduce an error in the flux calculations as mentioned above. Unfortunately, the effects of cloud cover on incoming solar radiation and air temperature are beyond the scope of this thesis, although it is quite evident that this is an area that needs further research and parameterization.

The results of the multiyear ice simulations were very encouraging. With the very arbitrary desalinization routine that was implemented the calculated salinities and temperature profiles were within reasonable limits. In addition, while running the simulations with only gravity drainage and brine expulsion through the summer, a qualitative estimate of the important role that meltwater flushing plays in the desalinization of multiyear ice was highlighted. The need for a parameterization of these processes is evident.

Although the multiyear simulations were initially a sideline, it is believed that the present results indicate that if a realistic parameterization of the summer desalinization processes could be added to the current model that the resulting combination should be capable of simulating the complete ice growth, ice temperature, ice salinity and brine volume of an undeformed sea ice sheet from the formation of the initial ice skim to the development of a steady state floe.

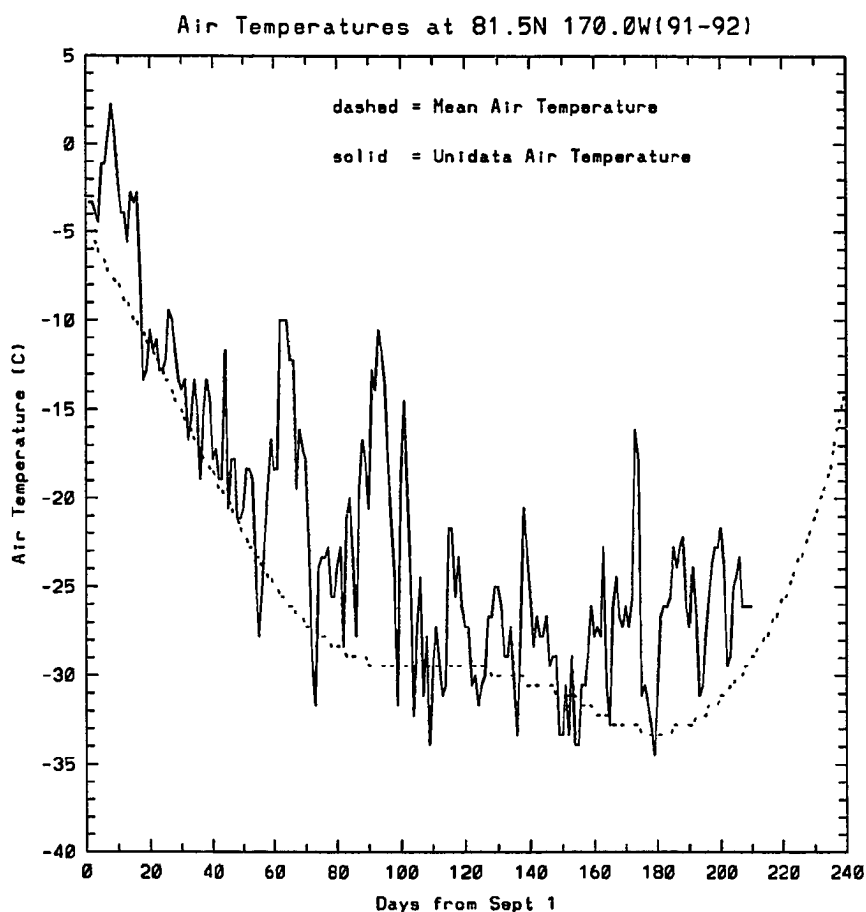


Fig. 30. Arctic Air Temperatures vs Average Air Temperatures.

The most obvious missing factor in the ice growth model simulations was the absence of snow. While the current model does have the capability to consider the effects of a snow cover on all aspects of sea ice growth and the effect is known to be significant, a lack of quantitative data necessitated its removal from the simulations. However, an estimate of the overall snow effect on the growth rate of first year sea ice may be seen in figure 17 where the accumulated freezing-degree-days were plotted for two versions of the non-linear model. The difference in growth rate between the 1:1 non-linear and the 1:3 non-linear model was equivalent to an accumulated snow

depth of 20 cm. Once a reliable parameterization of the snow cover is formalized its incorporation into the model is straightforward. This is obviously an area that is desperately in need of sequential field observations.

6.2 Backscattering Model

The radar backscattering model for first year sea ice that was developed in this thesis was based on the assumptions of a Lambertian surface and a strong dielectric dependence on brine volume. Using the calculated physical properties of the ice growth model, the penetration depth for C-band radar was determined and the active layer dielectric constant was input to the surface scattering model to produce predicted σ^o values for first year sea ice. The comparison of the predicted first year ice σ^o values to those obtained from ERS-1 SAR images of landfast ice at Dease Inlet proved to be surprisingly good considering the assumptions of the model. The large variations in the backscatter were strongly correlated to changes in the dielectric constant caused by the high sensitivity of the brine volume to temperature and desalinization. Thus, SAR imagery indirectly senses the thermal state of first year sea ice, and the possibility of detecting an ice thickness signal through the brine volume sensitivity becomes real. However, while the high sensitivity to temperature opens the possibility of a thickness signal, the large variations in thermal forcing as a result of changing meteorological conditions tend to mask the signal behind a noisy background making retrieval more difficult.

With the thermal state sensing in mind, another possible view of SAR imagery is to exploit the thermal sensing capabilities more and the thickness estimating ability less. The temperature of the upper portion of the ice sheet will have a significant effect on the brine volume and subsequently the radar return. If the quantities of interest here are the fluxes through the ice surface, it may be possible to relate the radar return to the surface temperature, similar to passive microwave, and produce high spacial resolution thermal

maps of the ice rather than ice thickness maps. In this sense it would be interesting to explore the results of the coupled application of SAR and infrared (IR) data.

The agreement between the predicted σ^0 values and the observed values, although generally satisfactory, showed marked differences in areas where the model clearly failed. A clear example of this may be seen late in the season when the ice temperature begins to rise. The discrepancy in signals during this general warming may be due to the presence of liquid water in the snow layer which has the effect of dramatically decreasing radar backscatter. The use of a more sophisticated backscattering model which incorporates the effects of liquid water in the snow layer as well as a more extensive treatment of volume scattering would undoubtedly increase the applicability and hopefully increase the effectiveness of the current model.

One result which was completely unexpected was the reasonable fit of the rescaled first year ice predicted signature with that of the observed multiyear backscatter. It appears that the multiyear ice reacts to the meteorological forcing in much the same way as the first year ice with the exception of an increased multiyear return. While the finding was unexpected, in retrospect, the results appear reasonable considering multiyear ice generally consists of a low density layer above the water level or freeboard and looks basically like first year ice below. It appears that the low density layer with its high bubble content produces an additional backscatter component which remains relatively constant during meteorological fluctuations, while the lower layers produce variations in the return similar to the signature seen in first year ice. This result casts considerable doubt on the generally accepted view that the winter signature of multiyear remains stable near -10 dB.

6.3 Areal Coverage of Ice Types and Thickness Estimates

In chapter 4 the results of the previous chapters were utilized along with an ice classification scheme to produce estimates of the areal coverage for three main ice types.

The results of this procedure indicated that the dominant ice type in the high Arctic during the winter months was clearly multiyear ice with an average percentage of 97.7% (supervised) or 94.9% (unsupervised). These results were based on the conventional SAR view that the winter multiyear fraction in the Arctic was near 95% and that the darkening seen in the time sequence of images was due to the appearance of refrozen melt ponds. The wisdom of this choice needs to be investigated further since preliminary results show that the area involving the melt ponds consists of nearly 20% of the total image and would have a significant effect on any flux calculations if these areas differ appreciably from multiyear ice. The signature history of these dark areas appears to be consistent with first year ice in that the winter returns initially show values near multiyear ice and are followed by a slow decrease in backscatter with the final signatures approaching the first year values. However the response during the middle of the season is unique, with values dropping much slower initially than those of first year ice. These signatures have some characteristics of first year ice and some of multiyear ice and obviously need to be investigated further.

In the classification scheme utilized for ice discrimination, the predicted first year backscatter value was used as the mean value statistic for the first year ice class. This procedure provided only a minimal use of the predictive capabilities of the backscattering model. The digital image analysis problem of unique pixel clustering for classes with closely similar DN values is a very difficult one and is further compounded by the presence of speckle (a type of SAR noise). However, with backscattering values of thin first year and multiyear ice being very similar, this would be an excellent area for further research and could result in an increased ice discrimination capability through the use of SAR images. A method that would use the relationship of neighboring pixels to classify a given ice area would show marked improvement over the current method. If such a method were available a scheme to classify ice in thicknesses bins would be possible and the thickness estimates would be greatly enhanced.

6.4 Flux Calculations

In Chapter 5, heat and mass flux calculations were made for a 100×100 km area using the estimates and model outputs from the previous chapters. The most notable difference in this study and those done previously is the fact that the flux densities are generally lower in the present study. This is not completely unexpected since the majority of the previous studies utilize the linear assumptions discussed in Chapter 2 with the noted results of overestimating the conducted heat flux by a factor approaching 2. While there are considerable differences between the Maykut findings and those of the current study, most notably in the first year ice class, the new ice/open water class values are fairly similar. The multiyear class results are reasonable considering the differences in conducted heat flux between the two studies. That is to say, the thick ice heat fluxes from the Maykut study were expected to be roughly twice those of the current investigation due to the higher conducted heat flux in the linear model. In the thin ice types where the difference in thermal conductivity between the top and bottom of the ice is less, the dissimilarities in the estimated conducted heat fluxes between the two model would also be expected to be less.

The most interesting flux result was seen in the area-wide calculations, with the finding that the multiyear ice was the major contributor to the overall flux. This is somewhat surprising and contrary to previous indications that the new ice and first year ice were the major contributors to the flux. The fact that the multiyear ice areal coverage was so much larger than the younger ice types resulted in its contribution dominating the overall flux. The younger ice types were only able to approach the multiyear ice in flux contributions during the early winter when the bottom of the multiyear ice was still responding to the warming of the past summer.

An illuminating calculation and one that shows the importance of accurate ice type estimates maybe done by assuming the presence of only two ice types in the imagery (e.g. OW/NI and MY or FY and MY) and estimating the areal coverages needed to

produce equal flux contributions. Using the average heat flux densities of -250.4 W m^{-2} for OW/NI, -43.9 W m^{-2} for FY and -7.5 W m^{-2} for MY, the percentage of 3% OW/NI and 97% MY or 15% FY and 85% MY would have equal heat flux contributions.

In conclusion, although this thesis has clarified some aspects of the riddle known as sea ice, it has revealed many more problems than it has solved. The encouraging feature is that in almost all of these cases approaches to resolving the problems are reasonably clear. In a sense this thesis can be taken as verifying the adage that the more you know, the more you don't know.

Appendix A Image Radiometric Corrections

The standard image product from ASF is a full-resolution image of 8192 by 8192 pixels in a 255-level grey scale representations of the received radar amplitude from the sensor. The Low-resolution image is a simple 8 pixel by 8 pixel average of the Full-res image which results in a 1024 pixel by 1024 pixel image. The pixels of each image are presented as 8 bits of amplitude.

The amplitude value contains the radar backscatter intensity, system noise, antenna and range variations and processor variations such as gain control. For the scientific user who is interested in the backscattering coefficient for the objects in the image, he must radiometrically correct these amplitude values.

The radiometric corrections are outlined in "User's Guide To Products". To eliminate the noise and to make the necessary corrections for the antenna pattern, range to the target and incidence of angle, three coefficient (noise scaling, linear conversion and offset) and 256 noise values are required. These values are provided in the Radiometric files of the CEOS leader file accompanying the raw data file.

The coefficients, noise values and data numbers are related to the radar backscatter coefficient (σ^o) by the following formula

$$\sigma_o = 10 \log [a_2(d^2 - a_1 n(r)) + a_3] \quad (\text{A.1})$$

where $n(r)$ is the noise value as a function range. The value of $([a_1 n(r)]^2)$ is the amplitude value of the noise.

The user must be aware that the radiometric corrections are handled differently depending on whether or not the data were processed during or after the Commissioning Phase. During the Commissioning Phase the coefficients given within the radiometric file are in error and they must be calculated from the following functions.

The noise scaling coefficient is

$$a_1 = 406.0 \times 10^{(\gamma)} \quad (\text{A.2})$$

and the linear conversion coefficient is

$$a_2 = 1.2 \times 10^{-(\gamma)} \quad (\text{A.3})$$

where γ is the processor gain divided by 10. After the Commissioning Phase (i.e. after Image ID 7000) the coefficient are included within the radiometric correction file of the CEOS leader.

Appendix B Ice Classification Tables

Table 12. Supervised Ice Classification Results.

Date	NI/OW (%)	NI/OW Max. Thickness (cm)	FY (%)	FY Max. Thickness (cm)	MY (%)
10/01/91	0.6	11.6	0.1	15.6	99.3
10/04/91	0.6	11.0	0.0	22.0	99.4
10/07/91	2.3	10.6	0.2	27.1	97.5
10/10/91	0.6	11.2	0.0	31.5	99.4
10/13/91	2.7	10.6	0.6	35.9	96.7
10/16/91	0.7	11.2	0.7	39.6	98.6
10/19/91	0.8	10.8	0.2	43.2	99.0
10/23/91	0.6	12.0	0.2	48.2	99.2
10/26/91	0.6	13.4	0.4	51.8	99.0
10/29/91	0.6	12.2	0.5	55.8	98.9
11/02/91	0.6	12.0	0.3	59.8	99.1
11/11/91	0.6	11.6	0.5	66.1	98.9
11/14/91	0.5	13.4	0.4	69.0	99.1
11/19/91	1.4	11.0	2.0	74.1	96.6
11/23/91	0.7	12.4	2.1	77.9	97.2
11/28/91	0.8	13.0	1.5	82.4	97.7
12/01/91	0.6	12.4	1.3	84.8	98.1
01/01/92	0.8	12.4	1.0	107.2	98.1
01/05/92	0.8	13.6	0.7	110.1	98.5
01/08/92	1.1	13.0	2.4	112.3	96.5
01/11/92	0.7	13.2	2.0	114.5	97.3
01/14/92	0.0	13.8	1.4	116.7	98.7
01/17/92	0.4	13.2	2.5	118.8	97.2
01/20/92	0.5	13.8	0.9	120.8	98.6
01/23/92	0.7	13.8	2.1	122.8	97.2
01/26/92	0.3	13.8	1.7	124.8	97.9

Table 12. (Continued) Supervised Ice Classification Results.

Date	NI/OW (%)	NI/OW Max. Thickness (cm)	FY (%)	FY Max. Thickness (cm)	MY (%)
01/29/92	0.3	13.2	2.1	126.7	97.5
02/01/92	0.7	13.2	2.1	128.6	97.2
02/04/92	0.9	13.8	2.1	130.6	97.0
02/07/92	0.6	13.0	2.5	132.6	96.8
02/10/92	0.5	13.0	1.2	134.6	98.3
02/13/92	0.3	13.0	2.3	136.5	97.3
02/16/92	0.4	12.6	2.4	138.4	97.1
02/19/92	0.3	12.6	3.1	140.2	96.5
02/22/92	0.5	11.6	1.8	142.1	97.6
02/25/92	0.5	13.4	5.0	143.8	94.5
02/28/92	0.5	13.0	1.7	145.5	97.7
03/02/92	0.7	12.6	1.8	147.1	97.6
03/05/92	0.6	12.6	1.8	148.8	97.5
03/08/92	0.4	13.0	1.6	150.5	98.1
03/11/92	0.6	13.4	1.7	152.1	97.7
03/14/92	1.1	13.8	2.3	153.7	96.6
03/17/92	0.7	12.0	2.6	155.2	96.7
03/20/92	0.6	11.4	2.5	156.8	96.8
03/23/92	0.4	12.8	2.6	158.3	97.0
03/25/92	0.6	12.8	4.2	159.8	95.2
03/28/92	0.7	11.0	4.0	160.7	95.3
03/30/92	0.4	12.0	1.6	161.7	98.0
Average	0.7	12.5	1.6	107.0	97.9

Table 13. GPS Ice Classification Results.

Date	NI/OW (%)	NI/OW Max. Thickness (cm)	FY (%)	FY Max. Thickness (cm)	MY (%)
10/01/91	n/a	11.6	n/a	15.6	n/a
10/04/91	n/a	11.0	n/a	22.0	n/a
10/07/91	n/a	10.6	n/a	27.1	n/a
10/10/91	n/a	11.2	n/a	31.5	n/a
10/13/91	0.6	10.6	0.5	35.9	98.9
10/16/91	0.1	11.2	1.0	39.6	98.9
10/19/91	n/a	10.8	n/a	43.2	n/a
10/23/91	0.0	12.0	0.7	48.2	99.3
10/26/91	n/a	13.4	n/a	51.8	n/a
10/29/91	0.0	12.2	1.3	55.8	98.7
11/02/91	0.0	12.0	0.9	59.8	99.1
11/11/91	n/a	11.6	n/a	66.1	n/a
11/14/91	n/a	13.4	n/a	69.0	n/a
11/19/91	n/a	11.0	n/a	74.1	n/a
11/23/91	n/a	12.4	n/a	77.9	n/a
11/28/91	n/a	13.0	n/a	82.4	n/a
12/01/91	n/a	12.4	n/a	84.8	n/a
01/01/92	0.0	12.4	2.9	107.2	97.1
01/05/92	0.0	13.6	6.2	110.1	93.8
01/08/92	0.4	13.0	3.1	112.3	96.6
01/11/92	0.0	13.2	2.5	114.5	97.5
01/14/92	n/a	13.8	n/a	116.7	n/a
01/17/92	0.0	13.2	2.4	118.8	97.5
01/20/92	0.0	13.8	7.9	120.8	92.1
01/23/92	0.0	13.8	3.7	122.8	96.3
01/26/92	n/a	13.8	n/a	124.8	n/a
01/29/92	0.0	13.2	12.0	126.7	88.0
02/01/92	n/a	13.2	n/a	128.6	n/a
02/04/92	0.1	13.8	3.7	130.6	96.1
02/07/92	0.0	13.0	3.7	132.6	96.2

Table 13. (Continued) GPS Ice Classification Results.

Date	NI/OW (%)	NI/OW Max. Thickness (cm)	FY (%)	FY Max. Thickness (cm)	MY (%)
02/10/92	0.0	13.0	8.5	134.6	91.5
02/13/92	n/a	13.0	n/a	136.5	n/a
02/16/92	n/a	12.6	n/a	138.4	n/a
02/19/92	0.0	12.6	10.5	140.2	89.5
02/22/92	n/a	11.6	n/a	142.1	n/a
02/25/92	0.0	13.4	99.9	143.8	0.0
02/28/92	n/a	13.0	n/a	145.5	n/a
03/02/92	0.0	12.6	100.0	147.1	0.0
03/05/92	n/a	12.6	n/a	148.8	n/a
03/08/92	0.0	13.0	1.9	150.5	98.0
03/11/92	0.0	13.4	12.6	152.1	87.4
03/14/92	0.0	13.8	11.3	153.7	88.7
03/17/92	0.0	12.0	3.0	155.2	97.0
03/20/92	0.0	11.4	13.4	156.8	86.6
03/23/92	0.0	12.8	2.6	158.3	97.4
03/25/92	0.0	12.8	2.4	159.8	97.6
03/28/92	n/a	11.0	n/a	160.7	n/a
03/30/92	0.0	12.0	6.8	161.7	93.3
Average	0.0	12.5	5.0	107.0	97.

Appendix C Daily Heat Flux Tables

Table 14. Daily Flux Densities for NI/OW and FY Ice.

Date	NI/OW 1/2 Max. Thickness (cm)	NI/OW Flux Density (W/m ²)	FY 1/2 Max. Thickness (cm)	FY Flux Density (W/m ²)
10/01/91	5.8	-240.9	7.8	-164.4
10/04/91	5.5	-258.9	11.0	-69.0
10/07/91	5.3	-302.6	13.6	-106.2
10/10/91	5.6	-308.2	15.8	-87.3
10/13/91	5.3	-202.3	18.0	-65.0
10/16/91	5.6	-273.3	19.8	-78.4
10/19/91	5.4	-369.3	21.6	-71.8
10/23/91	6.0	-158.5	24.1	-55.6
10/26/91	6.7	-236.5	25.9	-79.4
10/29/91	6.1	-171.3	27.9	-58.6
11/02/91	6.0	-144.0	29.9	-28.3
11/11/91	5.8	-416.4	33.0	-39.0
11/14/91	6.7	-260.2	34.5	-63.2
11/19/91	5.5	-404.8	37.0	-52.6
11/23/91	6.2	-171.6	39.0	-47.3
11/28/91	6.5	210.7	41.2	-39.9
12/01/91	6.2	-163.0	42.4	-31.5
01/01/92	6.2	-206.3	53.6	-39.1
01/05/92	6.8	-307.3	55.1	-42.0
01/08/92	6.5	-239.4	56.2	-36.7
01/11/92	6.6	-234.0	57.3	-34.2
01/14/92	6.9	-230.0	58.4	-34.7
01/17/92	6.6	-239.3	59.4	-38.1
01/20/92	6.9	-292.1	60.4	-31.4
01/23/92	6.9	-264.6	61.4	-37.1
01/26/92	6.9	-230.3	62.4	-39.0

Table 14. (Continued) Daily Flux Densities for NI/OW and FY Ice.

Date	NI/OW 1/2 Max. Thickness (cm)	NI/OW Flux Density (W/m ²)	FY 1/2 Max. Thickness (cm)	FY Flux Density (W/m ²)
01/29/92	6.6	-294.3	63.4	-39.1
02/01/92	6.6	-278.8	64.3	-34.8
02/04/92	6.9	-329.5	65.3	-35.5
02/07/92	6.5	-228.4	66.3	-34.6
02/10/92	6.5	-247.2	67.3	-30.2
02/13/92	6.5	-285.9	68.3	-31.3
02/16/92	6.3	-206.6	69.2	-30.5
02/19/92	6.6	-274.0	70.1	-28.5
02/22/92	5.8	-387.2	71.1	-29.4
02/25/92	6.7	-276.0	71.9	-27.1
02/28/92	6.5	-228.5	72.8	-31.0
03/02/92	6.3	-159.0	73.6	-29.7
03/05/92	6.3	-199.0	74.4	-25.5
03/08/92	6.5	-234.9	75.3	-26.1
03/11/92	6.7	-276.3	76.1	-25.3
03/14/92	6.9	-226.0	76.9	-27.3
03/17/92	6.0	-132.6	77.6	-27.6
03/20/92	5.7	-240.4	78.4	-25.5
03/23/92	6.4	-210.6	79.2	-22.9
03/25/92	6.4	-224.1	79.9	-24.3
03/28/92	5.5	-389.4	80.4	-25.5
03/30/92	6.0	-155.9	80.9	-26.8
Average	6.3	-250.4	53.5	-43.9

Table 15. Daily Heat Fluxes for NI/OW and FY Ice.

Date	NI/OW Flux Density (W/m ²)	NI/OW (%)	NI/OW Flux (GW)	FY Flux Density (W/m ²)	FY (%)	FY Flux (GW)
10/01/91	-240.9	0.6	-14.4	-164.4	0.1	-1.6
10/04/91	-258.9	0.6	-15.5	-69.0	0.0	0.0
10/07/91	-302.6	2.3	-69.6	-106.2	0.2	-2.1
10/10/91	-308.2	0.6	-18.5	-87.3	0.0	0.0
10/13/91	-202.3	2.7	-54.6	-65.0	0.6	-3.9
10/16/91	-272.3	0.7	-19.1	-78.4	0.7	-5.5
10/19/91	-369.3	0.8	-29.5	-71.8	0.2	-1.4
10/23/91	-158.5	0.6	-9.5	-55.5	0.2	-1.1
10/26/91	-236.5	0.6	-14.2	-79.4	0.4	-3.2
10/29/91	-171.3	0.6	-10.3	-58.6	0.5	-2.9
11/02/91	-144.0	0.6	-8.6	-28.3	0.3	-0.9
11/11/91	-416.4	0.6	-25.0	-39.0	0.5	-2.0
11/14/91	-260.2	0.5	-13.0	-63.2	0.4	-2.5
11/19/91	-404.8	1.4	-56.7	-52.6	2.0	-10.5
11/23/91	-171.6	0.7	-12.0	-47.3	2.1	-10.0
11/28/91	-210.7	0.8	-16.9	-39.9	1.5	-6.0
12/01/91	-163.0	0.6	-9.8	-31.5	1.3	-4.1
01/01/92	-206.3	0.8	-16.5	-39.1	1.0	-3.9
01/05/92	-307.3	0.8	-24.6	-42.0	0.7	-2.9
01/08/92	-239.4	1.1	-26.3	-36.7	2.4	-8.8
01/11/92	-234.0	0.7	-16.4	-34.2	2.0	-6.8
01/14/92	-230.0	0.0	0.0	-34.7	1.4	-4.8
01/17/92	-239.3	0.4	-9.6	-38.1	2.5	-9.5
01/20/92	-292.1	0.5	-14.6	-31.4	0.9	-2.8
01/23/92	-264.6	0.7	-18.5	-37.1	2.1	-7.8
01/26/92	-230.3	0.3	-6.9	-39.0	1.7	-6.6
01/29/92	-294.3	0.3	-8.8	-39.1	2.1	-8.2
02/01/92	-278.8	0.7	-19.5	-34.8	2.1	-7.3
02/04/92	-329.5	0.9	-29.7	-35.5	2.1	-7.6
02/07/92	-228.4	0.6	-13.7	-34.6	2.5	-8.7

Table 15. (Continued) Daily Heat Fluxes for NI/OW and FY Ice.

Date	NI/OW Flux Density (W/m ²)	NI/OW (%)	NI/OW Flux (GW)	FY Flux Density (W/m ²)	FY (%)	FY Flux (GW)
02/10/92	-247.2	0.5	-12.4	-30.2	1.2	-3.6
02/13/92	-285.9	0.3	-8.6	-31.3	2.3	-7.2
02/16/92	-206.6	0.4	-8.3	-30.5	2.4	-7.3
02/19/92	-274.0	0.3	-8.2	-28.5	3.1	-8.8
02/22/92	-387.2	0.5	-19.4	-29.4	1.8	-5.3
02/25/92	-276.0	0.5	-13.8	-27.1	5.0	-13.6
02/28/92	-228.5	0.5	-11.4	-31.0	1.7	-5.3
03/02/92	-159.0	0.7	-11.1	-29.7	1.8	-5.3
03/05/92	-199.0	0.6	-11.9	-25.5	1.8	-4.6
03/08/92	-234.9	0.4	-9.4	-26.1	1.6	-4.2
03/11/92	-276.3	0.6	-16.6	-25.3	1.7	-4.3
03/14/92	-226.0	1.1	-24.9	-27.3	2.3	-6.3
03/17/92	-132.6	0.7	-9.3	-27.6	2.6	-7.2
03/20/92	-240.4	0.6	-14.4	-25.5	2.5	-6.4
03/23/92	-210.6	0.4	-8.4	-22.9	2.6	-6.0
03/25/92	-224.1	0.6	-13.4	-24.3	4.2	-10.2
03/28/92	-389.4	0.7	-27.2	-25.5	4.0	-10.2
03/30/92	-155.9	0.4	-6.2	-26.8	1.6	-4.3
Average	-250.4	0.7	-17.7	-43.9	1.6	-5.5

Table 16. Daily Heat Fluxes for 2 Meter Multiyear Ice.

Date	2m-MY Thickness (cm)	2m-MY Flux Density (W/m ²)	MY (%)	2m-MY Heat Flux (GW)
10/01/91	199.1	-6.2	99.3	-61.6
10/04/91	199.4	-5.7	99.4	-56.7
10/07/91	199.7	-5.4	97.5	-52.7
10/10/91	200.0	-6.0	99.4	-59.6
10/13/91	200.4	-5.8	96.7	-56.1
10/16/91	200.7	-6.0	98.6	-59.2
10/19/91	201.1	-6.6	99.0	-65.3
10/23/91	201.7	-6.9	99.2	-68.4
10/26/91	202.2	-6.7	99.0	-66.3
10/29/91	202.6	-7.7	98.9	-76.2
11/02/91	203.3	-7.7	99.1	-76.3
11/11/91	205.1	-8.2	98.9	-81.1
11/14/91	205.7	-8.3	99.1	-82.3
11/19/91	206.8	-8.5	96.6	-82.1
11/23/91	207.6	-9.0	97.2	-87.5
11/28/91	208.7	-9.5	97.7	-92.8
12/01/91	209.5	-9.3	98.1	-91.2
01/01/92	216.8	-10.6	98.1	-104.9
01/05/92	217.9	-10.1	98.5	-99.5
01/08/92	218.7	-10.8	96.5	-104.2
01/11/92	219.5	-11.1	97.3	-108.0
01/14/92	220.4	-10.5	98.7	-103.6
01/17/92	221.3	-10.9	97.2	-106.0
01/20/92	222.2	-11.3	98.6	-111.4
01/23/92	223.1	-11.2	97.2	-108.9
01/26/92	224.0	-11.2	97.9	-109.7
01/29/92	224.9	-11.6	97.5	-113.1
02/01/92	225.8	-11.1	97.2	-107.9
02/04/92	226.7	-11.3	97.0	-109.6
02/07/92	227.6	-10.9	96.8	-105.5

Table 16. (Continued) Daily Heat Fluxes for 2 Meter Multiyear Ice.

Date	2m-MY Thickness (cm)	2m-MY Flux Density (W/m ²)	MY (%)	2m-MY Heat Flux (GW)
02/10/92	228.5	-11.1	98.3	-109.1
02/13/92	229.5	-11.1	97.3	-108.0
02/16/92	230.4	-11.5	97.1	-111.7
02/19/92	231.3	-11.7	96.5	-112.9
02/22/92	232.3	-12.1	97.6	-118.1
02/25/92	233.2	-11.8	94.5	-111.5
02/28/92	234.2	-11.9	97.7	-116.3
03/02/92	234.8	-11.6	97.6	-113.2
03/05/92	235.7	-12.2	97.5	-119.0
03/08/92	236.7	-11.5	98.1	-112.8
03/11/92	237.6	-11.6	97.7	-113.3
03/14/92	238.5	-11.6	96.6	-112.1
03/17/92	239.4	-11.1	96.7	-107.3
03/20/92	240.3	-11.2	96.8	-108.4
03/23/92	241.3	-10.8	97.0	-104.8
03/25/92	241.9	-11.5	95.2	-109.5
03/28/92	242.8	-11.7	95.3	-111.5
03/30/92	243.3	-11.4	98.0	-111.7
Average	220.7	-9.9	97.7	-96.2

Table 17. Daily Heat Fluxes for 3 Meter Multiyear Ice.

Date	3 m MY Thickness (cm)	3 m MY Flux Density (W/m ²)	% MY	3m MY Heat Flux (GW)
10/01/91	299.9	-5.4	99.3	-53.6
10/04/91	300.2	-6.1	99.4	-60.6
10/07/91	300.6	-5.8	97.5	-56.6
10/10/91	300.9	-5.8	99.4	-57.7
10/13/91	301.2	-5.6	96.7	-54.2
10/16/91	301.6	-5.5	98.6	-54.2
10/19/91	301.9	-5.6	99.0	-55.4
10/23/91	302.3	-5.2	99.2	-51.6
10/26/91	302.6	-5.5	99.0	-54.5
10/29/91	302.9	-5.4	98.9	-53.4
11/02/91	303.3	-5.0	99.1	-49.6
11/11/91	304.3	-5.8	98.9	-57.4
11/14/91	304.7	-6.0	99.1	-59.5
11/19/91	305.3	-6.1	96.6	-58.9
11/23/91	305.8	-6.2	97.2	-60.3
11/28/91	306.5	-5.8	97.7	-56.7
12/01/91	306.7	-6.2	98.1	-60.8
01/01/92	311.5	-7.2	98.1	-70.6
01/05/92	312.2	-7.8	98.5	-76.8
01/08/92	312.7	-8.0	96.5	-77.2
01/11/92	313.2	-7.3	97.3	-71.0
01/14/92	313.8	-7.6	98.7	-75.0
01/17/92	314.3	-8.3	97.2	-80.7
01/20/92	314.9	-7.6	98.6	-74.9
01/23/92	315.5	-8.3	97.2	-80.7
01/26/92	316.3	-7.7	97.9	-75.4
01/29/92	316.9	-8.2	97.5	-80.0
02/01/92	317.5	-8.4	97.2	-81.6
02/04/92	318.1	-7.7	97.0	-74.7
02/07/92	318.7	-8.4	96.8	-81.3

Table 17. (Continued) Daily Heat Fluxes for 3 Meter Multiyear Ice.

Date	3 m MY Thickness (cm)	3 m MY Flux Density (W/m ²)	% MY	3m MY Heat Flux (GW)
02/10/92	319.4	-7.6	98.3	-74.7
02/13/92	320.0	-7.7	97.3	-74.9
02/16/92	320.7	-8.7	97.1	-84.5
02/19/92	321.3	-9.0	96.5	-86.9
02/22/92	322.0	-9.0	97.6	-87.8
02/25/92	322.6	-8.6	94.5	-81.3
02/28/92	323.3	-9.0	97.7	-87.9
03/02/92	324.0	-8.8	97.6	-85.9
03/05/92	324.7	-8.7	97.5	-84.8
03/08/92	325.4	-9.0	98.1	-88.3
03/11/92	326.1	-8.8	97.7	-86.0
03/14/92	326.8	-9.6	96.6	-92.7
03/17/92	327.5	-9.0	96.7	-87.0
03/20/92	328.0	-9.5	96.8	-92.0
03/23/92	328.7	-9.5	97.0	-92.2
03/25/92	329.1	-9.5	95.2	-90.4
03/28/92	329.9	-9.2	95.3	-87.7
03/30/92	330.3	-9.3	98.0	-91.1
Average	314.5	-7.5	97.7	-73.1

Table 18. Daily Total Heat Fluxes.

Date	NI/OW Flux (GW)	FY Flux (GW)	2m-MY Heat Flux (GW)	3m-MY Heat Flux (GW)	2m-MY Total Heat Flux (GW)	3m-MY Total Heat Flux (GW)
10/01/91	-14.4	-1.6	-61.6	-53.6	-77.6	-69.6
10/04/91	-15.5	0.0	-56.7	-60.6	-72.2	-76.1
10/07/91	-69.6	-2.1	-52.7	-56.6	-124.4	-128.3
10/10/91	-18.5	0.0	-59.6	-57.7	-78.1	-76.2
10/13/91	-54.6	-3.9	-56.1	-54.2	-114.6	-112.7
10/16/91	-19.1	-5.5	-59.2	-54.2	-83.8	-78.8
10/19/91	-29.5	-1.4	-65.3	-55.4	-96.2	-86.3
10/23/91	-9.5	-1.1	-68.4	-51.6	-79.0	-62.2
10/26/91	-14.2	-3.2	-66.3	-54.5	-83.7	-71.9
10/29/91	-10.3	-2.9	-76.2	-53.4	-89.4	-66.6
11/02/91	-8.6	-0.9	-76.3	-49.6	-85.7	-59.1
11/11/91	-25.0	-2.0	-81.1	-57.4	-108.1	-84.4
11/14/91	-13.0	-2.5	-82.3	-59.5	-97.8	-75.0
11/19/91	-56.7	-10.5	-82.1	-58.9	-149.3	-126.1
11/23/91	-12.0	-10.0	-87.5	-60.3	-109.5	-82.3
11/28/91	-16.9	-6.0	-92.8	-56.7	-115.7	-79.6
12/01/91	-9.8	-4.1	-91.2	-60.8	-105.1	-74.7
01/01/92	-16.5	-3.9	-104.9	-70.6	-125.3	-96.2
01/05/92	-24.6	-2.9	-99.5	-76.8	-127.0	-104.3
01/08/92	-26.3	-8.8	-104.2	-77.2	-139.3	-112.3
01/11/92	-16.4	-6.8	-108.0	-71.0	-131.2	-94.2
01/14/92	0.0	-4.8	-103.6	-75.0	-108.4	-79.8
01/17/92	-9.6	-9.5	-106.0	-80.7	-125.1	-99.8
01/20/92	-14.6	-2.8	-111.4	-74.9	-128.8	-92.3
01/23/92	-18.5	-7.8	-108.9	-80.7	-135.2	-107.0
01/26/92	-6.9	-6.6	-109.7	-75.4	-123.2	-88.9
01/29/92	-8.8	-8.2	-113.1	-80.0	-130.1	-97.0
02/01/92	-19.5	-7.3	-107.9	-81.6	-134.7	-108.4
02/04/92	-29.7	-7.6	-109.6	-74.7	-146.9	-112.0
02/07/92	-13.7	-8.7	-105.5	-81.3	-127.9	-103.7

Table 18. (Continued) Daily Total Heat Fluxes.

Date	NI/OW Flux (GW)	FY Flux (GW)	2m-MY Heat Flux (GW)	3m-MY Heat Flux (GW)	2m-MY Total Heat Flux (GW)	3m-MY Total Heat Flux (GW)
02/10/92	-12.4	-3.6	-109.1	-74.7	-125.1	-90.7
02/13/92	-8.6	-7.2	-108.0	-74.9	-123.8	-90.7
02/16/92	-8.3	-7.3	-111.7	-84.5	-127.3	-100.1
02/19/92	-8.2	-8.8	-112.9	-86.9	-129.9	-103.9
02/22/92	-19.4	-5.4	-118.1	-87.8	-142.9	-112.6
02/25/92	-13.8	-13.6	-111.5	-81.3	-138.9	-108.7
02/28/92	-11.4	-5.3	-116.3	-87.9	-133.0	-104.6
03/02/92	-11.1	-5.3	-113.2	-85.9	-129.6	-102.3
03/05/92	-11.9	-4.6	-119.0	-84.8	-135.5	-101.3
03/08/92	-9.4	-4.2	-112.8	-88.3	-126.4	-101.9
03/11/92	-16.6	-4.3	-113.3	-86.0	-134.2	-106.9
03/14/92	-24.9	-6.3	-112.1	-92.7	-143.3	-123.9
03/17/92	-9.3	-7.2	-107.3	-87.0	-123.8	-103.5
03/20/92	-14.4	-6.4	-108.4	-92.0	-129.2	-112.8
03/23/92	-8.4	-6.0	-104.5	-92.2	-118.9	-106.6
03/25/92	-13.4	-10.2	-109.5	-90.4	-133.1	-114.0
03/28/92	-27.2	-10.2	-111.5	-87.7	-148.9	-125.1
03/30/92	-6.2	-4.3	-111.7	-91.1	-122.2	-101.6
Average	-17.4	-5.5	-96.2	-73.1	-119.2	-96.2

Appendix D Daily Salt Flux Tables

Table 19. Daily Salt Flux Densities for First Year Ice.

Date	NI/OW 1/2 Max. Thickness (cm)	NI/OW Salt Flux (kg/day/m ²)	NI/OW (%)	FY 1/2 Max. Thickness (cm)	FY Salt Flux (kg/day/m ²)	FY (%)
10/01/91	5.8	1.006	0.6	7.8	0.966	0.1
10/04/91	5.5	0.881	0.6	11.0	0.646	0.0
10/07/91	5.3	1.148	2.3	13.6	0.788	0.2
10/10/91	5.6	1.176	0.6	15.8	0.643	0.0
10/13/91	5.3	0.727	2.7	18.0	0.587	0.6
10/16/91	5.6	1.104	0.7	19.8	0.585	0.7
10/19/91	5.4	1.275	0.8	21.6	0.545	0.2
10/23/91	6.0	1.425	0.6	24.1	0.455	0.2
10/26/91	6.7	1.501	0.6	25.9	0.509	0.4
10/29/91	6.1	1.284	0.6	27.9	0.438	0.5
11/02/91	6.0	1.207	0.6	29.9	0.406	0.3
11/11/91	5.8	1.351	0.6	33.0	0.349	0.5
11/14/91	6.7	1.655	0.5	34.5	0.457	0.4
11/19/91	5.5	1.513	1.4	37.0	0.381	2.0
11/23/91	6.2	1.320	0.7	39.0	0.427	2.1
11/28/91	6.5	1.268	0.8	41.2	0.310	1.5
12/01/91	6.2	1.161	0.6	42.4	0.240	1.3
01/01/92	6.2	1.310	0.8	53.6	0.335	1.0
01/05/92	6.8	1.732	0.8	55.1	0.266	0.7
01/08/92	6.5	1.564	1.1	56.2	0.285	2.4
01/11/92	6.6	1.691	0.7	57.3	0.263	2.0
01/14/92	6.9	1.957	0.0	58.4	0.270	1.4
01/17/92	6.6	1.532	0.4	59.4	0.292	2.5
01/20/92	6.9	1.932	0.5	60.4	0.240	0.9

Table 19. (Continued) Daily Salt Flux Densities for First Year Ice.

Date	NI/OW 1/2 Max. Thickness (cm)	NI/OW Salt Flux (kg/day/m ²)	NI/OW (%)	FY 1/2 Max. Thickness (cm)	FY Salt Flux (kg/day/m ²)	FY (%)
01/23/92	6.9	1.974	0.7	61.4	0.266	2.1
01/26/92	6.9	2.005	0.3	62.4	0.257	1.7
01/29/92	6.6	1.727	0.3	63.4	0.298	2.1
02/01/92	6.6	1.719	0.7	64.3	0.267	2.1
02/04/92	6.9	1.767	0.9	65.3	0.273	2.1
02/07/92	6.5	1.644	0.6	66.3	0.269	2.5
02/10/92	6.5	1.577	0.5	67.3	0.234	1.2
02/13/92	6.5	1.693	0.3	68.3	0.229	2.3
02/16/92	6.3	1.590	0.4	69.2	0.218	2.4
02/19/92	6.6	1.678	0.3	70.1	0.215	3.1
02/22/92	5.8	1.496	0.5	71.1	0.226	1.8
02/25/92	6.7	1.768	0.5	71.9	0.224	5.0
02/28/92	6.5	1.501	0.5	72.8	0.231	1.7
03/02/92	6.3	1.209	0.7	73.6	0.201	1.8
03/05/92	6.3	1.544	0.6	74.4	0.193	1.8
03/08/92	6.5	1.645	0.4	75.3	0.184	1.6
03/11/92	6.7	1.603	0.6	76.1	0.184	1.7
03/14/92	6.9	1.997	1.1	76.9	0.207	2.3
03/17/92	6.0	1.176	0.7	77.6	0.206	2.6
03/20/92	5.7	0.934	0.6	78.4	0.192	2.5
03/23/92	6.4	1.457	0.4	79.2	0.184	2.6
03/25/92	6.4	1.475	0.6	79.9	0.179	4.2
03/28/92	5.5	1.319	0.7	80.4	0.192	4.0
03/30/92	6.0	1.876	0.4	80.9	0.197	1.6
Average	6.3	1.421	0.7	53.5	0.334	1.6

Table 20. Daily Salt Fluxes First Year Ice.

Date	NI/OW Salt Flux Density (kg/day/m ²)	NI/OW (%)	NI/OW Salt Flux (Mkg/day)	FY Salt Flux Density (kg/day/m ²)	FY (%)	FY Salt Flux (Mkg/day)
10/01/91	1.006	0.6	60.4	0.966	0.1	9.7
10/04/91	0.881	0.6	52.9	0.646	0.0	0.0
10/07/91	1.148	2.3	264.0	0.788	0.2	15.8
10/10/91	1.176	0.6	70.6	0.643	0.0	0.0
10/13/91	0.727	2.7	196.3	0.587	0.6	35.2
10/16/91	1.104	0.7	77.3	0.585	0.7	41.0
10/19/91	1.275	0.8	102.0	0.545	0.2	10.9
10/23/91	1.425	0.6	85.5	0.455	0.2	9.1
10/26/91	1.501	0.6	90.1	0.509	0.4	20.4
10/29/91	1.284	0.6	77.0	0.438	0.5	21.9
11/02/91	1.207	0.6	72.4	0.406	0.3	12.2
11/11/91	1.351	0.6	81.1	0.349	0.5	17.5
11/14/91	1.655	0.5	82.8	0.457	0.4	15.2
11/19/91	1.513	1.4	211.8	0.381	2.0	85.4
11/23/91	1.320	0.7	92.4	0.427	2.1	89.7
11/28/91	1.268	0.8	101.4	0.310	1.5	46.5
12/01/91	1.161	0.6	69.7	0.240	1.3	31.2
01/01/92	1.310	0.8	104.8	0.335	1.0	33.5
01/05/92	1.732	0.8	138.6	0.266	0.7	18.6
01/08/92	1.564	1.1	172.0	0.285	2.4	68.4
01/11/92	1.691	0.7	118.4	0.263	2.0	52.6
01/14/92	1.957	0.0	0.0	0.270	1.4	37.8
01/17/92	1.532	0.4	61.3	0.292	2.5	73.0
01/20/92	1.932	0.5	96.6	0.240	0.9	21.6
01/23/92	1.974	0.7	138.2	0.266	2.1	55.9
01/26/92	2.005	0.3	60.2	0.257	1.7	43.7
01/29/92	1.727	0.3	51.8	0.298	2.1	62.6
02/01/92	1.719	0.7	120.3	0.267	2.1	56.1
02/04/92	1.767	0.9	159.0	0.273	2.1	57.3
02/07/92	1.644	0.6	98.6	0.269	2.5	67.3

Table 20. (Continued) Daily Salt Fluxes First Year Ice.

Date	NI/OW Salt Flux Density (kg/day/m ²)	NI/OW (%)	NI/OW Salt Flux (Mkg/day)	FY Salt Flux Density (kg/day/m ²)	FY (%)	FY Salt Flux (Mkg/day)
02/10/92	1.577	0.5	78.9	0.234	1.2	28.1
02/13/92	1.693	0.3	50.8	0.229	2.3	52.7
02/16/92	1.590	0.4	63.6	0.218	2.4	52.3
02/19/92	1.678	0.3	50.3	0.215	3.1	66.7
02/22/92	1.496	0.5	74.8	0.226	1.8	40.7
02/25/92	1.768	0.5	88.4	0.224	5.0	112.0
02/28/92	1.501	0.5	75.1	0.231	1.7	39.3
03/02/92	1.209	0.7	84.6	0.201	1.8	36.2
03/05/92	1.544	0.6	92.6	0.193	1.8	34.7
03/08/92	1.645	0.4	65.8	0.184	1.6	29.4
03/11/92	1.603	0.6	96.2	0.184	1.7	32.3
03/14/92	1.997	1.1	219.7	0.207	2.3	47.6
03/17/92	1.176	0.7	82.3	0.206	2.6	53.6
03/20/92	0.934	0.6	56.0	0.192	2.5	48.3
03/23/92	1.457	0.4	58.3	0.184	2.6	47.8
03/25/92	1.475	0.6	88.5	0.179	4.2	75.2
03/28/92	1.319	0.7	92.3	0.192	4.0	76.8
03/30/92	1.876	0.4	75.0	0.197	1.6	31.5
Average	1.481	0.7	95.8	0.334	1.6	42.0

Table 21. Daily Salt Fluxes for Multiyear Ice.

Date	3m-MY Salt Flux Density (kg/day/m ²)	3m-MY Salt Flux (Mkg/day)	MY (%)	2m-MY Flux Density (kg/day/m ²)	2m-MY Salt Flux (Mkg/day)
10/01/91	0.030	297.9	99.3	0.030	297.9
10/04/91	0.029	288.3	99.4	0.030	298.2
10/07/91	0.028	273.0	97.5	0.030	292.5
10/10/91	0.029	290.0	99.4	0.031	308.1
10/13/91	0.028	270.8	96.7	0.033	319.1
10/16/91	0.028	276.1	98.6	0.034	335.2
10/19/91	0.027	267.3	99.0	0.036	356.4
10/23/91	0.027	267.8	99.2	0.039	386.9
10/26/91	0.027	270.0	99.0	0.042	415.8
10/29/91	0.028	276.9	98.9	0.045	445.1
11/02/91	0.028	277.5	99.1	0.045	446.0
11/11/91	0.030	296.7	98.9	0.053	524.2
11/14/91	0.031	307.2	99.1	0.055	545.1
11/19/91	0.033	318.8	96.6	0.054	521.6
11/23/91	0.034	330.5	97.2	0.057	554.0
11/28/91	0.035	342.0	97.7	0.056	547.1
12/01/91	0.036	353.2	98.1	0.061	598.4
01/01/92	0.044	431.6	98.1	0.070	686.7
01/05/92	0.043	423.6	98.5	0.073	719.1
01/08/92	0.044	424.6	96.5	0.073	704.5
01/11/92	0.045	437.9	97.3	0.074	720.0
01/14/92	0.046	454.0	98.7	0.077	760.0
01/17/92	0.046	447.1	97.2	0.077	748.4
01/20/92	0.047	463.4	98.6	0.078	769.1
01/23/92	0.048	466.6	97.2	0.079	767.9
01/26/92	0.049	479.7	97.9	0.080	783.2
01/29/92	0.049	477.8	97.5	0.080	780.0
02/01/92	0.050	486.0	97.2	0.081	777.6
02/04/92	0.051	494.7	97.0	0.081	785.7
02/07/92	0.048	474.4	96.8	0.081	784.1

Table 21. (Continued) Daily Salt Fluxes for Multiyear Ice.

Date	3m-MY Salt Flux Density (kg/day/m ²)	3m-MY Salt Flux (Mkg/day)	MY (%)	2m-MY Flux Density (kg/day/m ²)	2m-MY Salt Flux (Mkg/day)
02/10/92	0.052	511.2	98.3	0.081	796.2
02/13/92	0.052	506.0	97.3	0.082	797.9
02/16/92	0.054	524.3	97.1	0.082	796.2
02/19/92	0.054	521.1	96.5	0.082	791.3
02/22/92	0.054	527.0	97.6	0.083	810.1
02/25/92	0.055	519.8	94.5	0.083	784.4
02/28/92	0.056	547.1	97.7	0.083	810.9
03/02/92	0.056	546.6	97.6	0.083	810.1
03/05/92	0.057	555.8	97.5	0.082	799.5
03/08/92	0.057	559.2	98.1	0.082	804.4
03/11/92	0.057	556.9	97.7	0.082	801.1
03/14/92	0.058	560.3	96.6	0.081	782.5
03/17/92	0.058	560.9	96.7	0.081	783.3
03/20/92	0.057	551.8	96.8	0.081	784.1
03/23/92	0.058	562.6	97.0	0.080	776.0
03/25/92	0.057	542.6	95.2	0.077	733.0
03/28/92	0.058	552.7	95.3	0.075	714.8
03/30/92	0.059	560.5	98.0	0.079	774.2
Average	0.044	431.9	97.7	0.67	648.5

Table 22. Daily Total Salt Fluxes.

Date	3m-MY Salt Flux (Mkg/day)	2m-MY Salt Flux (Mkg/day)	FY Salt Flux (Mkg/day)	NI/OW Salt Flux (Mkg/day)	2m-MY Total Salt Flux (Gg/day)	3m-MY Total Salt Flux (Gg/day)
10/01/91	297.9	297.9	9.7	60.4	368.0	368.0
10/04/91	288.3	298.2	0.0	52.9	351.1	341.2
10/07/91	273.0	292.5	15.8	264.0	572.3	552.8
10/10/91	290.0	308.1	0.0	70.6	378.7	360.6
10/13/91	270.8	319.1	35.2	196.3	550.6	402.3
10/16/91	276.1	335.2	41.0	77.3	453.5	394.4
10/19/91	267.3	356.4	10.9	102.0	469.3	380.2
10/23/91	267.8	386.9	9.1	85.5	481.5	362.4
10/26/91	270.0	415.8	20.4	90.1	526.3	380.5
10/29/91	276.9	445.1	21.9	77.0	544.0	375.8
11/02/91	277.5	446.0	12.2	72.4	530.6	362.1
11/11/91	296.7	524.2	17.5	81.1	622.8	395.3
11/14/91	307.2	545.1	15.2	82.8	643.1	405.2
11/19/91	318.8	521.6	85.4	211.8	818.8	616.0
11/23/91	330.5	554.0	89.7	92.4	736.1	512.6
11/28/91	342.0	547.1	46.5	101.4	695.0	489.9
12/01/91	353.2	598.4	31.2	69.7	699.3	454.1
01/01/92	431.6	686.7	33.5	104.8	825.0	569.9
01/05/92	423.6	719.1	18.6	138.6	876.3	580.8
01/08/92	424.6	704.5	68.4	172.0	944.9	665.0
01/11/92	437.9	720.0	52.6	118.4	891.0	608.9
01/14/92	454.0	760.0	37.8	0.0	797.8	491.8
01/17/92	447.1	748.4	73.0	61.3	882.7	581.4
01/20/92	463.4	769.1	21.6	96.6	887.3	581.6
01/23/92	466.6	767.9	55.9	138.2	962.0	660.7
01/26/92	479.7	783.2	43.7	60.2	887.1	583.6
01/29/92	477.8	780.0	62.6	51.8	894.4	592.2
02/01/92	486.0	777.6	56.1	120.3	954.0	662.4
02/04/92	494.7	785.7	57.3	159.0	1002.0	711.0

Table 22. (Continued) Daily Total Salt Fluxes.

Date	3m-MY Salt Flux (Mkg/day)	2m-MY Salt Flux (Mkg/day)	FY Salt Flux (Mkg/day)	NI/OW Salt Flux (Mkg/day)	2m-MY Total Salt Flux (Gg/day)	3m-MY Total Salt Flux (Gg/day)
02/07/92	474.4	784.1	67.3	98.6	950.0	640.3
02/10/92	511.2	796.2	28.1	78.9	903.2	618.2
02/13/92	506.0	797.9	52.7	50.8	901.4	609.5
02/16/92	524.3	796.2	52.3	63.6	912.1	640.2
02/19/92	521.1	791.3	66.7	50.3	908.3	638.1
02/22/92	527.0	810.1	40.7	74.8	925.6	642.5
02/25/92	519.8	784.4	112.0	88.4	984.8	720.2
02/28/92	547.1	810.9	39.3	75.1	925.3	661.5
03/02/92	546.6	810.1	36.2	84.6	930.9	667.4
03/05/92	555.8	799.5	34.7	92.6	926.8	683.1
03/08/92	559.2	804.4	29.4	65.8	899.6	654.4
03/11/92	556.9	801.1	32.3	96.2	929.6	685.4
03/14/92	560.3	782.5	47.6	219.7	1049.8	827.6
03/17/92	560.9	783.3	53.6	82.3	919.2	696.8
03/20/92	551.8	784.1	48.3	56.0	888.4	656.1
03/23/92	562.6	776.0	47.8	58.3	882.1	668.7
03/25/92	542.6	733.0	75.2	88.5	896.7	706.3
03/28/92	552.7	714.8	76.8	92.3	883.9	721.8
03/30/92	560.5	774.2	31.5	75.0	880.7	667.0
Average	431.9	648.5	42.0	95.8	786.3	567.7

PLEASE NOTE

**Page(s) missing in number only; text follows.
Filmed as received.**

University Microfilms International

Bibliography

- Anderson, D.L. ,“Growth rate of sea ice”. *Journal of Glaciology*, 3:1170–1172, 1961.
- Assur, A. ,“Composition of Sea Ice and Its Tensile Strength”. Technical Report 598, National Research Council, U.S. Natl. Acad. Sci. Washington D.C., 1958.
- Bennington, K.O. ,“Some Crystal Growth Features of Sea Ice”. *Journal of Glaciology*, 4(36):669–688, 1963.
- Bilello, M.A. ,“Formation, Growth and Decay of Sea-Ice in the Canadian Arctic Archipelago”. *Journal of the Arctic Institute of North America*, 14, 1961.
- Carsey, F.D. *Microwave Remote Sensing of Sea Ice*. American Geophysical Union, 2000 Florida Avenue,NW,Washington DC 20009, 1992.
- Cox, G.F.N. and Weeks, W.F. ,“Equations for Determining the Gas and Brine Volumes in Sea Ice”. Technical Report 82–30, CRREL, Cold Regions Research and Engineering Laboratory, Hanover, New Hampshire, 1961.
- Cox, G.F.N. and Weeks, W.F. ,“Salinity variations in sea ice”. *Journal of Glaciology*, 13(67):109–120, 1974.
- Cox, G.F.N. and Weeks, W.F. ,“Brine Drainage and Initial Salt Entrapment in Sodium Chloride Ice”. Technical Report 345, Cold Regions Research and Engineering Laboratory, Hanover, New Hampshire, 1975.
- Cox, G.F.N. and Weeks, W.F. ,“Equations for determining the gas and brine volumes in sea-ice samples”. *Journal of Glaciology*, 29(102):306–316, 1983.
- Cox, G.F.N. and Weeks, W.F. ,“Changes in the Salinity and Porosity of Sea-Ice Samples”. *Journal of Glaciology*, 32:371–375, 1986.
- Cox, G.F.N. and Weeks, W.F. ,“Profile Properties of Undeformed First-Year Sea Ice”. Technical Report 88, Cold Regions Research and Engineering Laboratory, Hanover, New Hampshire, 1988.

- Cox, G.F.N. and Weeks, W.F. ,“Numerical Simulations of the Profile Properties of Undeformed First-Year Sea Ice During the Growth Season”. *Journal of Geophysical Research*, 93:12,449–12,460, 1988a.
- Fletcher, J.O. ,“The heat budget of the arctic basin and its relation to the climate”. Technical Report R-444-PR, Rand Corporation, 1965.
- Gineris, D.J. and Fetterer, F.M. ,“The Joint Ice Center SAR Workstation: Algorithm Evaluation”. Technical Report NRL/MR/7240-93-7019, Naval Research Laboratory, Stennis Space Center, MS 39529-5004, 1993.
- Goodrich, L.E. ,“A One-Dimensional Numerical Model for Geothermal Problems”. Technical Report 421, National Research Council of Canada Division of Building Research, 1974.
- Goodrich, L.E. ,“Efficient Numerical Technique for One-Dimensional Thermal Problems with Phase Change”. *International Journal of Heat Mass Transfer*, 21:615-621, 1978.
- Goodrich, L.E. ,“An Introductory Review of Numerical Methods for Ground Thermal Regime Calculations”. Division of Building Research Paper 1061, National Research Council of Canada, Division of Building Research, 1982.
- Graystone, P. and Langleben, M.P. ,“Ring-Tensile strength of Sea Ice”. In Kingery, W.D., editor, *Ice and Snow – Processes, Properties and Applications*. M.I.T. Press, Cambridge, 1963.
- Kim, Y.S. *Theoretical and Experimental Study of Radar Backscatter from Sea Ice*. PhD thesis, University of Kansas, 1984.
- Kim, Y.S., Moore, R.K., Onstott, R.G., and Gogineni, S. ,“Towards Identification of Optimum Radar Parameters for Sea Ice Monitoring”. *Journal of Glaciology*, 31(109), 1985.
- Kwok, R., Rignot, E., and Holt, B. ,“Identification of Sea Ice Types in

- Spaceborne Synthetic Aperture Radar Data". *Journal of Geophysical Research*, 97(C2):2391–2402, 1992.
- Makshtas, A.P. *The Heat Budget of Arctic Ice in the Winter*. Gidrometeoizdat, Leningrad, US Army Cold Regions Research and Engineering Laboratory, Hanover, New Hampshire 03755 (translated 1991), 1984.
- Marshunova, M.S. ,“Principal Characteristics of the Radiation Balance of the Underlying Surface and of the Atmosphere in the Arctic (in Russian)”. *Proc. Arctic Antarctic Research Institute*, 229:5–53, 1961.
- Maykut, G.A. ,“Energy Exchange Over Young Sea Ice in the Central Arctic”. *Journal of Geophysical Research*, 83:3646–3658, 1978.
- Maykut, G.A. ,“Large-Scale Heat Exchange and Ice Production in the Arctic”. *Journal of Geophysical Research*, 87:7971–7984, 1982.
- Maykut, G.A. *The Geophysics of Sea Ice*. Plenum Press, 233 Spring Street, New York,N.Y. 10013, 1986.
- Maykut, G.A. and Perovich, D.K. ,“The Role of Shortwave Radiation in the Summer Decay of Sea Ice Cover”. *Journal of Geophysical Research*, 92(C7):7032–7044, 1987.
- Maykut, G.A. and Untersteiner, N. ,“Some Results from a Time-Dependent Thermodynamic Model of Sea Ice”. *Journal of Geophysical Research*, 76:1550–1575, 1971.
- Nakawo, M. and Sinha, N.K. ,“Growth Rate and Salinity Profile of First-Year Sea Ice in the High Arctic”. *Journal of Glaciology*, 27(96):315–330, 1981.
- Ono, N. ,“Specific Heat and Heat of Fusion of Sea Ice”. In Oura, H., editor, *Physics of Snow and Ice: International Conference on Low Temperature Science 1966 Proceedings*, volume 1. Institute of Low Temperature Science, Hokkaido University, Sapporo, Japan, 1967.

- Ono, N. ,“Thermal Properties of Sea Ice IV”. Technical report, CRREL, Cold Regions Research and Engineering Laboratory, Hanover, New Hampshire, 1975.
- Parkinson, C.L., Comiso, J.C., Zwally, H.J., Cavalieri, D.J., Gloersen, P., and Campbell, W.J. *Arctic Sea Ice, 1973–1976*. National Aeronautics and Space Administration, NASA Scientific and Technical Information Branch, Washington, D.C., 1987.
- Sarmiento, J.L. and Toggweiler, J.R. ,“A New Model for the Role of the Ocean in Determining Atmospheric PCO_2 ”. *Nature*, 308:621–623, 1984.
- Schwarzacher, W. ,“Pack-Ice Studies in the Arctic Ocean”. *Journal of Geophysical Research*, 64:2357–2367, 1959.
- Schwerdtfeger, P. ,“The Thermal Properties of Sea Ice”. *Journal of Glaciology*, 4:789–807, 1963.
- Soulis, E.D., Lennox, W.C., and Sykes, J.F. ,“Estimation of the Thickness of Undeformed First Year Ice Using Radar Backscatter”. *Journal of Geophysical Research*, 1989.
- Thorndike, A.S. ,“A Toy Model Linking Atmospheric Thermal Radiation and Sea Ice Growth”. *Journal of Geophysical Research*, 97(C6):9401–9410, 1992.
- Thorndike, A.S. ,“Estimates of Sea Ice Thickness Distribution Using Observations and Theory”. *Journal of Geophysical Research*, 97(C8):12601–12605, 1992.
- Thorndike, A.S., Rothrock, D.A., Maykut, G.A., and Colony, R. ,“The Thickness Distribution of Sea Ice”. *Journal of Geophysical Research*, 80(33):4501–4513, 1975.
- Ulaby, F.T., Moore, R.K., and Fung, A.K. *Microwave Remote Sensing: Active and Passive Volume I*. Artech House, 685 Canton Street Norwood, MA 02062, 1981.
- Ulaby, F.T., Moore, R.K., and Fung, A.K. *Microwave Remote Sensing: Active and Passive Volume II*. Artech House, 685 Canton Street Norwood, MA 02062, 1982.

- Ulaby, F.T., Moore, R.K., and Fung, A.K. *Microwave Remote Sensing: Active and Passive Volume III*. Artech House, 685 Canton Street Norwood, MA 02062, 1986.
- Untersteiner, N. ,“Calculations of temperature regime and heat budget of sea ice in the central arctic”. *Journal of Geophysical Research*, 69:4755–4766, 1964.
- Untersteiner, N. ,“Natural Desalinization and Equilibrium Salinity Profile of Old Sea Ice”. In Oura, H., editor, *The Physics of Snow and Ice: International Conference on Low Temperature Science*, volume 1, pages 569–577, Sapporo: Institute of Low Temperature Science, Hokkaido University, 1967.
- Untersteiner, N. ,“Natural desalination and equilibrium salinity profile of perennial sea ice”. *Journal of Geophysical Research*, 73:1251–1257, 1968.
- Vant, M.R., Ramseier, R.O., and Makios, V. ,“The Complex Dielectric Constant of Sea Ice at Frequencies in the Range 0.1–40 GHz”. *Journal of Applied Physics*, 43(3), 1978.
- Wadhams, P. and Comiso, J.C. *Microwave Remote Sensing of Sea Ice*, pages 375–383. American Geophysical Union, 2000 Florida Avenue,NW,Washington DC 20009, 1992.
- Weller, G. ,“Radiation Flux Investigation”. Technical Report 14, AIDJEX Bulletin, 1972.
- Yen, Yin-Chao. ,“Review of Thermal Properties of Snow, Ice and Sea Ice”. Technical report, CRREL Report 81-10, Cold Regions Research and Engineering Laboratory, Hanover, New Hampshire, 1981.
- Zubov, N.N. (*L' dy Arktiki*) *Arctic Ice*. Izdatel'stvo Glavermorputi, Moscow, 1945.